Spinning Functional Fibers: An Interplay of Rheology, Miscibility & Crosslinking

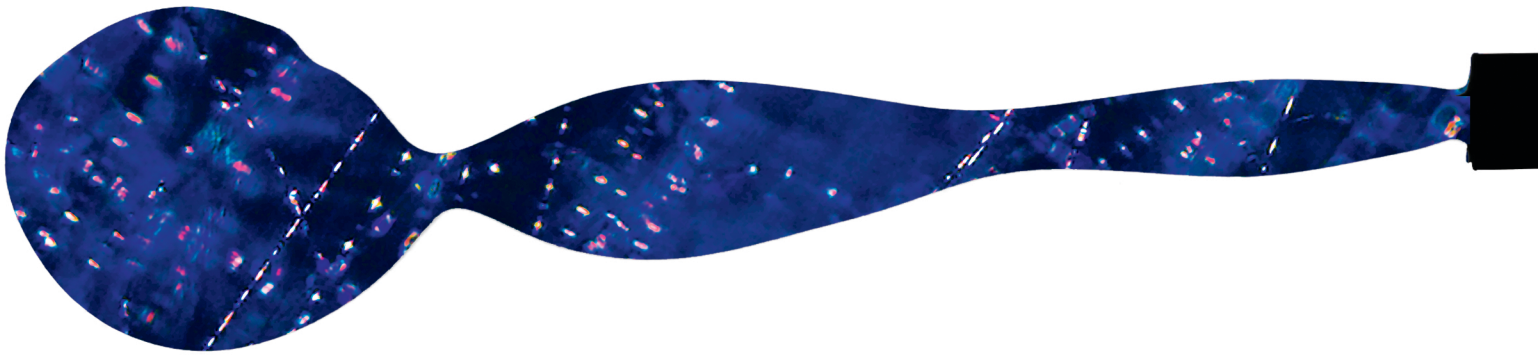

Shameek Vats

UNIVERSITÉ DU LUXEMBOURG

PhD-FSTM-2021-076
The Faculty of Science, Technology and Medicine

DISSERTATION

Defence held on 08/10/2021 in Luxembourg
to obtain the degree of

DOCTEUR DE L'UNIVERSITÉ DU LUXEMBOURG

EN PHYSIQUE

by

Shameek VATS
Born on 05 February 1991 in Patna, (India)

SPINNING FUNCTIONAL FIBERS: AN INTERPLAY OF RHEOLOGY, MISCIBILITY & CROSSLINKING

Dissertation Defence Committee

Prof. Dr Jan LAGERWALL, Dissertation supervisor
Professor, Université du Luxembourg

Dr. Anupam SENGUPTA, Chairman
Assistant Professor, Université du Luxembourg

Dr Giusy SCALIA
ADR, Université du Luxembourg

Dr Margaret FREY
Professor, Cornell University

Dr Maria Helena GODINHO
Associate Professor, Universidade Nova de Lisboa

Université du Luxembourg
The Faculty of Sciences, Technology and Communication

Spinning Functional Fibers: An Interplay of Rheology, Miscibility & Crosslinking

Shameek Vats

A Cumulative Dissertation to obtain the degree
Doctor of Philosophy
at the Department of Physics and Materials Science

I dedicate this work to all my teachers, for inspiring, instilling curiosity, love for learning, and igniting imagination in me.

Acknowledgements

I would like to deeply express my gratitude to the all those people who have taught, helped and guided me throughout this long and intense journey and many more who have accompanied me in the course of it.

First and foremost, I would like to thank my supervisor **Prof. Jan Lagerwall** for offering me the opportunity to be part of the ESMP group, teaching me not only the science of liquid crystals and electrospinning with utmost patience, but also the spirit of humility in his own deeds of being a great scientist. In my every unsuccessful attempt and failures, he had all positive encouragement for me to have faith in myself. Jan you have been an excellent mentor, support and guide to me.

I would also like to thank my CET members, Prof. Margaret Frey and Dr. Giusy Scalia for their kind nature and giving me periodic feedback, providing insightful comments and suggestions on the progress of my work. I would also like to use these lines to acknowledge my co-supervisor, Francesco for not only carrying out experiments in the lab with me but also for providing me with inputs and ideas for my work. Many thanks to Prof. Helena Godinho for giving me the chance to visit her lab in Lisbon early during my PhD project. I am also thankful to David Amantia, Diego Morillo and Sonia Matencio for giving me the chance to visit and work at LEITAT, Barcelona. My time in Barcelona exposed me to a different perspective of electrospinning and helped me approach my project from a fresh point of view.

All my gratitude to Larry for answering my repetitive questions, giving me periodic feedback, advising me, improving my French language, for travel memories and more. Manos and Camila, you were always very kind, polite, helpful even more important, a big support and model to follow during this PhD. Thanks also to Zory for gentle and helpful nature and her advice and assistance during the SEM imaging of some of my samples. I am grateful to Catherine, who was the first person to train me on electrospinning in the group.

I would like to acknowledge every group member: Anjali, Yong, Hakam, Rijeesh, Nikolay, Christina, Ursa, Jampani, JungHyun, Ashutosh, Deniz, Tabea, Rukhsar and Andy, for creating a fun, joyful and productive work environment. Thanks also to Monique Wiesinger for her support and assistance with some urgent and untimely need of chemicals. The technicians, Uli, Robbie, Nicolas, Bob and Olga have always been helpful with setting up, modifications

and repairing of the equipment. The administration would have a daunting task without the assistance of Paula, Vanessa, Astrid and Adamantia and I am equally thankful and grateful to them. To my office mates, Xu and Najiya, I will cherish all the fun and banter we shared in our office, I wish you luck in your PhD, I am sure you guys will do well.

My heartfelt thanks to my coworkers turned friends, Claudius, Ashik and Meenu for very dearly caring about me and lifting me up when I felt lost. All the laughter, travel and fun we shared makes this PhD journey even more memorable. To Katrin, my confidant of the Spiderlab, thank you for bearing with all my complains of failed experiments and for tolerating my music in the lab. I wish you luck for all your future endeavors. Thank you Anshul, Abhinav and little Ilina for never letting me feel home sick, for all the festival celebrations and lot more. I would also like to thank the other research groups at Campus Limpertsberg for making both research and life so much fun at the university campus.

There are many others who have been important in the last four and a half years, perhaps not directly related to my project but mostly to my personal life. Living away from home is demanding and depressing at times, and I am grateful to have my friends alongside me all through this time. A big shout out to Nathan and Andrea Gutierrez for being fun and caring roommates, I extend my gratitude to friends: Esperanza, Giulia Pagano, Andres, Steffi, Ruben and Beatrice for all the fun, laughter and craziness we shared together. A big warm thank you to the "Sene-gang": Maria, Debora, Natasâ, Andrea Susanna and Luca. I believe the COVID-19 lockdown brought us closer and I am grateful to have met you guys and would not have been able to go through this journey without you.

Finally, I would like to express, admiration and dedicate all my accomplishments to my two constant pillars of strength - my mom and my sister, for the sacrifices they make for me, their unconditional love and support.

Abstract

Wearable technology in general has increasingly gained interest in the last few decades and textile with incorporated functional component constitute one form of it. There are multiple ways to produce polymer fibers on both laboratory and industrial scales, and one of them is core–sheath electrospinning, which is a powerful method for producing advanced composite fibers. Liquid crystals (LCs), are materials that readily exhibit optical response to fluctuations and change in their immediate environment. By incorporating LC within polymer fibers through electrospinning, it is possible to create responsive LC-polymer fiber mats. However, incorporating a functional core has proven challenging for certain combinations of materials. This thesis explores and addresses some of the concerns involved in the coaxial electrospinning of fibers incorporating LCs from several standpoints.

Firstly, the effect of solvents on the electrospinning process was systematically studied. Following this, an optimum viscosity with pure and mixed solvents for successful electrospinning was identified and uniform fibers with different solvent combinations was produced. Using the knowledge gained, core-sheath electrospinning with LC as the core was carried out. One of the key findings of this work, the identification of a suitable means to reduce the interfacial tension between the core and sheath fluid to prevent break up of the jet and produce uniformly filled fibers, while at the same time avoiding complete mixing between core and sheath. These findings can be applied to any combination of core and sheath materials and should appeal to a large community of researchers.

Eventually, to achieve the durability of the LC-functionalized electrospun fiber mats for use in wearable technology, the sheath polymer of the fiber were crosslinked after spinning. The resultant crosslinked fibers were easily manipulated by hand and even fully immersed in water without dissolving and without losing their functional LC core.

This thesis is based on the following publications

1. *Stable electrospinning of core-functionalized coaxial fibers enabled by the minimum-energy interface given by partial core-sheath miscibility*

   Shameek Vats, Manos Anyfantakis, Lawrence W. Honaker, Francesco Basoli, Jan Lagerwall

   Langmuir (2021, 37, 13265-13277)

2. *Electrospinning ethanol–water solutions of poly(acrylic acid): non-linear viscosity variations and dynamic Taylor cone behavior*

   Shameek Vats, Lawrence W. Honaker, Margaret W. Frey, Francesco Basoli, Jan Lagerwall

   Macromolecular Materials and Engineering (2021, 2100640)

3. *Combining responsiveness and durability in liquid crystal-functionalised electrospun fibres with crosslinked sheath*

   Shameek Vats, Lawrence W. Honaker, Francesco Basoli, Jan Lagerwall

   Liquid Crystals (2021, DOI: 10.1080/02678292.2021.2005166)

Additional publications

1. *Elastic sheath–liquid crystal core fibres achieved by microfluidic wet spinning*

   Lawrence W. Honaker, **Shameek Vats**, Manos Anyfantakis, Jan Lagerwall

   Journal of Materials Chemistry C (2019, 7, 11588-11596)

Contents

List of Tables

List of Figures

Chapter 1

Motivation & Scope

Electrospinning is a powerful technique to produce micro and even nano scale fibers. Combining electrospinning with the responsiveness of liquid crystals (LCs) opens up wide opportunities and it has been previously proposed for developing smart wearables [10]. The main motivation for this study was to produce textile grade flexible polymer fibers with LC in the core. The idea was to use the responsiveness of the LC, to make fiber mats that function as sensors. For instance, it was demonstrated that LC-core fiber mats can be used as gas sensors [9].

Though electrospinning is a technique to produce nanofibers mostly [12, 13], our interest lies in producing micro scale fibers instead. The LC core at nano scale would not show the same effect (partly because the effect of birefringence would be weak) and hence the responsiveness of LCs cannot be utilized. Initial attempts focused on using poly (styrene-block-butadiene-block-styrene) (SBS) as the sheath due to the highly stretchable, properties of fibers made from this elastomer [14, 15], but it was difficult to encapsulate LC in the core(Figure 1.1). One outcome of this thesis is the realization that the failure was due to the solvent required for dissolving SBS being too good a solvent also for the LC core, and that the LC acts as plasticizer for the SBS.

Previous studies (Table 2.1) of core sheath electrospinning do not discuss the miscibility between core and sheath. We incorporate partial miscibility between core and sheath fluid to lower the interfacial tension between the two fluids to successfully and uniformly fill the fibers with LC.

Poly(acrylic acid) (PAA) offers an interesting choice of polymer, as it is soluble in water as well as in ethanol and it can be crosslinked to the point where it may be regarded as textile grade; which can be incorporated into garments. Here we focus on crosslinking PAA with poly vinyl alcohol (PVA), to spin fibers that are insoluble. PVA and PAA are both water soluble making

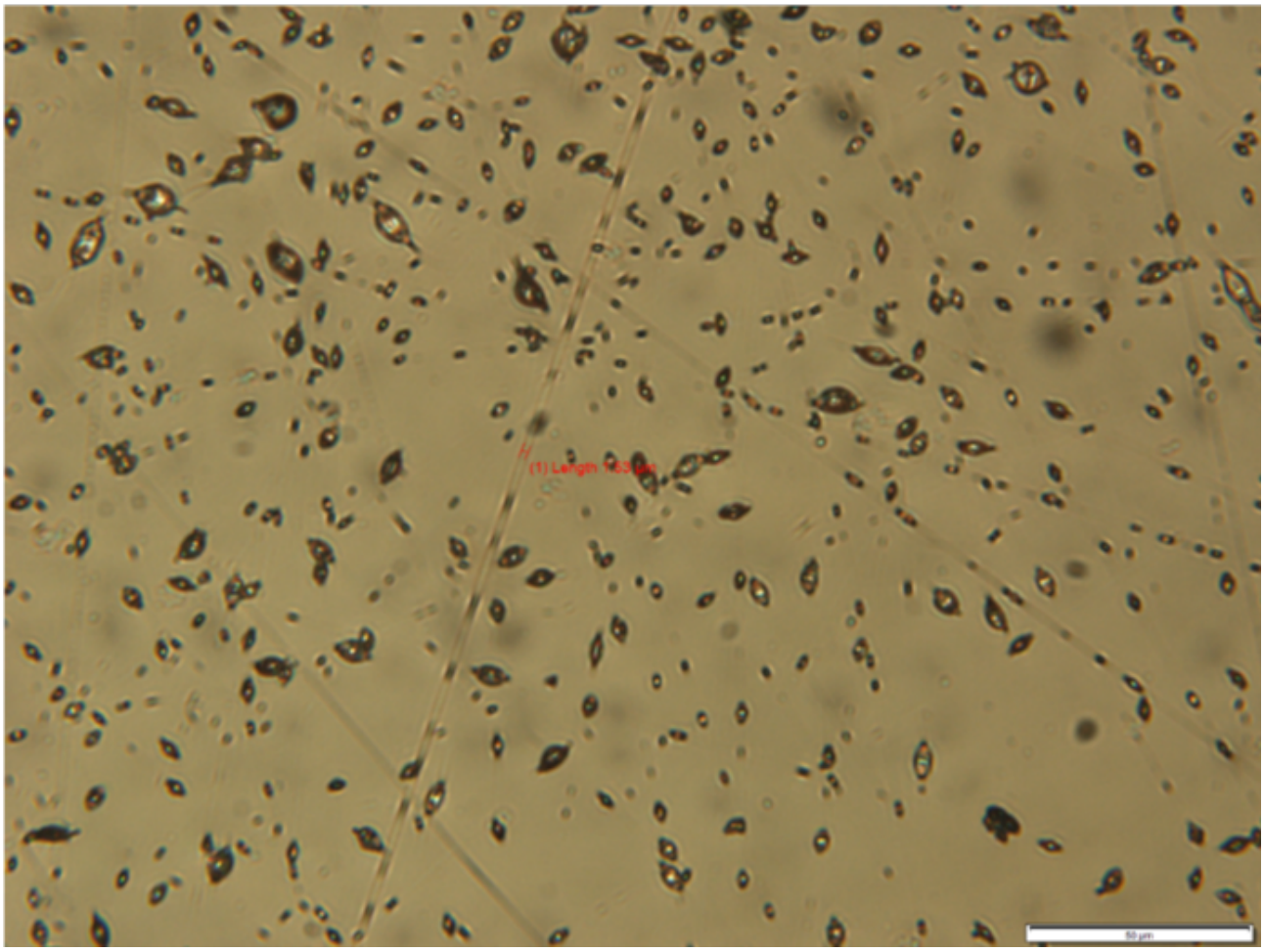

Figure 1.1: Result of coaxial electrospinning with a sheath solution of 15%w/w styrene-butadiene-styrene in tetrahydrofuran(THF)-dimethylformamide(DMF)(7-3 w/w) and 5CB as the core. Scale bar: 50μm.

them user friendly solvents to work with from a health and safety point of view.

Chapter 2

Electrospinning

2.1 What is Electrospinning?

Electrospinning (or electrostatic spinning) is a technique to produce continuous fibers from different polymer solutions and melts of micrometer down to nanometer scale in diameter. The first patent related to electrospinning came out in 1934, where Formhals revealed an apparatus for producing polymer filaments [16]. Despite the early discoveries, the process only gained more attention in the early 1990s when several research groups (in particular, Reneker and coworkers at the University of Akron) demonstrated the fabrication of thin fibers from a broad range of organic polymers [13,17]. It was during this time that the term *electrospinning* became more widely accepted and replaced the formerly used "electrostatic spinning" [18]. The past two decades have seen a significant increase in electrospinning research (Figure 2.1) in both industry and academia and the fibers produced are being utilized in a diverse range of applications such as in sensing, sound damping, self healing coatings, filtration, wound dressing, drug release and protective clothing to name some [9, 19–29].

In a typical electrospinning experiment, a high voltage is used to create an electrically charged jet of a polymer solution or melt which solidifies into a polymer fiber on a grounded collector [13]. In a classic electrospinning setup (sketched in Figure 2.2), there are three major components needed to carry out the process successfully: a high voltage power supply, a needle or a spinneret and a grounded collector.

The polymer solution or melt is fed into the spinneret by a syringe pump or a pneumatic flow control unit (as in my case a Fluigent pressure control unit described in section 7.1.2) at a constant rate. The solution (from now on I consider only polymer solutions, since I did not work with melt spinning in my thesis work) pendant drop hangs at the orifice of the spinneret

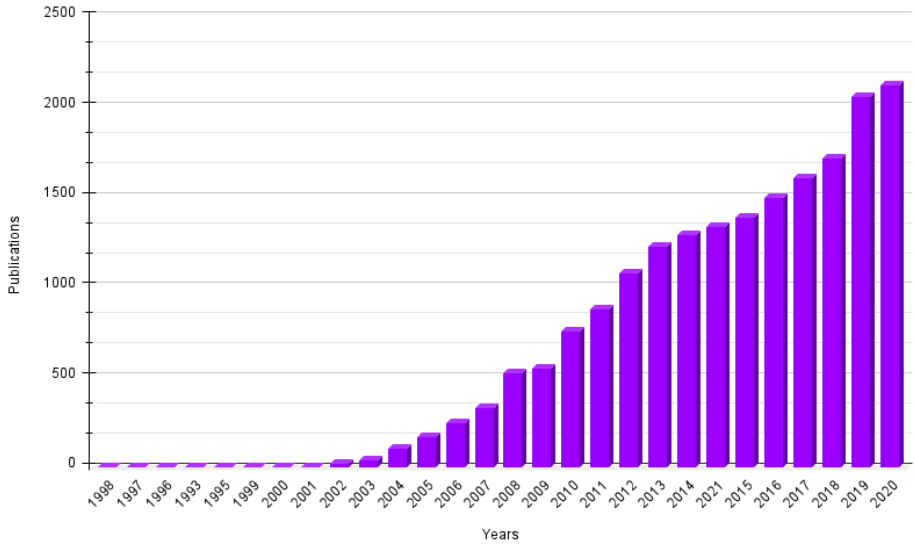

Figure 2.1: The annual number of publications on the subject of electrospinning increasing over the years. Search carried out using keywords "electrospinning" and "electrospun". For 2021 there are 1276 publication before August 27. (Source: ISI Web of Science)

until a high voltage is applied to it. The resulting electric field on the pendant drop induces a charge separation within the solution and adds excess charges that distribute evenly over the surface [30–32]. The accumulation of the charges distorts the shape of the pendant drop and transforms it into a cone called the *Taylor cone* [33, 34]. On further increasing the voltage at a critical value, the electrostatic forces overcome the surface tension and a jet erupts from the apex of the Taylor cone (Figure 2.3). As the polymer jet travels towards the collector and the solvent evaporates, it undergoes stretching and whipping due to bending instabilities arising from the self repelling surface charges [35, 36], leading to the formation of long, thin fibers.

Electrospinning is closely related to electrospraying, where a continuous stream of droplets is produced from low viscosity fluids through an applied electric field. The understanding of electrospraying is well-established and has diverse applications in processing of paints and emulsions, formation of dispersions and in mass spectroscopy [37]. In electrospraying, the viscoelastic forces of the solution are not high enough to suppress the Rayleigh Instability (chapter 5) and therefore the Taylor cone ejects droplets or a jet that eventually breaks into droplets. However, in electrospinning the polymer solution or melt needs to have a higher viscosity to suppress the Rayleigh instability and form a cylindrical jet instead of breaking into droplets. One of the challenges in electrospinning is not the dearth of fundamental understanding but the involvement and balancing of several variables/parameters.

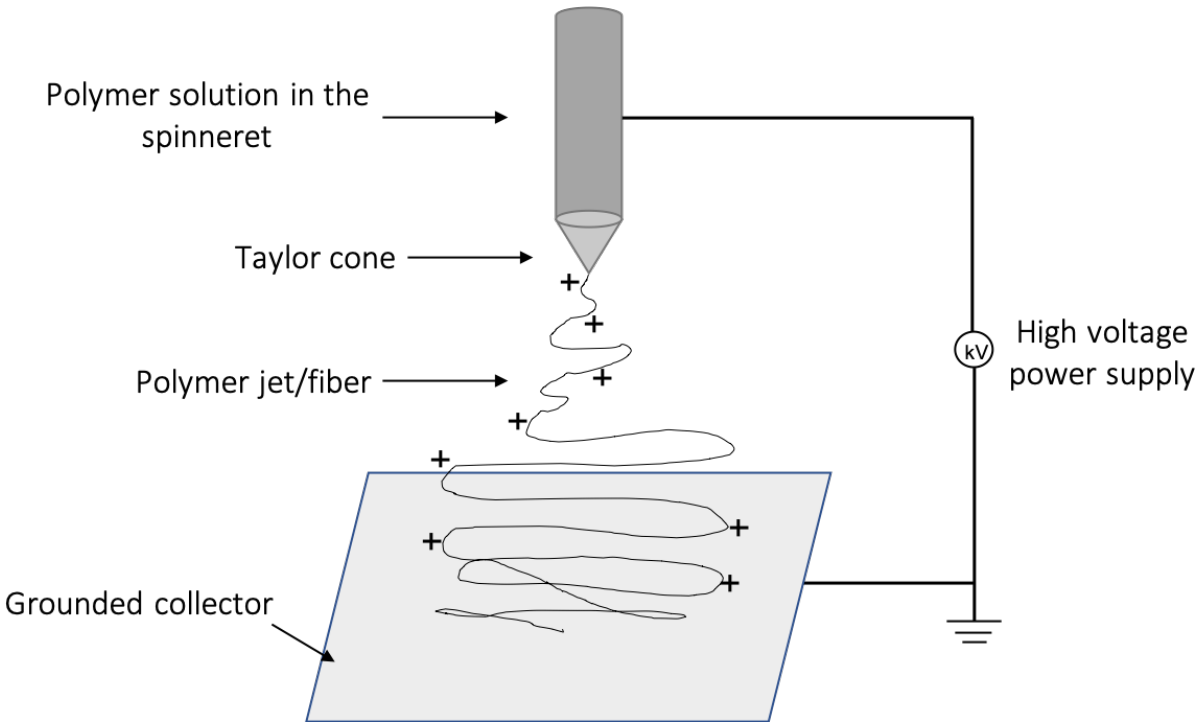

Figure 2.2: Schematic illustration of a basic electrospinning setup and of fiber formation, redrawn from [1].

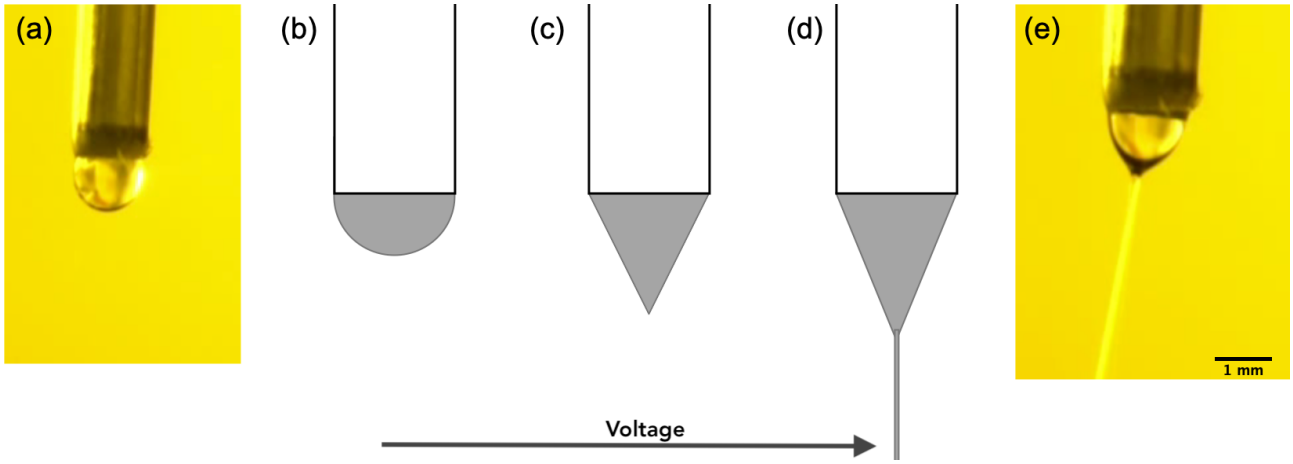

Figure 2.3: Transition behavior of the polymer solution as a result of the applied voltage. (a) An actual image and (b) sketch of the pendant drop hanging from the spinneret orifice in the absence of applied voltage. (c) When the voltage is applied, the drop deforms into a Taylor cone and (d) on increasing the voltage further at the critical value a thin jet erupts at the apex of the Taylor cone. (e) A real image of jet erupting from the Taylor cone corresponding to the sketch (d). Both the real images (a) and (e) are single fluid electrospinning of 10% w/w poly(acrylic acid) (PAA) solution in anhydrous ethanol.

2.2 Effects of various parameters on electrospinning

There are several different parameters regulating the electrospinning process and affecting the production and the morphology of the resultant fibers. These are broadly classified into: *so-*

lution, operational and ambient parameters. The solution parameters include the properties of the solution (both polymer and solvent) like viscosity, solvent volatility, conductivity and surface tension. The operational parameters include the ones that can be controlled by the operator in real time such as applied electric field, distance from spinneret tip to collector and the flow rate. Lastly, the ambient parameters encompass humidity and temperature of the electrospinning environment.

2.2.1 Solution parameters

Solution **viscosity**, measured at low shear rate, is one of the important parameters for electrospinning. A minimum viscosity (that depends on the chosen polymer and solvent) is necessary for electrospinning to occur. The solution viscosity reflects the number of polymer chain entanglements and the number of entanglements has to be sufficient for stretching the polymer jet without breaking, otherwise droplets are formed. However, a solution with excessive viscosity will be difficult to pump into the spinneret and will less likely undergo stretching induced by electric field [38]. **Surface tension**, mostly a function of solvent [39, 40] and to a lesser extent, of polymer concentration [40, 41], plays a critical role in determining fiber morphology. A solution with high surface tension (and low viscosity) yields beaded fibers as Rayleigh instability (driven by surface tension) promotes the jet break up and if there are insufficient forces to stretch the jet, the resultant fibers are beaded. Since electrospinning is an electrohydrodynamic process, the **conductivity** and **(surface) charge density** are important parameters. Both depend mostly on the chosen solvent and added salts [12, 42]. For electrospinning to occur successfully a minimum conductivity is required; however, at higher conductivity the electric field experienced by the bulk liquid will be lower as the ions at the surface will screen the applied electric field producing an unstable Taylor cone, which disrupts the spinning [31, 43]. In the intermediate optimum conductivity window, a higher conductivity and/or charge density marks a rise in Coulombic repulsion and electrostatic forces causing the jet to be more stretched and producing thinner fibers. All the parameters mentioned above are interdependent and to understand the effect of one, the rest of the parameters should be considered constant.

Smooth and non-beaded fibers are produced as a result of an interplay between solution viscosity, surface tension and charge density. Surface tension favors the jet to be broken into droplets because of Rayleigh instability, and electrostatic repulsion between the charges on the surface tends to increase the surface area and favors formation of jet. In addition, viscoelastic forces also supports stretching and formation of a jet.

The fiber jet travels from the spinneret tip towards the collector and solvent is evaporated during this short time. Therefore, **solvent volatility** is an important parameter to be considered.

When the fibers hit the collector and not all the solvent has evaporated, the resultant fibers are fused. In the other case for a highly volatile solvent an inhomogenous drying can take place. The solvent from the outer surface evaporates while the solvent is still present in the inside of the fiber. When the remaining solvent from the inner part of the fiber evaporates through the outer layer, the volume on the inside of the fibers decreases drastically giving it a "wrinkled" or "reptile skin" like structure [44] or a hollow tube which collapses into a ribbon [45].

2.2.2 Operational parameters

There should be a balance between the rate at which the solution is introduced into the spinneret and the rate at which it is drawn out. Therefore, the solution **flow rate** is important. If all other parameters are kept constant, a lower flow rate would result in a smaller or even depleted Taylor cone (Figure 2.4 (a)) as there is a greater volume of solution drawn out from the spinneret compared to the volume fed in. On the other hand, a too high flow rate results in an overfed and often a dripping Taylor cone (Figure 2.4 (b)) because more solution is pumped into the spinneret and this volume of solution is not transported away fast enough resulting in wet or fused fibers (Figure 2.5(a)).

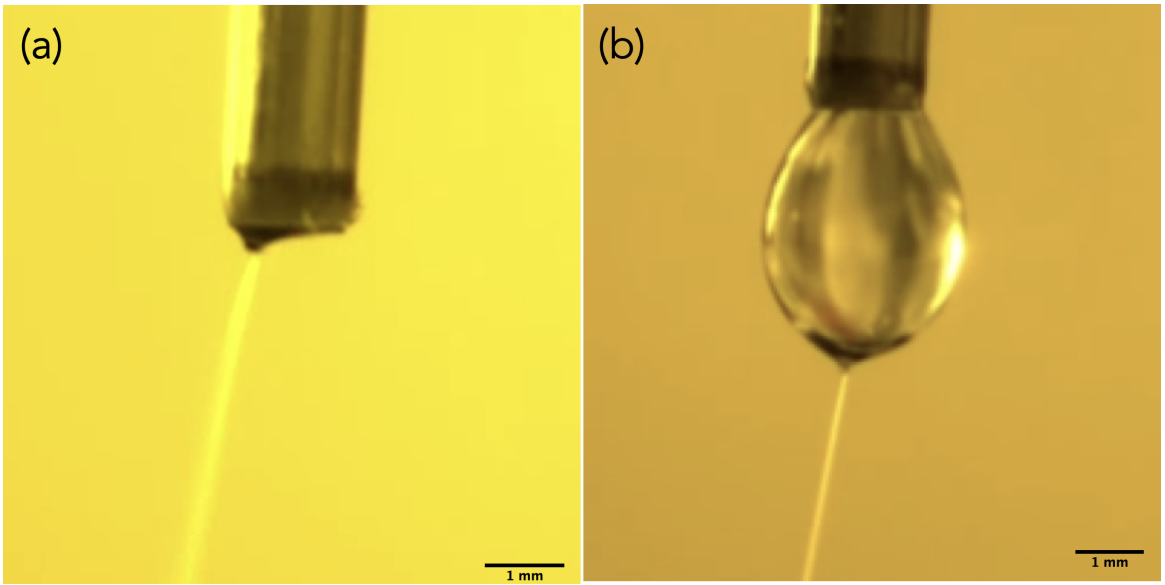

Figure 2.4: The effect of flow rate on the Taylor cone, when all the other parameters remain constant. (a) A depleted Taylor cone as a result of low flow rate and (b) an overfed Taylor cone as a result of high flow rate.

The effect of applied **voltage** is crucial in the electrospinning process as only above a threshold voltage the jet is initiated from a pendant drop as explained in the preceding sections and presented schematically in Figure 2.3.

There have been conflicting reports regarding the effect of voltage on fiber diameter at fixed flow rate. In most cases, a higher voltage induces more surface charges into the solution which requires more surface area to distribute the charges resulting in jet elongation resulting in fibers with reduced diameter [39]. Other studies have concluded that a higher voltage there is more polymer ejection and this results in fibers with larger diameter [46, 47].

At a constant voltage and flow rate, the spinneret tip to collector **distance** is another operational parameters to control the morphology of the fibers. First, the distance has critical impact as it is the electric field (voltage divided by distance), not the voltage per se, that drives the spinning. Hence, a constant electrostatic condition requires the distance to be increased (decreased) in conjunction with a voltage increase (decrease), and vice versa, a distance change requires a corresponding voltage adjustment. A smaller distance also gives the solvent less time to evaporate resulting in wet or fused fibers (Figure 2.5 (a)). On the other hand, a large distance between the spinneret tip and the collector, gives the fiber more time to stretch resulting in thinner fibers. However, if the distance is increased further, the fibers are already dried before reaching the collector and no difference is noticed for different distances [46].

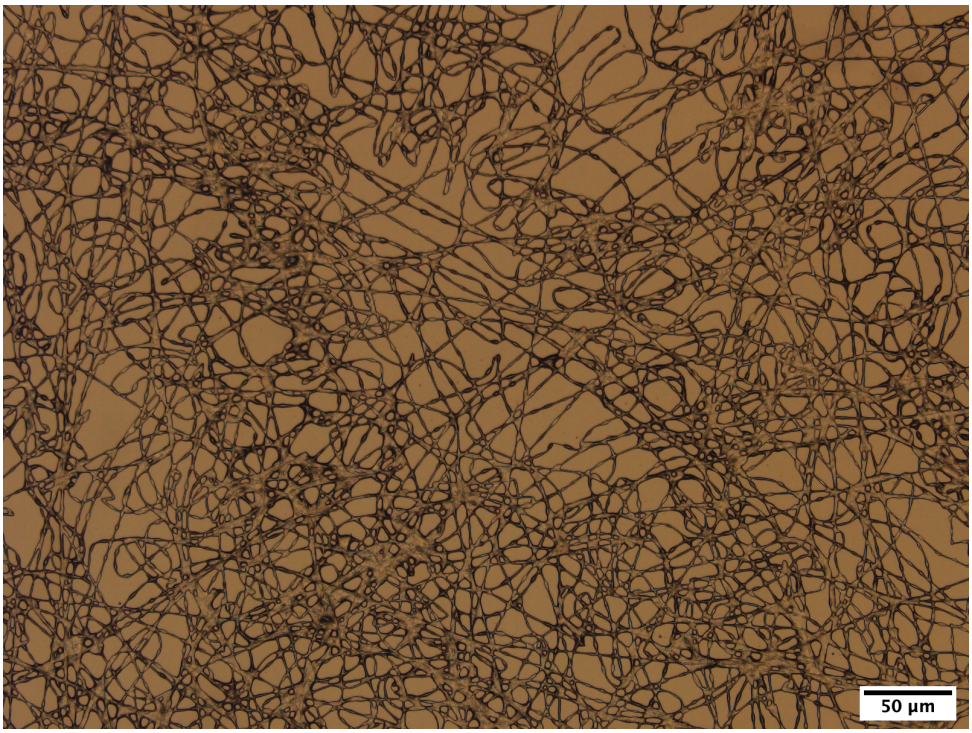

Figure 2.5: A micrograph of wet or fused fibers produced from 10% w/w polyacrylic acid in anhydrous ethanol. The fibers generated can be wet or fused as an effect of multiple parameters. (i) Solvent volatility: If the solvent has not evaporated completely. (ii) Humidity: Electrospinning in highly humid environment. (iii) Electrospinning distance: When the tip to collector distance is too low. (iv) Flow rate: When the flow rate is high and the Taylor cone is overfed.

2.2.3 Ambient parameters

The **humidity** of the electrospinning atmosphere affects the evaporation rate of the solvents. A hygroscopic polymer in a humid atmosphere absorbs more water which leads to slower solidification. This means the elongation and thinning process can continue for longer and the resultant fibers are thinner. This effect of humidity on fiber diameter was noticed by de Vrieze et al [48] for PVP and Reneker et al for PEO [49]. However, if the humidity is extremely high, there will be a greater absorbtion of water, and not all of it is evaporated before deposition on the collector. As a result the fibers formed will be wet and fused (Figure 2.5). For polymers which do not dissolve in water, a highly humid environment results in fibers with increased diameter. For example, de Vrieze et al [48] observed that for cellulose acetate, water absorption causes faster precipitation of polymer in the jet opposing the elongation and thinning during electrospinning. In addition to humidity, the **temperature** also has a role in evaporation of the solvent. Moreover, other solution parameters like viscosity and surface tension are affected by temperature; therefore, it is challenging to predict the effect of change in temperature on fiber morphology and diameter.

2.3 Coaxial electrospinning

Coaxial electrospinning first came into light when Loscertales et al. [50] pumped two immiscible fluids through concentric needles in a spinneret to generate a compound Taylor cone by applying high voltage (Figure 2.6). However, in this study they could not generate core-sheath fibers but instead electrosprayed mono dispersed compound droplets with one liquid encapsulated inside the other. Interestingly, they demonstrated that, to successfully develop a compound Taylor cone, the voltage need not be applied to the inner fluid, but just the outer fluid. Soon after, the first core-sheath fibers were reported by Sun et al. [51], where two different polymer solutions were electrospun. A major advantage of this process is that the inner fluid can even be a low molecular weight compound that normally could not be electrospun on its own [52, 53].

Composite fibers are not only produced by coaxial electrospinning but have also been obtained using single fluid electrospinning by phase separation during the process [6, 10, 54, 55]. There are contrasting results from different studies about the miscibility of core and sheath fluids. Several groups report successfully spinning core and sheath that are miscible [56–58] while others maintained that core and sheath should be immiscible [50, 59]. Table 2.1 presents an overview of coaxial spinning and spraying studies with a comment on the miscibility of core and sheath fluids. This is interesting especially in relation to our work [60] pointing out the importance of partial miscibility of core and sheath for uniform filling of fibers.

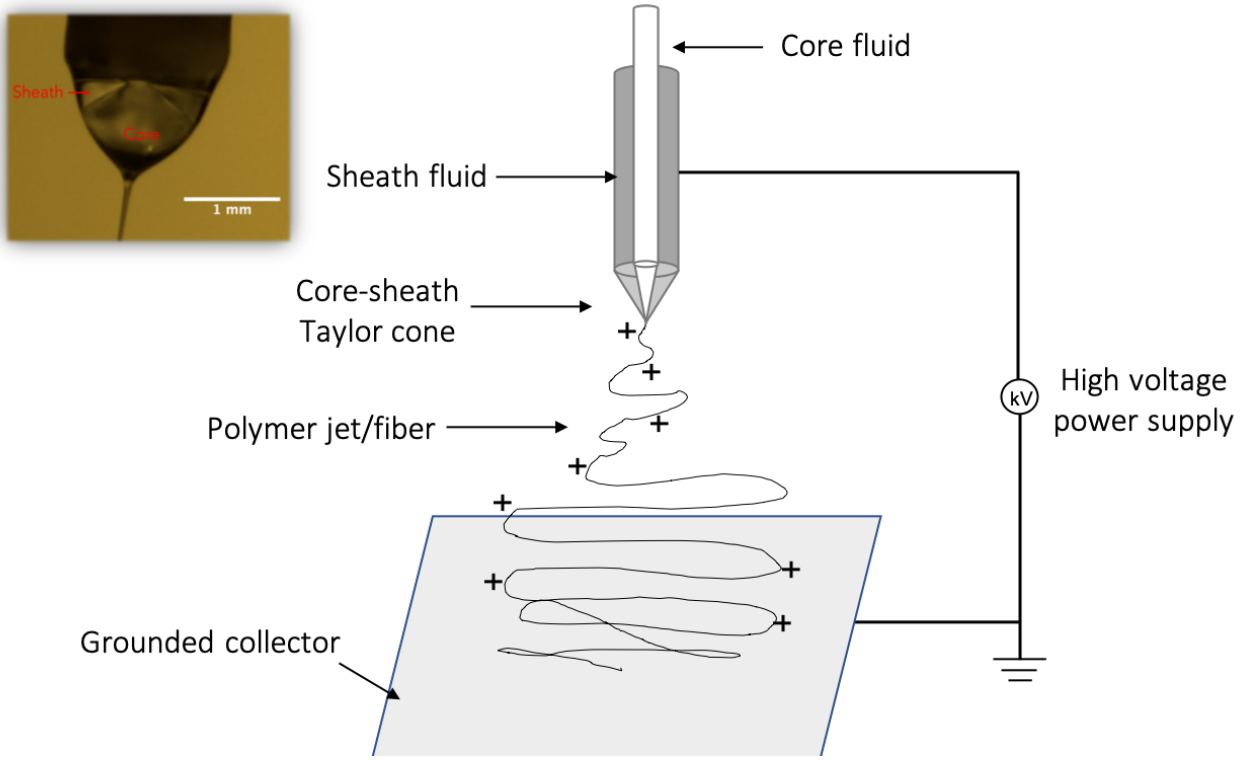

Figure 2.6: Schematic illustration of a coaxial electrospinning setup with spinneret having an inner and outer needle for core and sheath fluids. Inset: An image of the a compound Taylor cone generated during electrospinning with both fluids labeled (Scale 1 mm). Electrospinning schematic redrawn from [1]

Table 2.1: An overview of some important coaxial spinning and spraying research papers

Sheath	Core	Authors' comments about core-sheath miscibility	Outcome	Article reference
1. Somos (UV-curable polymer or reactive monomer liquid) 2. Olive oil	1. Ethylene glycol 2. Water	Core and sheath should be immiscible	Core-sheath droplets.	Loscertales et al (2002). [50]
1: PAN-co-PS in DMF 2. PVA in water 3. PEO in water	1: PAN in DMF 2. PAni in water 3. Silk in water	Common solvent (thus miscibility)	Core-sheath fibers.	Yu et al. (2004). [56]
PVP + $Ti(OiPr)_4$ in ethanol + acetic acid	Mineral oil	Core and sheath should be immiscible	Hollow tubes.	Li et al (2004). [52]
PVP + $Ti(OiPr)_4$ in ethanol + acetic acid	Hexa- and octadecane and eicosane	The core should not be soluble in the sheath solvent	Core-sheath fibers but not continuous filling.	McCann et al. (2006). [61]
PLA in 2:1(w/w) chloroform:acetone	Tetracycline hydrochloride (TCH) + 1% PLA in 2:1 (w/w) of methanol:chloroform	Core and sheath can be miscible or immiscible	Core-sheath fibers.	He et al. (2006). [62]
PVP + $Ti(OiPr)_4$ in ethanol + acetic acid	Paraffin oil	Core and sheath fluids are immiscible	Symmetric multi-core fibers.	Zhao (2007). [63]
PMMA in 3:1 (w/w) chloroform + ethanol	Mineral oil, toluene, octane and water, respectively.	They demonstrate immiscibility	Hollow fibers.	Chan et al. (2008) [64]
PVP in DMF	PDMS	No comments	Beaded fibers.	Park et al. (2009) [65]
PLA in HFIP	TCH (drug) in HFIP	Common solvent (thus miscibility)	Core-sheath fibers.	He et al. (2009). [66]
1.PVP + $Ti(OiPr)_4$ in ethanol + acetic acid or 2.PS in DMF	1.Middle fluid was water-in-oil emulsion and inner core was the identical to sheath. 2.Middle fluid was paraffin oil and inner solution was PAN in DMF.	Immiscible or poorly miscible	Rod inside a hollow tube.	Chen et al. (2010). [67]
PVP + $Ti(OiPr)_4$ in ethanol + acetic acid	Mineral oil with Ag nanoparticles.	No comments	Core-sheath fibers.	Yuan et al. (2011). [68]
PS in DMF	PU in DMF+THF and then PS in DMF inside this.	No comments	PS-in PU-in PS.	Jiang et al. (2014). [69]
PVP in ethanol and 0.5% NaCl.	Thermotropic cholesteric LC.	Core and sheath should be immiscible	Core-sheath fibers.	Lin et al. (2016). [59]
PAN in DMF	Paraffin wax in kerosene.	No comments	Core-sheath fibers.	Lu et al. (2019). [70]
PVP in EtOH with 0.5% NaCl.	5CB with or without azobenzene.	No comments	Core-sheath fibers	Thum et al. (2021). [11]

Chapter 3

Liquid crystals

3.1 What are liquid crystals?

From the popularity and success of liquid crystal displays (LCD), one might have come across the word, *liquid crystal*, at least once. Although the liquid crystal display technology evolved later, the discovery of liquid crystals was made by the Austrian botanist Friedrich Reinitzer in 1888 when he noticed that a cholestrol derivative unusually showed two "melting points" upon heating [71].

Liquid crystals (LCs) are distinct states of matter that appear between strongly organized solids and isotropic liquids (Figure 3.1). A crystalline solid has long range positional and orientational order, while a regular liquid has neither. LCs are unique in the sense that they exhibit both properties of crystals (from solids) and liquids [72,73]. They are anisotropic fluids, which means their molecules are mobile and LCs are flowing materials but on the other hand, they are partly ordered, leading to anisotropy in their properties. Because of their intermediate presence and behavior they are identified as *mesophases* and the molecules making them are called *mesogens*.

3.2 Classes of liquid crystals

Liquid crystals are largely classified into *thermotropic* and *lyotropic*. The difference between the two lies in the parameters that regulate the liquid crystalline phase. Thermotropic LCs, as the name suggests (from Greek, *thermos*, meaning heat) show temperature dependent phase behavior. On heating, a mesophase appears at a temperature above the melting point (T_m) (crystalline solid to LC transition temperature) and, on heating further to above a clearing

point (T_c) (LC to isotropic liquid transition temperature), the material exists as isotropic liquid (Figure 3.1). The terminology of the clearing point is based on the fact that a turbid liquid crystal turns into a clear liquid, as Reinitzer first observed. Lyotropic LCs, on the other hand, are more concentration dependent. They are formed from amphiphilic molecules dissolved in appropriate concentration of a suitable solvent. An example of occurrence of these phases in everyday life is soap solutions and shampoo. Since lyotropics are not part of this research study, they will not be further discussed in this thesis, but a brief introduction and basic concepts can be found for example in [74, 75].

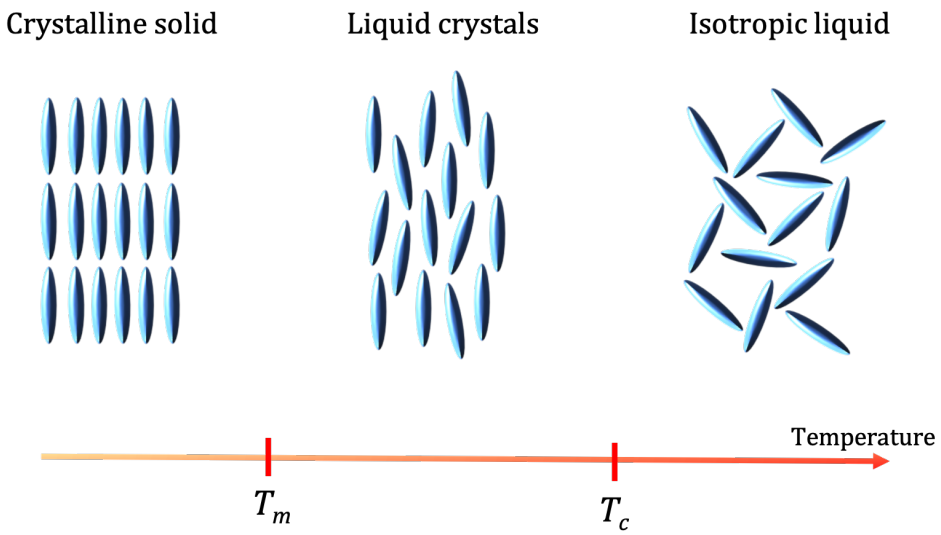

Figure 3.1: A 2D schematic showing the occurrence of liquid crystals (LC) between crystalline solids and disordered isotropic liquids. The transition temperature from solids to LC is the melting point (T_m) and the LC to isotropic liquid transition temperature is the clearing point (T_c).

3.3 Liquid crystalline phases

The properties of LCs are related to the shape anisotropy of their mesogens. The molecular structure is such that, not all the principle symmetry axes are equivalent [76]. In most cases, rod-shaped (also called *calamitic*) [73] and disc-shaped (called *discotics*) [77] molecules potentially form liquid crystalline phases, but other molecular shapes, such as, banana [78, 79] or pear [80] can also form mesophases.

Within calamitic thermotropic LCs, the most commonly encountered and well-studied mesophase is the *nematic* phase (from Greek *nýma*, or "thread", referring to thread-like inclination lines visible in polarizing optical microscopy (section 7.2), where molecules align with long range orientational order without corresponding positional order. The rod-like molecules orient with

their long-axis along a common direction, called the *director*, defined by a unit pseudovector, denoted by $\hat{n}$ [81]. In addition to the nematic, another classification is a *smectic* phase (from Latin *smecticus*, or "soap", referring to structure found in soap films), where molecules additionally segregate into layers producing a two-dimensional fluid where they can flow within the layers but less easily across them.

Cholesterics or chiral nematics, are the chiral configuration of nematic liquid crystals. These are formed either by an inherently chiral molecule or doping an achiral LC host with a chiral dopant [82, 83], often with a structure similar to the host LC. Chiral nematics are abbreviated as N^* where chirality is marked with an asterisk to distinguish it from achiral phases. As in nematic LCs the building blocks lack positional order but are oriented along the director. The director rotates in a helical manner with the twist axis perpendicular to the director. When well-aligned, this helical structure gives rise to striking colors due to Bragg reflection [84]. The reflected color is adjusted by tuning the concentration of the chiral dopant.

3.4 Orientational order parameter

Although the molecules of nematic LCs tend to orient along the director $\hat{n}$, the thermal fluctuations lead to angular deviations. This orientational distribution of individual nematic molecules is quantified by the scalar order parameter, S:

$$S = \frac{1}{2}\langle 3cos^2\theta - 1\rangle, \tag{3.1}$$

where θ is the deviation angle between the long axis of the individual molecule and the director. The order parameter lies in the range, $-\frac{1}{2} \leq S \leq 1$, with S=0 implying random orientation order in the isotropic phase and S=1, referring to perfect order in crystalline phase, meaning all the molecules are perfectly aligned in a single direction. The negative order parameter range corresponds to molecules avoiding the director, the extreme value, $S = -\frac{1}{2}$, meaning that the molecules are randomly distributed in a plane without any preferred orientation, all being perpendicular to the director [85–87]. Typically, for a nematic LC, the scalar order parameter is positive and lies in the range of 0.4-0.6 [81].

3.5 Optical anisotropy in LCs: birefringence

Normally, anisotropy in a material means their properties are different in different orientations. The long range orientational order of the LCs give rise to such anisotropy, most easily seen in the

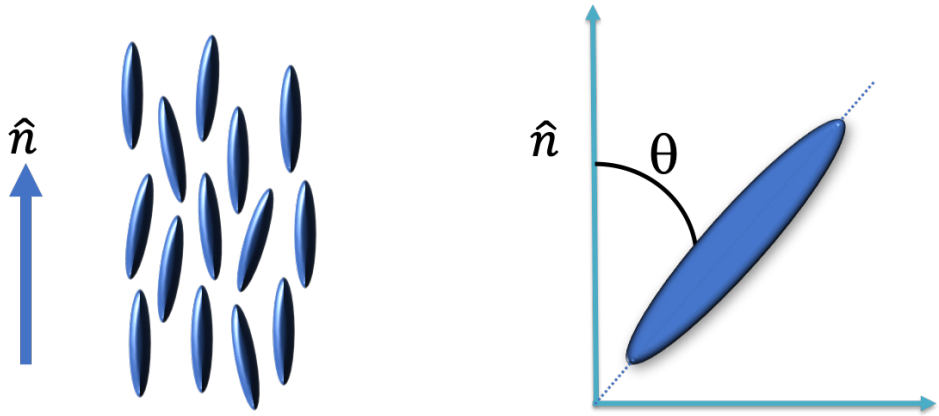

Figure 3.2: Sketch of the orientation of nematic LC molecule, preferentially along the director $\hat{n}$ and θ is the angle between the molecule and the director.

optical domain. Before proceeding further, it is important to define the *optic axis*. It indicates an axis of full rotation symmetry and when propagating along it, the light does not experience any anisotropy. In general, based on the number of optic axes, there are two categories of LCs: uniaxial and biaxial, possessing one or two optic axes, respectively. The work carried out in this research study only focuses on uniaxial LCs. The long range order of rod-shaped molecule of a uniaxial nematic LC causes the light to interact differently with light polarized along the director $\hat{n}$ as opposed to across it. This translates to two distinct indices of refraction each corresponding to orthogonal polarizations [88]. The refractive index for the polarization of light perpendicular to the director is denoted by $n_\perp$, and for the light polarized along the director (which is equivalent to the optic axis) we denote it by $n_\parallel$. Because of this double refraction, the optical anisotropy of LCs (and optically anisotropic solid crystals) is called as *birefringence*, which is quantitatively defined as the difference between the two refractive indices:

$$\Delta n = n_\parallel - n_\perp. \tag{3.2}$$

As mentioned, light passing through a birefringent medium is split into two beams with different refractive indices. They consequently travel at different velocities and on coming out of the medium they recombine but with a phase shift($\Delta\phi$) defined by [89]:

$$\Delta\phi = \frac{2\pi}{\lambda}(\Delta n)d \tag{3.3}$$

where λ is the vacuum wavelength of the light and d is the distance traveled in the medium or the sample thickness. For simplicity, I have here assumed that the light is incident perpendicular to the director, such that full birefringence (Δn), is experienced. This is the sample configuration

I use when studying LCs in this thesis. The sample thickness (d) times birefringence (Δn) is the optical path difference.

The birefringent nature of LCs allow them to be characterized by polarizing optical microscopy (POM)(section 7.2). A LC sample observed between crossed linear polarizers (where the polarizer axes are perpendicular to each other) will be bright or dark depending on the orientation of the LC with respect to the polarizer axes. If light propagates along the director, there would be no birefringence (as the incoming beam, by virtue of the transverse nature of light, must be polarized perpendicular to the director, hence it would experience only one refractive index) and the sample would appear dark. As mentioned above, in this thesis I consider only the standard configuration where the director is instead perpendicular to the light propagation, and for this situation we may write that, generally, for LC samples between two polarizers, the transmitted intensity of light is formulated as:

$$I = I_0 \sin^2 2\varphi \sin^2 \frac{\Delta\phi}{2} \tag{3.4}$$

where I_0 is the light intensity after passing through the first polarizer and φ is the angle between the optic axis and the analyzer (the second polarizer for the outbound light). As indicated by equation 3.4, the maximum intensity is observed when the sample is aligned at $\varphi = 45°$ with respect to both polarizer and analyzer, while the minimum intensity is at $\varphi = 0°$ and $\varphi = 90°$. The minimum intensity implies that the optic axis is either parallel or perpendicular to the polarization axis of each polarizer (Figure 3.3).

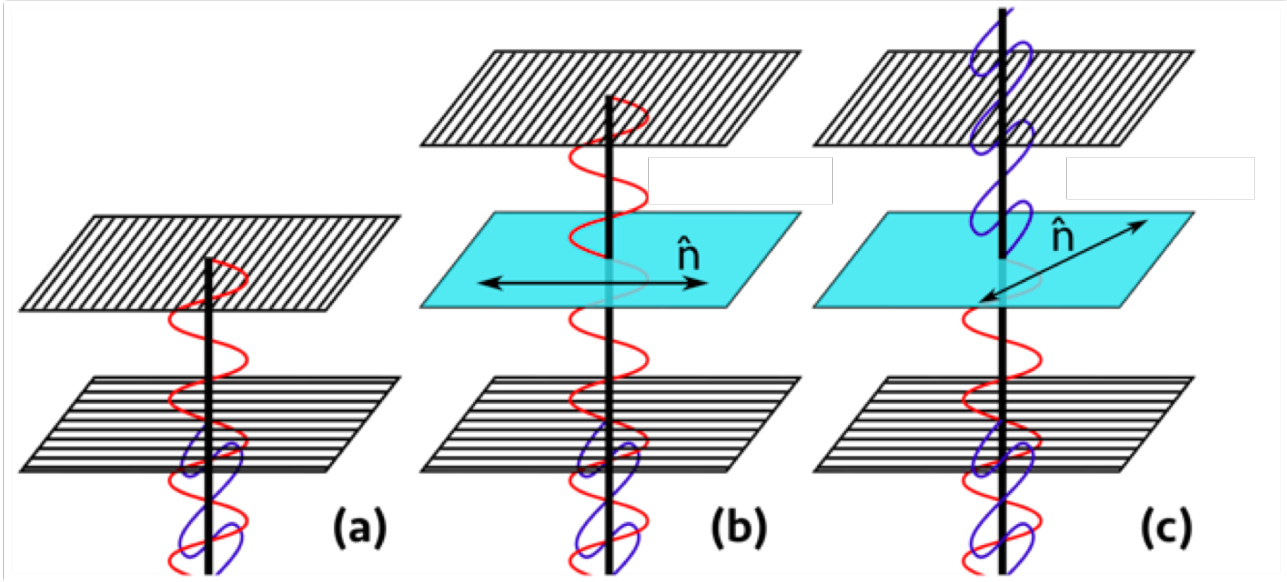

Figure 3.3: Schematic illustration of transmission of light through a uniaxial birefringent sample (in this case, a nematic LC) placed between crossed polarizers, with its optic axis in the plane of polarizers. (a) No sample is placed between the crossed polarizers to modulate the polarization of the light and therefore, no light is permitted through the analyzer (second polarizer). (b) A LC sample is placed in between the crossed polarizer with the director along either the polarizer or the analyzer axis, the polarization is not changed and no light passes through the analyzer.(c) A LC sample placed between crossed polarizers with the director oriented at 45° with respect to the polarizer (and analyzer) produces a maximum birefringence condition with maximum intensity of light observed. Image adapted from [2] and reproduced with permission.

Chapter 4

Polymers

4.1 What are polymers?

The term *polymer* derives from *poly*, the Greek prefix for "many", and *meros*, Greek for "part". Polymers, or macromolecules, can be defined as chains built up by linking together a large number of repeated functional units. These units that combine together to form a polymer molecule are termed as *monomers*. Compounds where fewer monomer units are in a chain can be termed as *oligomers*(from *oligos*, Greek for "few"). However, there is no clear distinction between an oligomer and a polymer. Polymers are broad in scope and appear all throughout nature from genetics and life (proteins, DNA, RNA) to what we use on daily basis (such as cellulose, nylons, rubbers, polyacrylamides) to high end materials like Kevlar.

4.2 Polymer structure and function

Polymers are synthesized through different processes, the most important ones of which are addition polymerization, where one monomer at a time is added to the end of the growing chain, and condensation polymerization where two units (either monomers, oligomers or polymers or any combination thereof) react into a single product.

Polymers can be either hard and brittle or soft and rubbery separated by the *glass transition temperature* T_g, below which the polymer will be in a glassy state. For temperatures between T_g and the melting temperature T_m (when this is defined, i.e., when the polymer can crystallize to some extent), the polymer is instead rubbery and shows a viscoelastic behavior [72]. This is a combination of viscous behavior, where on a long time scale the polymer "flows" and, an elastic

response acting on a short time scale, where the polymer goes back to its original configuration on release of stress.

The total mass of a polymer molecule is its *molecular mass* or *molecular weight*, but, the polymerization is rarely uniform, and it is common to report as weight-average molecular weight (M_W) and the number average molecular weight (M_N). These are defined as

$$M_N = \frac{\sum N_i M_i}{\sum N_i} \tag{4.1}$$

$$M_W = \frac{\sum N_i {M_i}^2}{\sum N_i M_i} \tag{4.2}$$

where M_i is the given molecular weight for a molecule with i monomers and N_i is the number of molecules in the sample with that size. The ratio between the two is called *polydispersity index* (PDI = $\frac{M_W}{M_N}$). It is an indicator of the distribution of molar mass in the polymer sample. For a non disperse or monodisperse sample the PDI = 1 and for a disperse or a polydisperse sample, the PDI > 1 (which means there is considerable variance in polymer chain size).

The long-range structure of the molecules of a polymer in a liquid state (molten or dissolved) is more like a bowl of spaghetti where the backbones of polymers twist and turn in a random fashion. This means that the "length" of a polymer is never the actual distance between the end groups in a stretched-out polymer. The dimensional space occupied by a polymer molecule, in its typical random coil conformation, is best described by one of the two parameters, the average end-to-end distance, $\langle r \rangle$, and the radius of gyration $\langle r_G \rangle$ defined by [90]:

$$\langle r_G \rangle = l \cdot \sqrt{\frac{N}{6}} \tag{4.3}$$

where N is the number of monomers and l the effective monomer size.

The arrangement of a polymer molecule can be modeled in number of ways, with the simplest being an ideal random coil behavior (sometimes also referred to as a random walk distribution) [91]. In this model, the polymer is described as a long chain of randomly oriented segments without interacting or being affected by the neighbors.

4.3 Polymer dissolution: Good, bad & theta solvents

The dissolution of a polymer into a solvent involves two transport processes, namely solvent diffusion and chain disentanglement. There are three distinct cases for polymer in a solvent. For a *good solvent*, the interactions between the solvent molecules and the polymer chains are more favorable than the interaction of the polymer chains with themselves. These interactions cause the polymer chain to swell, increasing its effective size with a shell of solvent molecules due to excluded volume interactions (space where the other polymer chains are not allowed to enter). In the case of a *poor solvent*, the polymer chains prefer themselves over the solvent molecules. A theta solvent is one where solvent molecules and polymer chains have no preference for each other meaning the solvent-polymer and polymer-polymer interactions are equally favorable. Thus when a polymer is added to a theta solvent it will maintain the same average end-to-end distance as in its own melt, unlike in a poor solvent, where this distance is reduced, or in a good solvent where this length increases. The theta conditions for a polymer-solvent system are very narrow, requiring both specific solvent and specific temperature [2, 92].

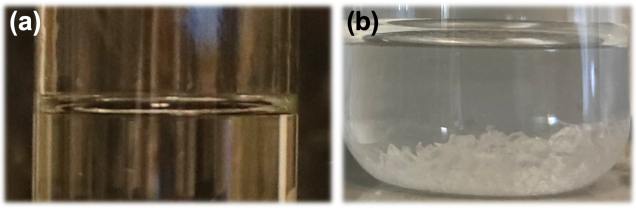

Figure 4.1: Poly(vinyl alcohol) (10%w/w): (a) dissolved in water producing a clear solution. Water is a good solvent for PVA where the polymer chain prefers the water molecules and (b) in 1,4-Dioxane, where PVA molecules prefers itself over the solvent and precipitates, thus a case of poor solvent.

4.4 Chain entanglements

Due to their large size, polymer chains tend to entangle in the liquid state. In case of polymer solutions, the degree of entanglement is related to the concentration, molecular weight and the polymer-solvent system. It affects solution viscoelastic properties and is required for electrospinning of fibers [93–95]. High molecular weight polymers are more likely to form entanglements.

At a certain concentration, called the critical overlap concentration (c^*) chain overlap is initiated and the solution transitions from dilute (Figure 4.2(a)) to semi-dilute regime (Figure 4.2(b) and (c)). In the semidilute unentangled regime (Figure 4.2(b)) the concentration is high enough to have some chain overlap (c $>c^*$) but not enough to cause any significant degree of

entanglement. On increasing the concentration further, entanglements in the solution is initiated and the solution enters the semidilute entangled regime (Figure 4.2(c)). The crossover of concentration from the semidilute unentangled to semidilute entangled regime is referred to as the critical entanglement concentration (c_e), and it marks the distinct onset of significant chain entanglements in solution, and thus suitability for electrospinning [96].

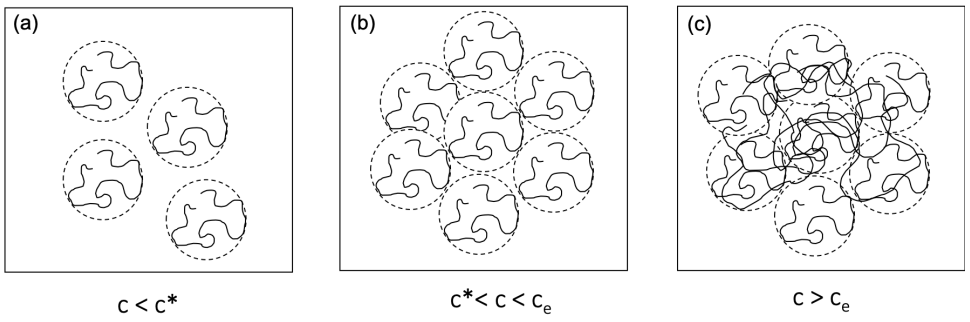

Figure 4.2: A schematic of a polymer solution representing three different regimes, (a) dilute, (b) semi-dilute unentangled and (c) semi-dilute entangled. Image redrawn from [3].

4.5 Crosslinking of polymers

Crosslinking in general refers to the process of forming chemical bonds to join polymer chains together. The bridges formed between chains leading to a three-dimensional network are "crosslinks", which can be induced by a number of ways such as photo crosslinking using a photo initiator [97, 98], heat [99] or adding a crosslinking agent [100]. The process is carried out to improve the resilience and strength of polymers and prevent them from flowing or dissolving. If the degree of crosslinking is high, the material becomes more rigid. The motivation of the thesis is to spin fibers which can be used as wearable textiles. One way of accomplishing this is to use polymers, like poly(vinyl alcohol) (PVA) and poly(acrylic acid) PAA, which are water soluble on their own, allowing them to be electrospun with low environmental impact, but which can then be crosslinked after spinning to make them durable and insoluble. For the case of PVA-PAA crosslinking, this is done via heat induced esterification (Figure 4.3), where the hydroxyl group (-OH) from PVA and carboxyl group(-COOH) from PAA form an ester linkage. Once crosslinked, the fibers resist water (Figure 4.4) and become a suitable candidate for applications.

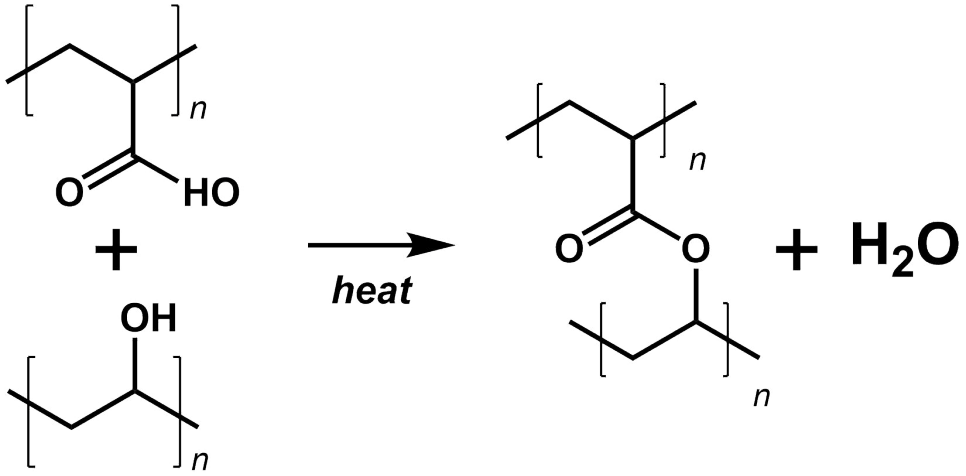

Figure 4.3: Heat induced esterification reaction between poly(acrylic) acid and poly(vinyl alcohol) to create a crosslink. The sample should be heated at 130° for 30 minutes.

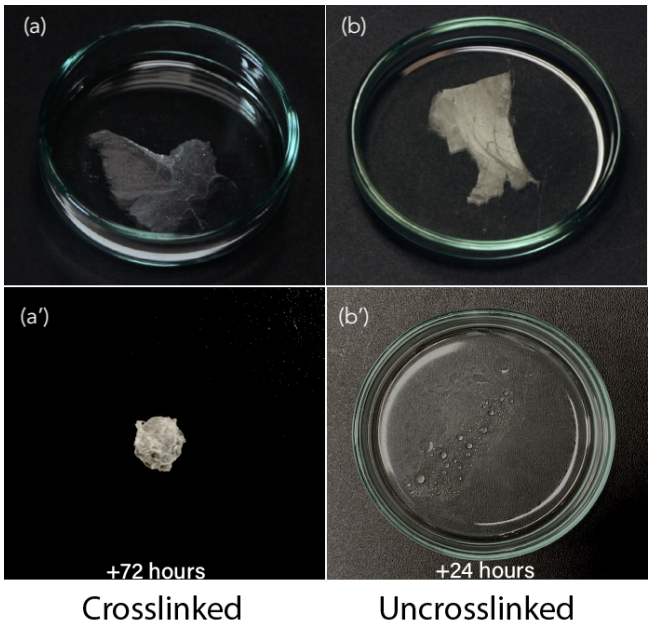

Figure 4.4: Macroscopic samples of mats spun from hybrid PVA/PAA fibers, both cross-linked (left: (a) and (a')) and not cross-linked (right: (b) and (b')). The fiber sample, (a') at 72 h after immersion contracted without a supporting frame, compared to the uncrosslinked fiber.

Chapter 5

Surface and Interfacial tension

5.1 Interfacial tension

An interface is the area which separates two phases from each other, for e.g if we consider the solid, liquid, and gas phase we immediately get three combinations of interfaces: the solid–liquid, the solid–gas, and the liquid–gas interface. Interfaces can also separate two immiscible liquids such as water and oil. The terms surface tension (usually denoted by σ) and interfacial tension (usually written as γ) are often used interchangeably. Surface tension is generally used for an air-liquid interface and interfacial tension is used when there is a liquid-liquid interface. The presence of an interface between two phases has an energy cost associated with it.

A definition of interfacial/surface tension can be considered in terms of energy. To explain, we consider a frame with a fixed and mobile side of length L, in which a film with surface tension γ is drawn, as shown in Figure 5.1. The film is relatively thick, so that the distance between the back and front surfaces is large enough to avoid overlapping of the two interfacial regions. The force exerted by the film on the movable slide is counterbalanced to maintain a stable state. Since there are two sides of the film, the force needed to maintain the surface area on one side is half the total force, thus interfacial tension is defined as [101]:

$$\gamma = \frac{1}{2}\frac{F}{L} \tag{5.1}$$

where F is the force applied and L is the length of the frame as illustrated in Figure 5.1.

The unit of surface/interfacial tension is N/m. For convenience they are usually given in mN/m

(or $10^{-3)}$ N/m), where the first "m" stands for "milli". The term "surface tension" is tied to the concept that the surface stays under a tension.

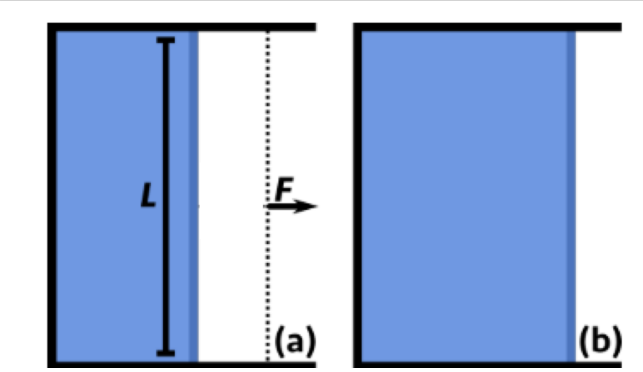

Figure 5.1: A diagram to verify and define surface tension, deriving from expansion of film between (a) and (b) by displacement of the frame length L. Image adapted from [2] and reproduced with permission.

On a molecular level, surface tension can also be defined as the property of a liquid that allows it to resist an external force at the surface, due to the cohesive forces of its molecules, as illustrated in (Figure 5.2). At the surface, molecules are only partially surrounded by other molecules and the number of adjacent molecules is less than in the bulk. The molecules at the surface of the liquid do not experience cohesive forces from the air at the liquid-air interface and the neighboring molecules on either side at the surface contribute to a net downward force over the molecules within the liquid below. Because of this force the surface resists being broken and holds the liquid together to minimize the surface area. [2, 102].

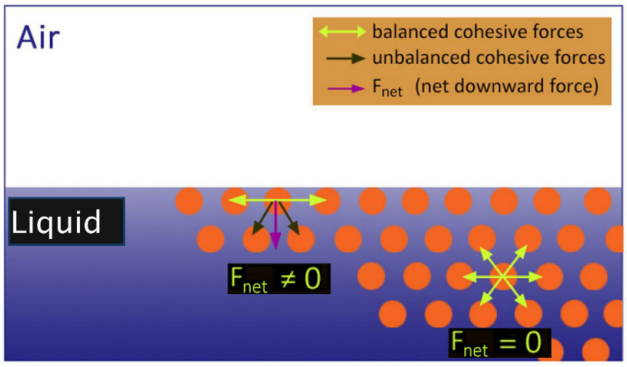

Figure 5.2: Sketch illustrating the origin of surface tension in a liquid. Image redrawn from [4].

5.2 Plateau-Rayleigh instability

One of the effects of surface tension is the *Rayleigh instability*, which helps explain why cylindrical columns of fluid break up into droplets [103]. There are small instabilities and wavelike

perturbations developed on the surface of the column, which then propagate over the length of the column/jet and lead to breaking up into droplets. To form an interface between a flowing liquid and air costs energy and to create a boundary with large surface area costs even more energy. The fluid will thus assume a shape that minimizes this energy cost, and the shape of sphere satisfies this condition as opposed to cylinder. The driving force here is that liquids, by virtue of their surface tensions, tend to minimize their surface area. Plateau and Rayleigh both first witnessed and explained this phenomena once they realized that freely falling columns (streams) of water in air eventually break up into droplets [104, 105].

In case of electrospinning (as described in chapter 2) surface tension and Rayleigh instability promote jet breakup, but they can be balanced out by applied voltage and viscoelastic forces of the polymer solution.

Chapter 6

State of the art & beyond

The encapsulation of LC in an electrospun polymer sheath was first carried out by Lagerwall and team using coaxial electrospinning to produce a composite fiber of PVP/TiO_2 as the sheath and a room temperature nematic LC as the core [22]. Independently, Buyuktanir et al. achieved LC-functionalized fibers by in-situ phase separation during spinning [106]. Later, Enz and Lagerwall, in their work, [5] produced polymer composite fiber encapsulated with a short-pitch cholesteric liquid crystal. These fibers, due to selective reflection from the LC, show a blue reflected color, as shown in Figure 6.1.

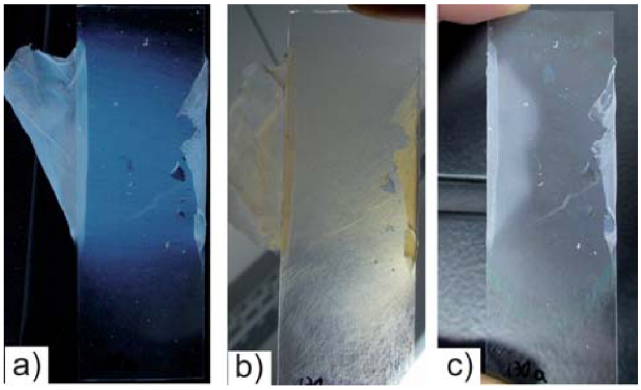

Figure 6.1: PVP fiber mat filled with cholesteric LC shows visible colors even macroscopically. In this image the fiber mats is viewed in (a) reflection, (b) transmission and (c) reflection after heating the LC to the isotropic phase. The image is reproduced from [5] with permission. Copyright 2010, Royal Society of Chemistry.

Electrospinning core-sheath fiber with LC core has attracted a lot of interest and attention in the past decades with a some exciting research being undertaken in this field [9, 19, 21, 60, 107–110]. The incorporation of LC within a polymer fiber matrix has not just been limited to coaxial electropsinning, but has also been achieved with single-fluid electrospinning.

6.1 Electrospinning with *in situ* phase separation

Apart from coaxial electrospinning, LCs have been successfully incorporated in fibers using an *in situ* phase separation technique. These fibers are electrospun from one homogeneous solution of the LC and the polymer dissolved in a common solvent. During electrospinning, the solvent evaporates, leading to LC phase separation and polymer solidification. West et al [6] in their work, studied a system each of 5CB/PVP and 5CB/PLA, (Figure 6.2) and concluded that phase separation can be used to control the morphology of the electrospun LC/polymer composite fibers. Some of the parameters with which the morphology can be tuned are the humidity, the solvent, the concentration of polymer and LC, and the polymer feed rate.

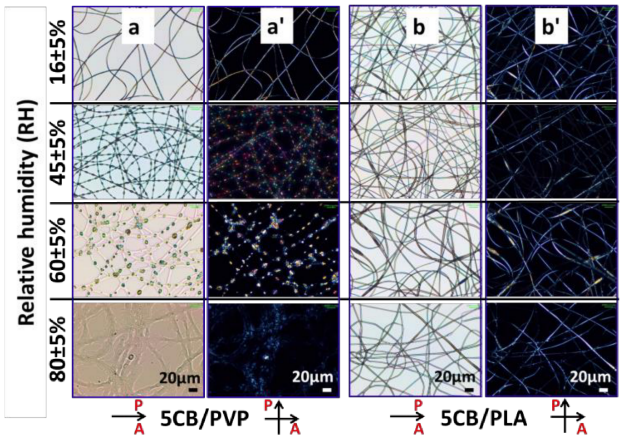

Figure 6.2: In the work of West et al., 5CB/PVP (a & a') and 5CB/PLA (b & b') fibers are produced from single fluid electrospinning using phase separation, in different relative humidities and observed using a POM. Images (a) and (b) were pictured between linear polarizers, while images (a') and (b') were captured between crossed polarizers. Image adapted from [6], reproduced with permission.

In situ phase separation has been actively used to produce LC-filled polymer fibers to study the morphology and optical properties of the fibers [54,106,109,111]. The production of core-sheath fibers through phase separation can also be employed to methods other than electrospinning, such as airbrushing.

6.2 Air brushing

Based on the in situ phase separation West et al [7,8] successfully produced LC filled PVP and PLA fibers (Figure 6.3) using a commercial airbrush. The LC and polymer are dissolved in a common volatile solvent (chloroform and acetone in this case) and a high velocity air stream produced from the airbrush deforms and drags the solution into jets. The solvent evaporates

during the process and the jet solidifies into fibers. An image of the airbrush used by West et al is shown in Figure 6.3 (c-e). The diameter of the fibers was controlled using the solution composition and conditions.

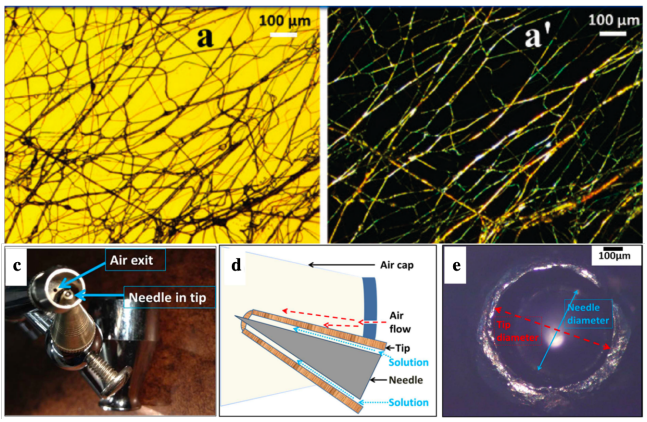

Figure 6.3: Top row: POM image of E7/PVP fibers produced using an airbrush by West et al. (a) between parallel polarizors and (a') crossed polarizers [7]. Bottom row: The airbrush used for producing LC filled PVP fibers. (c) Picture of used airbrush; (d) Cross-sectional sketch of airbrush; and (e) Microscope image of opening area between needle and tip. Image (a) and (a') reproduced from [7] and (c-e) from [8], with permission.

6.3 Applications demonstrated by LC-filled fibers

Some works [9,110,112] have successfully demonstrated the response of LC filled polymer fibers to the exposure of volatile organic vapors at room temperature. Since these fibers function non-electronically, requiring no power source, they offer potential opportunities to be used as gas sensors. Reyes et al [9], in their work show a non-woven mat made of PVP fibers, filled with the LC 5CB, that changes its optical properties within seconds when exposed to toluene vapor, as shown in Figure 6.4, visible to the unaided eye. On exposure to toluene gas, the clearing point of the LC is reduced, inducing a phase transition to isotropic at room temperature, Figure 6.4(b). This is a reversible response and the LC-filled fibers return to an opaque texture within seconds of ceasing vapor exposure, Figure 6.4(c). In their work, they observed no visible change in the response when storing fibers for a month, indicating the stability of the sensing of the fibers over a long period of time.

In addition to gas sensing, Wang and coworkers used the responsive character of LC for chemical sensing [10]. In their work, they showed 5CB filled PLA fibers appear milky white due to strong light scattering when there is no chemical exposure but they become more transparent in the presence of a VOC as shown in Figure 6.5. This is the same effect observed, demonstrated and explained by Reyes et al [9].

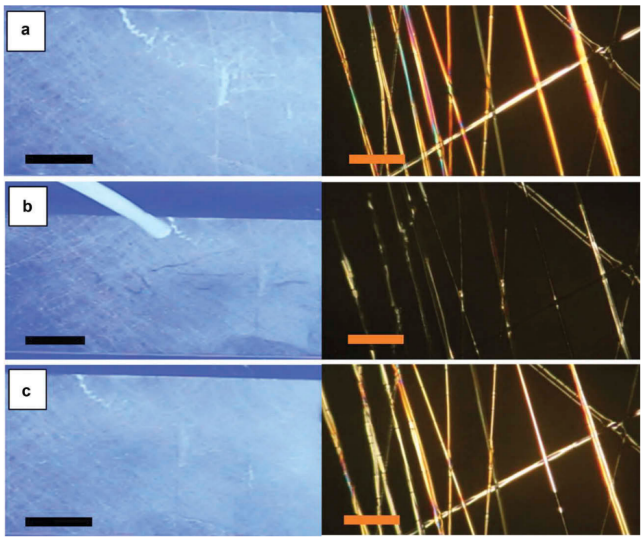

Figure 6.4: Toluene vapor sensing with electrospun 5CB/PVP fiber mat: (a) Before toluene vapor exposure, showing a scattering state; (b) On toluene exposure, the area exposed to vapor rapidly transitions from scattering to transparent due to a nematic-isotropic phase transition. When the toluene exposure is stopped, the fiber mat returns to its scattering state, as in (a). The corresponding POM images on the right column shows LC in the fibers responding to toluene exposure. The scale bar on the left column is 10 mm and on the POM images in the right column is 80 μm. Reproduced from [9] under a Creative Commons License.

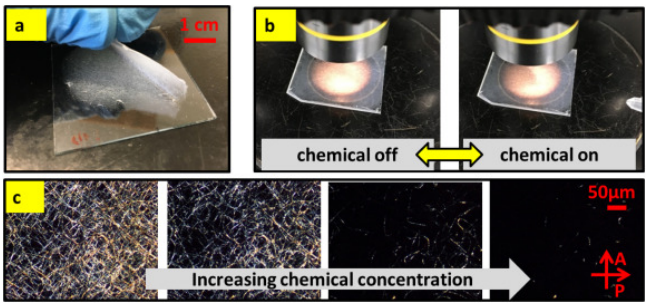

Figure 6.5: LC filled polymer fibers show visible response to chemicals and can be used as a chemical sensor. Reproduced with permission from [10], Copyright 2018, Elsevier.

Furthermore, when doped with azobenzene, the nematic to isotropic phase transition of LC can be initiated photochemically. Thum and coworkers [11] electropun PVP fibers with azobenzene-doped LC in the core and successfully demonstrated a reversible photo-induced phase transition upon irradiation with UV light at room temperature, figure 6.6. From an application point of view, this marks an important step for developing LC-filled electrospun fibers towards advanced textiles and photo displays.

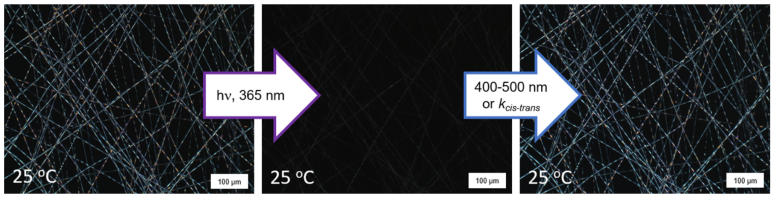

Figure 6.6: Azobenzene doped 5CB-filled electrospun PVP showing a reversible photo-induced phase transition at room temperature. Reprinted with permission from [11], Copyright 2021 American Chemical Society

6.4 What are the challenges?

Although core-sheath electrospinning is a powerful tool to produce composite fibers with LC core, it poses its own challenges. There are many materials and material combinations that are difficult to spin together. Firstly, most of the polymers used in the studies for encapsulating the liquid crystal core have poor mechanical properties and are not feasible from an application point of view. PLA is a biodegradable polymer which can be and has been used as a textile grade polymer because its mechanical properties are similar to that of polyethylene terephthalate (PET) [113]. However, it is stiff at room temperature with a low glass transition temperature (T_g=55-60°C) and a comparatively low melting point (T_m=170°C) [114]. Moreover, PLA is also prone to hydrolytic degradation, especially in an aqueous high temperature and alkaline conditions [115]. This makes it uncertain if PLA can be considered as a candidate for textile based applications.

The choice and availability of solvents to prepare the polymer solutions for core-sheath electrospinning poses a separate challenge. Some solvents (like THF, DMF, chloroform and acetone) used to make a polymer solutions are volatile, flammable and hazardous to health. Moreover, during electrospinning, a good solvent dissolves the LC in the core, thus preventing the formation of a distinct core-sheath structure in the fibers. In addition, it turns the core into a coagulation bath for the sheath solution, resulting in the gelation of the Taylor cone and thus disrupting the electrospinning process. On the other hand, a polymer solvent that does not at all dissolve the LC leads to break up of the core and even prevents the core from entering the jet during electrospinning due a relatively high interfacial tension between the core and sheath fluids. Our work [60] discusses this issue in depth and addresses the challenges encountered by the choice of solvents.

6.5 This research

The research covered in this thesis focuses on addressing the issues and challenges discussed in the preceding sections. The following subsections will briefly introduce the objectives of the three peer-reviewed publications establishing a link between the results presented in the papers.

6.5.1 Publication 1: Stable Electrospinning of Core-Functionalized Coaxial Fibers Enabled by the Minimum-Energy Interface Given by Partial Core Sheath Miscibility

A uniform filling of LC in the core of a PVP sheath was previously achieved by coaxial electrospinning and other techniques. Since PVP does not offer good mechanical properties for use as textiles from an application point of view, an alternative choice of polymer was needed. The first choice, SBS, showed that the solvents used are miscible with core and dissolve the LC; hence, there is no core-sheath structure formed. A second alternative, PVA, uses water as the solvent, which is immiscible with core and thus has a high interfacial tension between the two fluids, resulting in a beaded or absent core in the spun fibers. We eventually found PAA, a polymer that dissolves both in water and ethanol (also a solvent for LC), and can be crosslinked with PVA (which is soluble in water and sparingly so in ethanol) to create fibers that are amenable for application.

A common solvent adds partial miscibility between the core and sheath to lower the interfacial tension, which eventually helps in stabilizing the Taylor cone and filling the fibers. Interestingly, the effect of interfacial tension has seldom been discussed in core-sheath electrospinning and this paper sheds light on requirement to balance the need for a low interfacial tension with sufficiently low miscibility.

6.5.2 Publication 2: Electrospinning Ethanol–Water Solutions of Poly(Acrylic Acid): Nonlinear Viscosity Variations and Dynamic Taylor Cone Behavior

After outlining the effect of solvents in the previous study, this paper further investigates in-depth, the importance of the solvent (and solvent mixtures) on electrospinning. A publication based on fundamental science, this work is a new contribution towards the understanding of polymer-solvent interaction and its role in electrospinning of smooth and uniform fibers. The

solvent and solvent mixture ratio shows unsystematic behavior, suggesting a change in the concentration of the polymer, PAA in this case, for each ratio of the mixed solvents. Therefore, a PAA concentration for each solvent ratio was outlined using interpolation of the viscosity values and the solutions were electrospun to assess the suitability of PAA solution in each solvent mixture.

6.5.3 Publication 3: Combining responsiveness and durability in liquid crystal-functionalised electrospun fibres with crosslinked sheath

Building on the findings of publications 1 and 2, this paper discusses the research to make the fibers amenable for application so that they can be used in wearable technology. The recipe to crosslink the fibers is detailed in this paper and, after crosslinking, the fibers are shown to be sturdy enough to be manipulated by hand and to survive water immersion. Up until the previous publications, a nematic LC was used in my work, so a polarizing optical microscope (POM) was always needed to observe the fiber and validate the LC filling in the core. Here, fibers with cholesteric LC core were produced by coaxial electrospinning with the aim to observe colors with the naked eye. Furthermore, the fibers are immersed in an index matching liquid (water in this case), making the sheath swell and become transparent, offering an excellent opportunity to study the effect of confinement within fiber sheath.

Chapter 7

Experimental setups

7.1 Electrospinning setup

The electrospinning setup, of vertical geometry, used for the experiments employed a high voltage power supply (Gamma High Voltage, model ES30R-5W/DAM/RS232) to apply the electric field. The polymer solution to be spun was pumped to the vertically mounted spinneret using a microfluidic pressure controller (Section 7.1.2). The Taylor cone was imaged using a digital camera (Pixelink D755) equipped with a macro lens (Tokina AT-X Pro). The movable collector was grounded and the spinning distance was adjusted using a cogwheel. The temperature and relative humidity were monitored during all experiments and the fibers were collected either freely hanging on an untreated copper wire frame or on a glass slide. The whole setup was housed inside an acrylic box with ventilation to vent out the volatile solvents. A schematic illustration of the electrospinning setup is presented in Figure 7.1.

7.1.1 Spinneret

For spinning core-sheath fibers a stainless steel dual-phase spinneret consisting of concentric needles (external/internal diameter of the inner needle: 0.9/0.6 mm; of the outer needle: 1.7/1.4 mm), manufactured by Y-Flow was used (Figure 7.1, inset). The outer needle of the spinneret has dents to keep the inner needle in the center and, at the same time, to provide an ohmic contact between the two needles that ensures they are at the same electrical potential. The spinneret was stored in ethanol when not in use and, prior to and after experiments, was thoroughly rinsed with fresh 96% w/w ethanol to remove any material residues. Before starting the electrospinning process, the spinneret was carefully dried to avoid any possible cross

contamination from the lower-grade ethanol used for cleaning. For single fluid electrospinning, an 18-gauge blunt-tipped disposable stainless steel needle with outer diameter of 1.20 mm purchased from VWR was used.

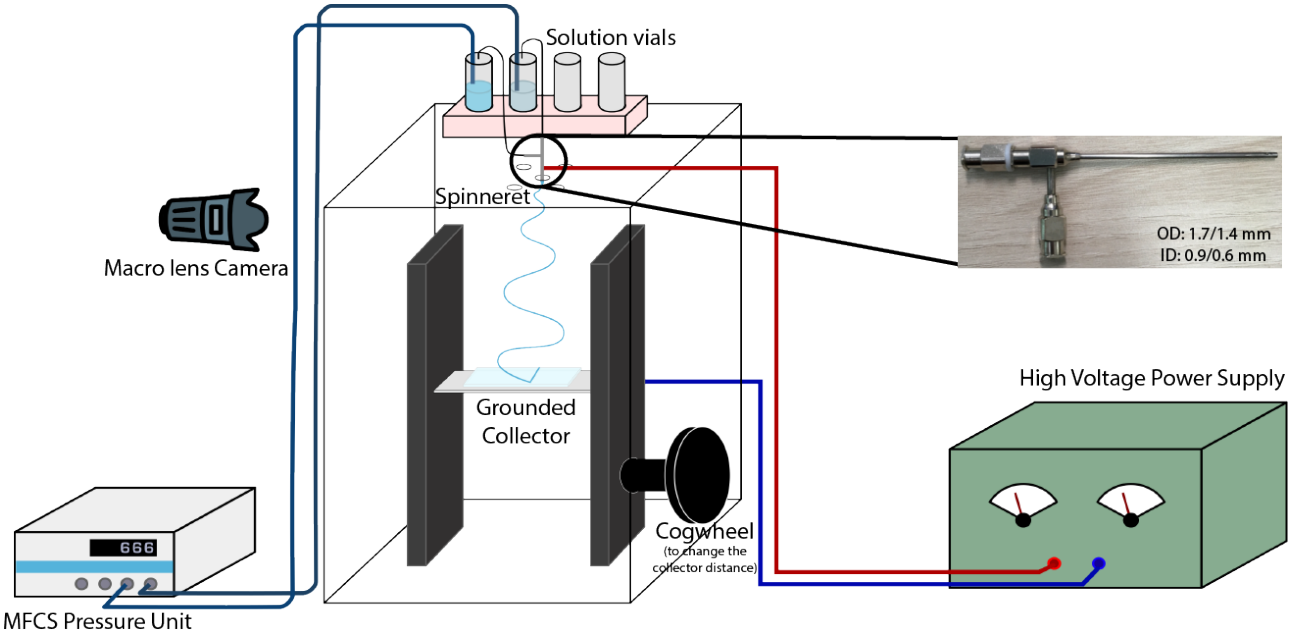

Figure 7.1: Schematic illustration of the electrospinning setup used for the producing microfibers. Inset: Image of the coaxial spinneret in the electrospinning process to spin core-sheath fibers.

7.1.2 Pressure based flow

A pressure based microfluidic flow control unit (Fluigent, model MFCS-EZ, maximum pressure 1034 mbar, uncertainty ± 0.3 mbar) was used for controlling the rates at which the polymer solution was introduced into the spinneret. As opposed to the traditional syringe pumps one advantage of using a pneumatic control is that fluids can be contained in any sample container. However, since this is a pressure based flow control, the flow rate needs to be calculated from the pressure readings using the Hagen-Poiseuille equation:

$$\Delta p = \frac{8\eta L Q}{\pi R^4} \tag{7.1}$$

where Δp is the pressure difference between the ends of the tube, Q the volumetric flow rate, η the viscosity, R the cross-sectional radius of the tube, and L its length. Simple rearrangement allows us to express Q in terms of the input parameters (most notably, Δp, L, and R):

$$Q = \frac{\Delta p \pi R^4}{8\eta L} \tag{7.2}$$

7.2 Polarizing optical microscopy (POM)

To investigate the optical properties of the fibers a light microscope was used with two adjustable polarizers set in crossed configuration, i.e., with their transmission directions perpendicular to each other. It works on the basic principle that light exiting the first polarizer can exit also the second one (called the analyzer) only if it interacts an optically anisotropic sample between the two polarizers. The sample changes the polarization and the strength of the effect depends on the wavelength of the light, hence this results in interference colors. Thus, the isotropic part of the sample appears dark and the anisotropic parts in color. The presence of liquid crystals (LCs) in the fibers was verified using POM. The images were taken in transmission mode using Olympus (BX51) optical polarizing light microscope. The details on working and importance of crossed polarizers are discussed in chapter 3.

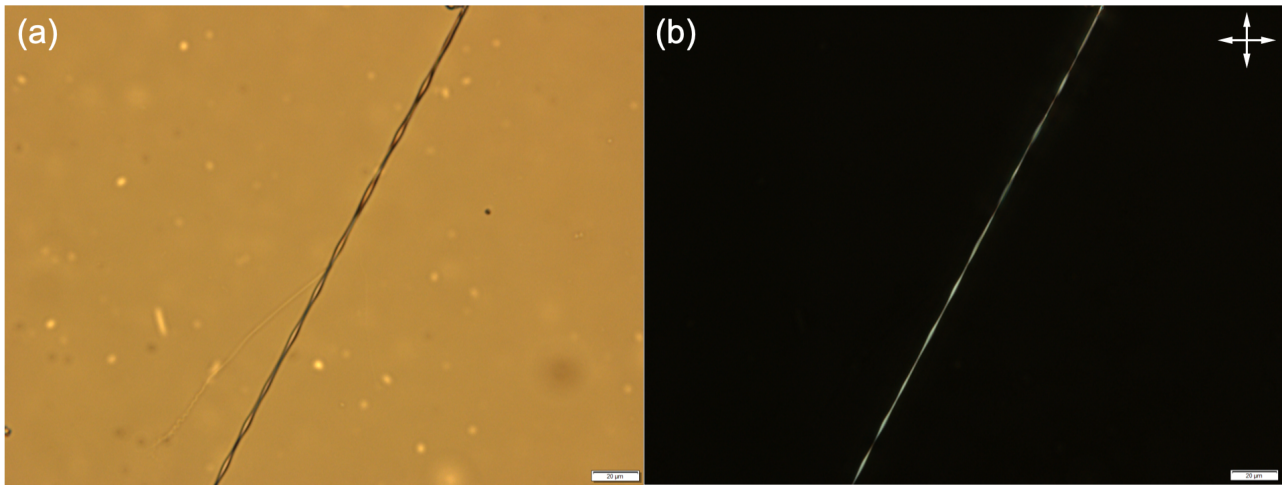

Figure 7.2: Sample POM image of a PAA fiber with LC core, spun from a 10 % w/w of PAA in anhydrous ethanol sheath solution, observed (a) without and (b) in between crossed polarizors. Because of the optical birefringence of LC, the fibers appear brighter, when observed between crossed polarizors.

7.3 Scanning Electron Microscopy (SEM)

The scanning electron microscope (SEM) uses a focused beam of high-energy electrons to generate a detailed image from the electron-sample interaction revealing information including the morphology of the sample.

7.3.1 Sample preparation

Since the SEM uses electrons, the sample must be conductive to avoid charging. Charging, in SEM, is a term used to describe the situation when there are insufficient electrons flowing from top of the sample to the ground (the sample holder) as the SEM beam scans the sample. This results in accumulation of charge at the surface of the sample and the image produced is blurred. The electrospun fibers in this study are not conductive and hence needed to be coated. The sample was glued to a stub and placed in a sample holder and coated with a 5nm gold layer using the Quorum Q150RS sputter coater.

After coating, the morphology of the electrospun fibers was characterized using the JEOL JSM-6010LA Scanning Electron Microscope (SEM, Akishima, Japan). The fibers were imaged at multiple locations with different magnifications. Since the samples were attached to the sample holder, only top view of the fiber was captured.

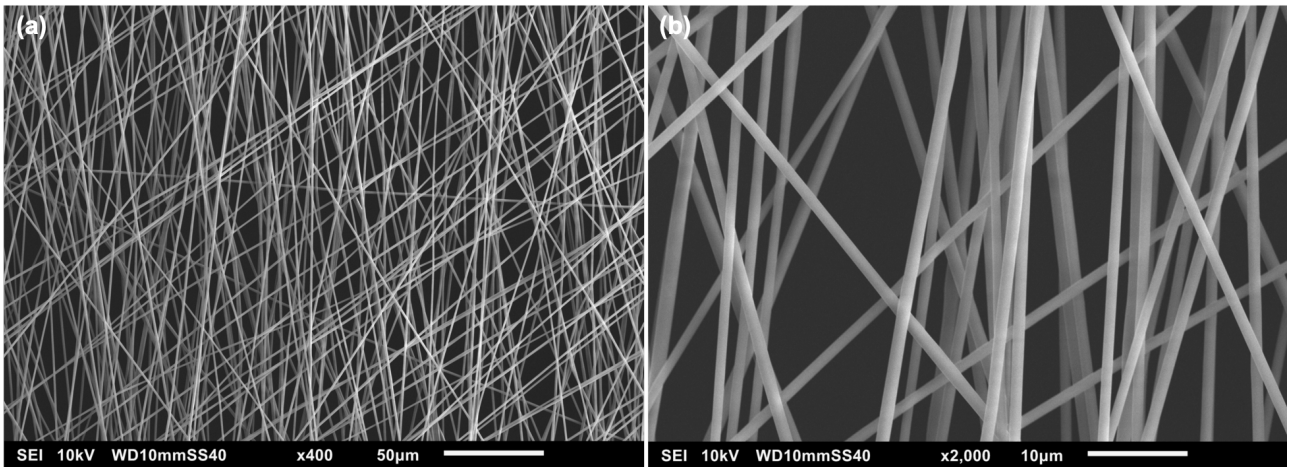

Figure 7.3: Sample SEM image of PAA fibers spun from a 10% w/w PAA in anhydrous ethanol solution captured at different magnifications: (a) at 400x and (b) at 2000x.

7.4 Viscosity measurements: Rheometer

The viscosity (η) of the polymer solutions was measured using an Anton Paar rheometer (MRC-102) with a parallel plate (one stationary and the other rotating) geometry and controlled by Rheocompass software. While in operation the rheometer measures the torque and speed with high accuracy. The measuring head of the rheometer contains the drive motor and encoder to measure and set the torque and speed. The viscosity of the polymer solution is not measured directly but calculated according to the viscosity law from the quotients of the shear stress (τ) and shear rate ($\dot{\gamma}$) using equation 7.3.

$$\eta = \frac{\tau}{\dot{\gamma}} \tag{7.3}$$

The shear stress correlates with the torque and shear rate with the speed. In addition, the temperature, an important parameter is measured by the equipment as well.

7.5 Interfacial tension measurement

The surface and interfacial tension (γ) measurements were performed at room temperature using the pendant drop tensiometer (OCA 15EC from Dataphysics). The equipment setup (figure 7.5) includes a camera, a movable stage, a syringe (filled with the sample fluid) and a needle. The whole system is connected to a computer and controlled with a dedicated software.

A pendant drop is formed at the tip of the needle and its shape results from the relationship of two forces between the surface or interfacial tension and gravity. This drop is imaged from a camera and from its shape and size, surface (against air) or interfacial tension (against a liquid) is measured using the equation 7.4 mentioned below. To measure the interfacial tension, a bath of an ambient or surrounding liquid is prepared and the needle inserted in the bath to generate the pendant drop inside the bath. For optical analysis the ambient phase or surrounding bath has to be transparent.

$$\gamma = \Delta\rho g \frac{R_0}{\beta} \tag{7.4}$$

where γ is the surface/interfacial tension, $\Delta\rho$ is the density difference between fluids, g is the gravitational constant, R_0 is the drop radius of curvature at the apex and β is the shape factor, which can be defined through the Young-Laplace equation expressed as three dimensionless first-order equations as shown in the figure 7.4.

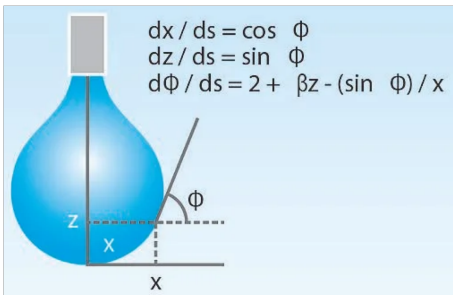

Figure 7.4: Pendant drop schematic and measurement for surface/interfacial tension. Schematics adapted from the Dataphysics equipment user manual.

7.5.1 Sample preparation

The software to measure the surface and interfacial tension, requires density of the solutions to entered for a correct and accurate measurement. In this study, the density of the polymer solutions and LC was measured (at room temperature) using Mettler Toledo DE45 Delta range density meter.

The needle used for the experiment should be clean of all the impurities. In the experiments used for this study the needle was first flushed with ethanol, rinsed with water to wash off all the ethanol, then sonicated in a bath for 20 mins, rinsed with water and dried with compressed air at room temperature before using it for the measurements. For interfacial tension measurements a bath of polymer solution was prepared in 3.5 mL quartz cuvette and the needle was dipped inside the bath. The drop phase, LC, was slowly introduced into the bath or ambient phase at a low flow rate (on the scale of 0.01-1 μL/s) and the corresponding pendant drop was formed was imaged and the value was measured using the software.

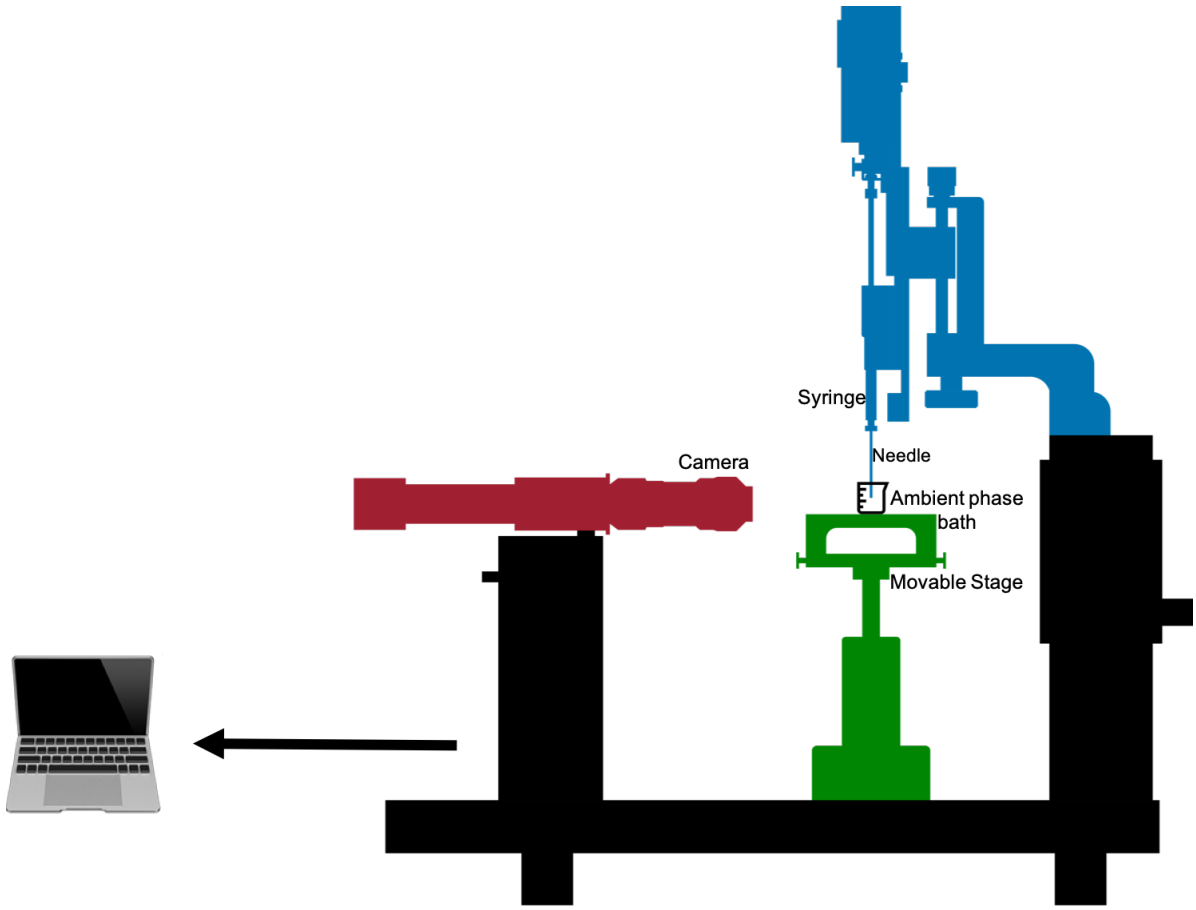

Figure 7.5: A sketch of the equipment used for surface and interfacial tension measurements with labelled parts. Surface tension measurements were carried out against air and the ambient phase bath was used only for interfacial tension measurements. The diameter of the stainless steel needle used was 0.51 mm, and it was provided by the manufacturer, Dataphysics. Schematics adapted from the Dataphysics equipment user manual.

Chapter 8

Summary & outlook

This thesis aims at contributing to the fundamental understanding of the effects of partial miscibility and solvent combinations on coaxial electrospinnability, Taylor cone stability, and resultant core-sheath structural integrity. Three different systems, one each of completely miscible, partially miscible and immiscibile core-sheath were studied. Their Taylor cones were systematically analyzed during electrospinning and their interfacial tensions were measured. We showed that production of fibers with continuous core sheath morphology could be achieved using partial miscibility. A common solvent for core and sheath imparts partial miscibility and, reduces the interfacial tension between the two producing a distinct core–sheath interface that can be maintained throughout the spinning process. Complete miscibility eliminates the core-sheath morphology, while immiscibility causes the core to break-up inside the Taylor cone and even preventing it from entering the fiber-producing jet because of a relatively high interfacial tension. Even though our experiments were performed with LC cores we believe that our conclusions are applicable to any other core-sheath combination.

Electrospinning of polymer solutions to produce multifunctional composite fibers is a delicate balance of multiple parameters, including mixtures of multiple solvents, to achieve the desired outcome. In this context, poly(acrylic acid) is interesting, as it is readily soluble in water as well as ethanol. Viscosity is a good probe for solvent-polymer interaction and the electrospinnability changes when poly(acrylic acid) (PAA) is dissolved in ethanol–water mixtures at varying mixing ratio. There was a pronounced peak noticed in the viscosity values at a water-to-ethanol molar ratio of about 2:1, possibly due to the partial deprotonation of carboxylate groups by water while the ethanol dissolves the remaining uncharged polymer fraction. An optimum viscosity window was identified for consistent electrospinning of any water-ethanol solvent ratio.

Finally, PAA and PVA were combined (with equal number of functional groups to get the maximum crosslinking) in the sheath using a mixed solvent of water and ethanol. The fibers

produced were thermally crosslinked after spinning, and were easily manipulated by hand and even fully immersed in water without dissolving and losing their functional LC core. In addition to the nematic LC, PVA/PAA fibers with cholesteric cores were also successfully produced with the core remaining intact after thermal crosslinking. However, to spin fibers with cholesteric cores, the solvent had to be changed from ethanol to 1,4-dioxane as the chiral dopant to prepare the cholesteric mixture, CB15, is chemically similar to 5CB, resulting in a problematic isotropic–isotropic phase separation in mixtures with ethanol and water. The cholesteric filled fibers were thin (diameter 1-5 μm) and the selective reflection was not observed with the unaided eye but the core presence was confirmed using a POM. The core's appearance was more pronounced upon immersion in water, due to the removal of sheath scattering.

Though a lot was achieved in this thesis, it still leaves scope to continue the research further. Cholesteric-filled PVA/PAA fibers of higher diameter need to be electrospun and crosslinked to observe the colors with naked-eye, eliminating the need for microscope. This could be a positive leap in the direction of LC wearable sensors. The current recipe of using equal number of carboxyl and hydroxyl functional groups to achieve maximum crosslinking makes the fibers stiff and brittle. Ideally, the degree of crosslinking can be lowered by tuning the number of functional groups to electrospin a cholesteric filled stretchable fiber mat.

Apart from being fascinating, electrospinning is also a simple(r) fiber production methods. The components to build a setup for electrospinning can be assembled using basic tools. From this point, two important areas to further dive in would be to study the challenges of upscaling from a laboratory-based spinning setup to an industrial scale production. The setup used for the experiments for this research was home built in the laboratory. Therefore, upgrading it to an industrial scale and the challenges encountered, including technical, scientific and logistical and more could also make an interesting research topic. Finally, following Prof Manu Prakash's inspiration of frugal science [116], an interesting study would to make electrospun fibers using everyday basic tools. For example, a kitchen ladle or sieve can serve as collectors, to deposit the fibers and then analyzing them with a smartphone as a microscope [117]. The idea is to formulate a setup or protocol where everybody (including non-technical people) could spin useful and functional fibers with basic tools available.

The spinneret design plays an important role in producing a symmetrical Taylor cone and filling of the fibers in general, especially the position of the core needle in the spinneret. Another interesting study could be to observe and analyze the effects of positioning of the inner needle in the spinneret (shorter, inline and longer than the outer needle). A systematic study of how it affects the shape of Taylor cone and filling of the fibers would be valuable.

Bibliography

[1] Y. K. Doğan, A. Demirural, and T. Baykara, "Single-needle electrospinning of PVA hollow nanofibers for core–shell structures," *SN Applied Sciences*, vol. 1, pp. 1–7, 5 2019.

[2] L. W. Honaker, *Liquid Metals and Liquid Crystals Subject to Flow: From Fundamental Fluid Physics to Functional Fibers*. PhD thesis, University of Luxembourg, 2019.

[3] T. Sakai, "Polymer Solution," *Physics of Polymer Gels*, pp. 23–43, 4 2020.

[4] C. G. Reyes, "Confined in a fiber: Realizing flexible gas sensors by electrospinning liquid crystals," 2019.

[5] E. Enz and J. Lagerwall, "Electrospun microfibres with temperature sensitive iridescence from encapsulated cholesteric liquid crystal," *Journal of Materials Chemistry*, vol. 20, pp. 6866–6872, 8 2010.

[6] J. Wang, A. Jákli, and J. L. West, "Morphology Tuning of Electrospun Liquid Crystal/Polymer Fibers," *ChemPhysChem*, vol. 17, pp. 3080–3085, 10 2016.

[7] J. Wang, A. Jákli, and J. L. West, "Airbrush Formation of Liquid Crystal/Polymer Fibers," *ChemPhysChem*, vol. 16, pp. 1839–1841, 6 2015.

[8] J. L. West, J. R. Wang, and A. Jákli, "Airbrushed Liquid Crystal/Polymer Fibers for Responsive Textiles," *Advances in Science and Technology*, vol. 100, pp. 43–49, 10 2017.

[9] C. G. Reyes, A. Sharma, and J. P. F. Lagerwall, "Non-electronic gas sensors from electrospun mats of liquid crystal core fibres for detecting volatile organic compounds at room temperature," *Liquid Crystals*, vol. 43, pp. 1986–2001, 12 2016.

[10] J. Wang, A. Jákli, and J. West, "Liquid crystal/polymer fiber mats as sensitive chemical sensors," *Journal of Molecular Liquids*, vol. 267, pp. 490–495, 2018.

[11] M. D. Thum, D. C. Ratchford, R. Casalini, J. H. Wynne, and J. G. Lundin, "Azobenzene-Doped Liquid Crystals in Electrospun Nanofibrous Mats for Photochemical Phase Control," *ACS Applied Nano Materials*, vol. 4, pp. 297–304, 1 2021.

[12] D. Li and Y. Xia, "Electrospinning of Nanofibers: Reinventing the Wheel?," *Advanced Materials*, vol. 16, pp. 1151–1170, 7 2004.

[13] J. Doshi, D. R. J. o. Electrostatics, and U. 1995, "Electrospinning process and applications of electrospun fibers," *Journal of Electrostatics*, vol. 35, no. 2-3, pp. 151–160, 1995.

[14] S. van der Heijden, L. Daelemans, K. De Bruycker, R. Simal, I. De Baere, W. Van Paepegem, H. Rahier, and K. De Clerck, "Novel composite materials with tunable delamination resistance using functionalizable electrospun SBS fibers," *Composite Structures*, vol. 159, pp. 12–20, 1 2017.

[15] S. Ribeiro, P. Costa, C. Ribeiro, V. Sencadas, G. Botelho, and S. Lanceros-Méndez, "Electrospun styrene–butadiene–styrene elastomer copolymers for tissue engineering applications: Effect of butadiene/styrene ratio, block structure, hydrogenation and carbon nanotube loading on physical properties and cytotoxicity," *Composites Part B: Engineering*, vol. 67, pp. 30–38, 12 2014.

[16] Formhals Anton, "Process and apparatus for preparing artificial threads," 12 1934.

[17] D. Reneker and I. Chun, "Nanometre diameter fibres of polymer, produced by electrospinning," *iopscience.iop.org*, vol. 7, pp. 216–223, 1996.

[18] L. Wang and A. Ryan, "Introduction to electrospinning," *Electrospinning for tissue regeneration*, pp. 3–33, 2011.

[19] G. Scalia, E. Enz, O. Calò, D. K. Kim, M. Hwang, J. H. Lee, and J. P. Lagerwall, "Morphology and core continuity of liquid-crystal-functionalized, coaxially electrospun fiber mats tuned via the polymer sheath solution," *Macromolecular Materials and Engineering*, vol. 298, pp. 583–589, 5 2013.

[20] D. K. Kim, M. Hwang, and J. P. F. Lagerwall, "Liquid crystal functionalization of electrospun polymer fibers," *Journal of Polymer Science Part B: Polymer Physics*, vol. 51, pp. 855–867, 6 2013.

[21] E. Enz, V. La Ferrara, and G. Scalia, "Confinement-sensitive optical response of cholesteric liquid crystals in electrospun fibers," *ACS Nano*, vol. 7, pp. 6627–6635, 8 2013.

[22] J. Lagerwall, J. McCann, E. Formo, G. Scalia, and X. Younan, "Coaxial electrospinning of microfibres with liquid crystal in the core," *Chemical Communications*, no. 42, pp. 5420–5422, 2008.

[23] R. Gopal, S. Kaur, Z. Ma, C. Chan, and S. Ramakrishna, "Electrospun nanofibrous filtration membrane," *Journal of Membrane Science*, vol. 281, no. 1-2, pp. 581–586, 2006.

[24] R. Uppal, G. Ramaswamy, C. Arnold, R. Goodband, and Y. Wang, "Hyaluronic acid nanofiber wound dressing—production, characterization, and in vivo behavior," *Journal of Biomedical Material Research*, vol. 97B, no. 1, pp. 20–29, 2011.

[25] J. Díaz, A. Barrero, and M. Márquez, "Controlled encapsulation of hydrophobic liquids in hydrophilic polymer nanofibers by co-electrospinning," *Advanced Functional Materials*, vol. 16, pp. 2110–2116, 10 2006.

[26] P. Rathore and J. D. Schiffman, "Beyond the Single-Nozzle: Coaxial Electrospinning Enables Innovative Nanofiber Chemistries, Geometries, and Applications," *ACS Applied Materials and Interfaces*, vol. 13, pp. 48–66, 1 2021.

[27] D. Han and A. J. Steckl, "Coaxial Electrospinning Formation of Complex Polymer Fibers and their Applications," *ChemPlusChem*, vol. 84, pp. 1453–1497, 10 2019.

[28] A. L. Yarin, "Coaxial electrospinning and emulsion electrospinning of core-shell fibers," *Polymers for Advanced Technologies*, vol. 22, pp. 310–317, 3 2011.

[29] S. Lee and S. K. Obendorf, "Use of Electrospun Nanofiber Web for Protective Textile Materials as Barriers to Liquid Penetration," *Textile Research Journal*, vol. 77, no. 9, pp. 696–702, 2007.

[30] G. C. Rutledge and S. V. Fridrikh, "Formation of fibers by electrospinning," *Advanced Drug Delivery Reviews*, vol. 59, no. 14, pp. 1384–1391, 2007.

[31] A. Andrady, *Science and technology of polymer nanofibers*. John Wiley & Sons, Ltd, 2008.

[32] D. H. Reneker and A. L. Yarin, "Electrospinning jets and polymer nanofibers," *Polymer*, vol. 49, no. 10, pp. 2387–2425, 2008.

[33] S. Reznik, A. Yarin, and A. Theron, "Transient and steady shapes of droplets attached to a surface in a strong electric field," *Journal of Fluids*, vol. 516, pp. 349–377, 2004.

[34] G. Taylor, "Electrically driven jets," *Proceedings of the Royal Society*, vol. 313, pp. 453–475, 1969.

[35] D. H. Reneker, A. L. Yarin, H. Fong, and S. Koombhongse, "Bending instability of electrically charged liquid jets of polymer solutions in electrospinning," *Journal of Applied Physics*, vol. 87, no. 9 I, pp. 4531–4547, 2000.

[36] Y. Shin, M. Hohman, and M. Brenner, "Electrospinning: A whipping fluid jet generates submicron polymer fibers," *Applied Physics Letters*, vol. 78, pp. 1149–1151, 2 2001.

[37] R. D. Smith, J. A. Loo, C. G. Edmonds, C. J. Barinaga, and H. R. Udseth, "New Developments in Biochemical Mass Spectrometry: Electrospray Ionization," *Analytical Chemistry*, vol. 62, pp. 882–899, 4 1990.

[38] A. Martins, R. Reis, N. N. I. M. Reviews, and u. 2008, "Electrospinning: processing technique for tissue engineering scaffolding," *Taylor & Francis*, vol. 53, pp. 257–274, 9 2008.

[39] S. Chuangchote, T. Sagawa, and S. Yoshikawa, "Electrospinning of poly(vinyl pyrrolidone): Effects of solvents on electrospinnability for the fabrication of poly(p-phenylene vinylene) and TiO2 nanofibers," *Journal of Applied Polymer Science*, vol. 114, pp. 2777–2791, 12 2009.

[40] H. Fong, I. Chun, D. R. Polymer, and U. 1999, "Beaded nanofibers formed during electrospinning," *Polymer*, vol. 40, no. 16, pp. 4585–4592, 1999.

[41] L. W. Honaker, A. Sharma, A. Schanen, and J. P. F. Lagerwall, "Measuring the Anisotropy in Interfacial Tension of Nematic Liquid Crystals," *Crystals 2021, Vol. 11, Page 687*, vol. 11, p. 687, 6 2021.

[42] D. G. Yu, K. White, J. H. Yang, X. Wang, W. Qian, and Y. Li, "PVP nanofibers prepared using co-axial electrospinning with salt solution as sheath fluid," *Materials Letters*, vol. 67, pp. 78–80, 1 2012.

[43] K. Morota, H. Matsumoto, T. Mizukoshi, Y. K. cience, interface, and U. 2004, "Poly (ethylene oxide) thin films produced by electrospray deposition: morphology control and additive effects of alcohols on nanostructure," *Journal of Colloid and Interface Science*, vol. 279, no. 2, pp. 484–492, 2004.

[44] R. V. Krishnappa, K. Desai, and C. Sung, "Morphological study of electrospun polycarbonates as a function of the solvent and processing voltage," *Journal of Materials Science*, vol. 38, no. 11, pp. 2357–2365, 2003.

[45] S. Koombhongse, W. Liu, and D. H. Reneker, "Flat polymer ribbons and other shapes by electrospinning," *Journal of Polymer Science Part B: Polymer Physics*, vol. 39, pp. 2598–2606, 11 2001.

[46] C. Zhang, X. Yuan, L. Wu, Y. Han, and J. Sheng, "Study on morphology of electrospun poly(vinyl alcohol) mats," *European Polymer Journal*, vol. 41, pp. 423–432, 3 2005.

[47] M. Demir, I. Yilgor, E. Yilgor, and B. Erman, "Electrospinning of polyurethane fibers," *Polymer*, vol. 43, pp. 3303–3309, 5 2002.

[48] S. De Vrieze, T. Van Camp, A. Nelvig, B. Hagström, P. Westbroek, and K. De Clerck, "The effect of temperature and humidity on electrospinning," *Journal of Materials Science*, 2009.

[49] S. Tripatanasuwan, Z. Zhong, and D. H. Reneker, "Effect of evaporation and solidification of the charged jet in electrospinning of poly(ethylene oxide) aqueous solution," *Polymer*, vol. 48, pp. 5742–5746, 9 2007.

[50] I. Loscertales, A. Barrero, I. Guerrero, R. C. . . . , and U. 2002, "Micro/nano encapsulation via electrified coaxial liquid jets," *Science*, vol. 286, no. 5560, p. 5191, 2002.

[51] Z. Sun, E. Zussman, A. L. Yarin, J. H. Wendorff, and A. Greiner, "Compound Core-Shell Polymer Nanofibers by Co-Electrospinning," *Advanced Materials*, 2003.

[52] D. L. and and Y. Xia*, "Direct Fabrication of Composite and Ceramic Hollow Nanofibers by Electrospinning," *Nano Letters*, vol. 4, pp. 933–938, 5 2004.

[53] I. G. Loscertales, A. Barrero, M. Márquez, R. Spretz, R. Velarde-Ortiz, , and G. Larsen, "Electrically Forced Coaxial Nanojets for One-Step Hollow Nanofiber Design," *Journal of the American Chemical Society*, vol. 126, pp. 5376–5377, 5 2004.

[54] A. E. Mamuk, Koçak, and E. Demirci Dönmez, "Production and characterization of liquid crystal/polyacrylonitrile nano-fibers by electrospinning method," *Colloid and Polymer Science*, vol. 299, pp. 1209–1221, 7 2021.

[55] e. a. Jasiurkowska-Delaporte, Małgorzata, "Soft versus hard confinement effects on the phase transitions, and intra-and inter-molecular dynamics of 6BT liquid crystal constrained in electrospun polymer," *Journal of Molecular Liquids*, vol. 331, no. 115817, 2021.

[56] H. J. Yu, S. V. Fridrikh, and G. C. Rutledge, "Production of submicrometer diameter fibers by two-fluid electrospiiming," *Advanced Materials*, vol. 16, pp. 1562–1566, 9 2004.

[57] M. J. Bertocchi, D. C. Ratchford, R. Casalini, J. H. Wynne, and J. G. Lundin, "Electrospun Polymer Fibers Containing a Liquid Crystal Core: Insights into Semi-Flexible Confinement," *Journal of Physical Chemistry C*, vol. 122, pp. 16964–16971, 7 2018.

[58] E. Zussman, A. L. Yarin, A. V. Bazilevsky, R. Avrahami, and M. Feldman, "Electrospun polyacrylonitrile/poly(methyl methacrylate)-derived turbostratic carbon micro-/nanotubes," *Advanced Materials*, vol. 18, pp. 348–353, 2 2006.

[59] J. Lin, C. Chen, L. Chen, Y. C. O. . . . , and U. 2016, "Morphological appearances and photo-controllable coloration of dye-doped cholesteric liquid crystal/polymer coaxial microfibers fabricated by coaxial electrospinning," *OSA Publishing*, vol. 24, no. 3, p. 3112, 2016.

[60] S. Vats, M. Anyfantakis, L. W. Honaker, F. Basoli, and J. P. F. Lagerwall, "Stable Electrospinning of Core-Functionalized Coaxial Fibers Enabled by the Minimum-Energy Interface Given by Partial Core–Sheath Miscibility," *Langmuir*, vol. 37, pp. 13265–13277, 11 2021.

[61] J. T. McCann, M. Marquez, and Y. Xia, "Melt coaxial electrospinning: A versatile method for the encapsulation of solid materials and fabrication of phase change nanofibers," *Nano Letters*, vol. 6, pp. 2868–2872, 12 2006.

[62] C. He, Z. Huang, X. Han, L. L. cience, P. B, and u. 2006, "Coaxial Electrospun Poly(L-Lactic Acid) Ultrafine Fibers for Sustained Drug Delivery," *Taylor & Francis*, vol. 45 B, pp. 515–524, 8 2006.

[63] Y. Zhao, X. Cao, L. J. J. o. t. A. Chemical, and u. 2007, "Bio-mimic multichannel microtubes by a facile method," *ACS Publications*, vol. 129, pp. 764–765, 1 2007.

[64] K. H. K. Chan and M. Kotaki, "Fabrication and morphology control of poly(methyl methacrylate) hollow structures via coaxial electrospinning," *Journal of Applied Polymer Science*, vol. 111, pp. 408–416, 1 2009.

[65] J. Park, P. B. A. materials, and u. 2010, "Coaxial electrospinning of self-healing coatings," *Wiley Online Library*, vol. 21, pp. 1–4, 1 2009.

[66] C. He, Z. Huang, and X. Han, "Fabrication of drug-loaded electrospun aligned fibrous threads for suture applications," *Journal of Biomedical Material Research*, vol. 89, pp. 80–95, 4 2008.

[67] H. Chen, N. Wang, J. Di, Y. Zhao, Y. Song, and L. Jiang, "Nanowire-in-microtube structured core/shell fibers via multifluidic coaxial electrospinning," *Langmuir*, vol. 26, pp. 11291–11296, 7 2010.

[68] T. Yuan, B. Zhao, R. Cai, Y. Zhou, Z. S. J. o. M. Chemistry, and u. 2011, "Electrospinning based fabrication and performance improvement of film electrodes for lithium-ion batteries composed of TiO 2 hollow fibers," *pubs.rsc.org*, vol. 21, pp. 15041–15048, 9 2011.

[69] S. Jiang, G. Duan, E. Zussman, A. Greiner, and S. Agarwal, "Highly flexible and tough concentric triaxial polystyrene fibers," *ACS Applied Materials and Interfaces*, vol. 6, pp. 5918–5923, 4 2014.

[70] Y. Lu, X. Xiao, J. Fu, C. Huan, S. Qi, Y. Zhan, and Y. Zhu, "Novel smart textile with phase change materials encapsulated core-sheath structure fabricated by coaxial electrospinning," *Chemical Engineering Journal*, vol. 335, pp. 532–539, 2019.

[71] F. R. M. f. Chemie and u. 1888, "Beiträge zur kenntniss des cholesterins," *zobodat.at*, vol. 9, pp. 421–441, 1888.

[72] J. V. Selinger, "Introduction to the Theory of Soft Matter," 2016.

[73] A. Jakli and A. Saupe, "One- and Two-Dimensional Fluids : Properties of Smectic, Lamellar and Columnar Liquid Crystals," *One- and Two-Dimensional Fluids*, 5 2006.

[74] I. Dierking, "One- and two-dimensional fluids," in *Liquid Crystals Today*, vol. 18, pp. 28–29, Taylor & Francis, 6 2009.

[75] Z. S. Davidson, *Assembly, Elasticity, and Structure of Lyotropic Chromonic Liquid Crystals and Disordered Colloids*. PhD thesis, 2017.

[76] P. Collings and J. Goodby, *Introduction to liquid crystals: chemistry and physics*. 2019.

[77] F. Berride, E. Troche-Pesqueira, G. Feio, E. J. Cabrita, T. Sierra, A. Navarro-Vázquez, and M. M. Cid, "Chiral amplification of disodium cromoglycate chromonics induced by a codeine derivative," *Soft Matter*, vol. 13, no. 38, pp. 6810–6815, 2017.

[78] W. Iglesias, N. L. Abbott, E. K. Mann, and A. Jákli, "Improving liquid-crystal-based biosensing in aqueous phases," *ACS Applied Materials and Interfaces*, vol. 4, pp. 6884–6890, 12 2012.

[79] A. Jákli, O. D. Lavrentovich, and J. V. Selinger, "Physics of liquid crystals of bent-shaped molecules," *Reviews of Modern Physics*, vol. 90, 11 2018.

[80] J. Stelzer, R. Berardi, C. Z. M. C. Liquid, , and u. 2000, "Flexoelectric coefficients for model pear shaped molecules from monte carlo simulations," *Taylor & Francis*, vol. 352, no. 1, pp. 187–194, 2000.

[81] P. D. Gennes and J. Prost, *The physics of liquid crystals*. 1993.

[82] H. G. Lee, S. Munir, and S. Y. Park, "Cholesteric Liquid Crystal Droplets for Biosensors," *ACS Applied Materials and Interfaces*, vol. 8, pp. 26407–26417, 10 2016.

[83] M. Lee, Y. Sung, Y. Hsiao, and W. L. XX, "Chiral liquid crystals as biosensing platforms," *SPIE Digital Library*, vol. 9940, 2016.

[84] H.-S. Kitzerow and C. Bahr, "Introduction," *Chirality in Liquid Crystals*, pp. 1–27, 4 2006.

[85] C. Oseen, "The theory of liquid crystals," *Transactions of the Faraday Society*, vol. 29, pp. 883–899, 1933.

[86] P. Harris and P. Harris, *Carbon nanotube science: synthesis, properties and applications*. 2009.

[87] M. Dresselhaus, G. Dresselhaus, and P. Eklund, *Science of fullerenes and carbon nanotubes: their properties and applications*. 1996.

[88] U. Mur, S. Čopar, G. Posnjak, I. Muševič, M. Ravnik, and S. Žumer, "Ray optics simulations of polarised microscopy textures in chiral nematic droplets," *Liquid Crystals*, vol. 44, pp. 679–687, 3 2017.

[89] I. Dierking, *Textures of liquid crystals*. 2003.

[90] A. Rudin and P. Choi, "Practical Aspects of Molecular Weight Measurements," *The Elements of Polymer Science & Engineering*, pp. 89–148, 1 2013.

[91] A. Grosberg, A. Khokhlov, and T. Halsey, "Giant molecules: here, there, and everywhere," *Physics Today*, vol. 51, no. 2, p. 73, 1998.

[92] H. Elias, "Theta solvents," in *Encyclopedic Dictionary of Polymers*, pp. 975–976, 4 2007.

[93] Steyaert Iline, *Electrospinning and morphology characterization of polymer blend nanofibers*. PhD thesis, Ghent University, Ghent, 2016.

[94] T. McLeish, "Tube theory of entangled polymer dynamics," *Advances in Physics*, vol. 51, pp. 1379–1527, 9 2010.

[95] M. Abadi, M. F. Serag, and S. Habuchi, "Entangled polymer dynamics beyond reptation," *Nature Communications 2018 9:1*, vol. 9, pp. 1–12, 11 2018.

[96] P. Gupta, C. Elkins, T. Long, and G. Wilkes, "Electrospinning of linear homopolymers of poly (methyl methacrylate): exploring relationships between fiber formation, viscosity, molecular weight and concentration," *Polymer*, vol. 46, no. 13, pp. 4799–4810, 2005.

[97] B. Oktay, N. Kayaman-Apohan, and S. Erdem-Kuruca, "Fabrication of nanofiber mats from electrospinning of functionalized polymers," *IOP Conference Series: Materials Science and Engineering*, vol. 64, p. 012011, 8 2014.

[98] M. Avadanei, "Photocrosslinking of 1, 2-polybutadiene and characteristics of the crosslinked system," *Journal of Macromolecular Science, Part B: Physics*, vol. 51, pp. 313–327, 2 2012.

[99] K. Kumeta, I. Nagashima, S. Matsui, and K. Mizoguchi, "Crosslinking reaction of poly(vinyl alcohol) with poly(acrylic acid) (PAA) by heat treatment: Effect of neutralization of PAA," *Journal of Applied Polymer Science*, vol. 90, pp. 2420–2427, 11 2003.

[100] J.-W. Rhim, M.-Y. Sohn, H.-J. Joo, and K.-H. Lee, "Pervaporation separation of binary organic-aqueous liquid mixtures using crosslinked PVA membranes. I. Characterization of the reaction between PVA and PAA," *Journal of Applied Polymer Science*, vol. 50, pp. 679–684, 10 1993.

[101] H. Butt, K. Graf, and M. Kappl, "Physics and Chemistry of Interfaces," *Physics and Chemistry of Interfaces*, 9 2003.

[102] J. G. Speight, "Test Methods for Asphalt Binders," *Asphalt Materials Science and Technology*, pp. 137–203, 1 2016.

[103] P.-G. d. Gennes, F. Brochard-Wyart, and D. Quéré, "Capillarity and Gravity," *Capillarity and Wetting Phenomena*, pp. 33–67, 2004.

[104] L. Rayleigh, "On The Instability Of Jets," *Proceedings of the London Mathematical Society*, vol. s1-10, pp. 4–13, 11 1878.

[105] J. W. Strutt, "On the instability of a cylinder of viscous liquid under capillary force.," *PHILOS. MAG.*, vol. 34 , 1892, pp. 145–154, 1976.

[106] E. A. Buyuktanir, M. W. Frey, and J. L. West, "Self-assembled, optically responsive nematic liquid crystal/polymer core-shell fibers: Formation and characterization," *Polymer*, vol. 51, pp. 4823–4830, 10 2010.

[107] E. Enz, "Electrospun Polymer - Liquid Crystal Composite Fibres {THESIS}," pp. 1–147, 2013.

[108] C. G. Reyes and J. P. Lagerwall, "Disruption of Electrospinning due to Water Condensation into the Taylor Cone," *ACS Applied Materials and Interfaces*, vol. 12, pp. 26566–26576, 6 2020.

[109] A. Sharma and J. P. Lagerwall, "Electrospun composite liquid crystal elastomer fibers," *Materials*, vol. 11, no. 3, 2018.

[110] K. Schelski, C. G. Reyes, L. Pschyklenk, P.-M. Kaul, and J. Lagerwall, "Quantitative Volatile Organic Compound (VOC) Sensing with Liquid Crystal Core Fibers," *SSRN Electronic Journal*, 5 2021.

[111] E. A. Buyuktanir, J. L. West, and M. W. Frey, "Optically responsive liquid crystal microfibers for display and nondisplay applications," *https://doi.org/10.1117/12.880076*, vol. 7955, pp. 135–141, 2 2011.

[112] L. Pschyklenk, T. Wagner, A. Lorenz, and P. Kaul, "Optical Gas Sensing with Encapsulated Chiral-Nematic Liquid Crystals," *ACS Applied Polymer Materials*, vol. 2, pp. 1925–1932, 5 2020.

[113] Y. Yang, M. Zhang, Z. Ju, P. Y. Tam, T. Hua, M. W. Younas, H. Kamrul, and H. Hu, "Poly(lactic acid) fibers, yarns and fabrics: Manufacturing, properties and applications," *Textile Research Journal*, vol. 91, pp. 1641–1669, 7 2021.

[114] D. W. Farrington, J. Lunt, S. Davies, and R. S. Blackburn, "Poly(lactic acid) fibers (PLA)," *Polyesters and Polyamides*, pp. 140–170, 1 2008.

[115] G. Gorrasi and R. Pantani, "Hydrolysis and Biodegradation of Poly(lactic acid)," *Advances in Polymer Science*, vol. 279, pp. 119–151, 2017.

[116] "Frugal Science and Global Health – PRAKASH LAB."

[117] A. Orth, E. R. Wilson, J. G. Thompson, and B. C. Gibson, "A dual-mode mobile phone microscope using the onboard camera flash and ambient light," *Scientific Reports 2018 8:1*, vol. 8, pp. 1–8, 2 2018.

1

LANGMUIR

pubs.acs.org/Langmuir Article

Stable Electrospinning of Core-Functionalized Coaxial Fibers Enabled by the Minimum-Energy Interface Given by Partial Core–Sheath Miscibility

Shameek Vats, Manos Anyfantakis, Lawrence W. Honaker, Francesco Basoli, and Jan P. F. Lagerwall*

Cite This: *Langmuir* 2021, 37, 13265–13277 Read Online

ACCESS | Metrics & More | Article Recommendations | Supporting Information

ABSTRACT: Core–sheath electrospinning is a powerful tool for producing composite fibers with one or multiple encapsulated functional materials, but many material combinations are difficult or even impossible to spin together. We show that the key to success is to ensure a well-defined core–sheath interface while also maintaining a constant and minimal interfacial energy across this interface. Using a thermotropic liquid crystal as a model functional core and polyacrylic acid or styrene-butadiene-styrene block copolymer as a sheath polymer, we study the effects of using water, ethanol, or tetrahydrofuran as polymer solvent. We find that the ideal core and sheath materials are partially miscible, with their phase diagram exhibiting an inner miscibility gap. Complete immiscibility yields a relatively high interfacial tension that causes core breakup, even preventing the core from entering the fiber-producing jet, whereas the lack of a well-defined interface in the case of complete miscibility eliminates the core–sheath morphology, and it turns the core into a coagulation bath for the sheath solution, causing premature gelation in the Taylor cone. Moreover, to minimize Marangoni flows in the Taylor cone due to local interfacial tension variations, a small amount of the sheath solvent should be added to the core prior to spinning. Our findings resolve a long-standing confusion regarding guidelines for selecting core and sheath fluids in core–sheath electrospinning. These discoveries can be applied to many other material combinations than those studied here, enabling new functional composites of large interest and application potential.

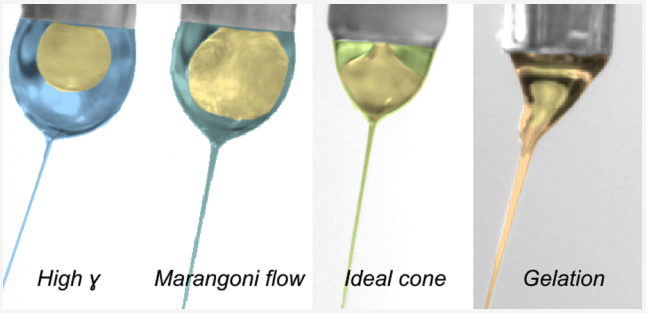

INTRODUCTION

Although the idea of making fibers by electrospinning is approaching its centennial anniversary,[1] it has only been in the last two decades that the technique has truly flourished.[2−8] The introduction of core–sheath electrospinning using nested capillary spinnerets, often coaxial, has led to an explosion of creativity, with a diversity of functional nano- and microfibers with a variety of internal morphologies being successfully electrospun.[9−13] Pioneering contributions in demonstrating the potential of dual-phase coaxial electrospinning for making controlled core–sheath fibers were published by Sun et al.,[14] Yu et al.,[15] and Li and Xia.[16] The latter was the first paper to spin coaxial fibers where the core was a nonpolymeric and nonvolatile liquid, thus defining a cylindrical core that could easily be removed after spinning to make hollow tubes. The authors emphasized that the core and sheath liquids must be immiscible for reliable results. This contrasted with the results of Sun et al. and Yu et al., which both were obtained with miscible core and sheath liquids.

While the mineral oil used as core liquid by Li and Xia was largely a sacrificial fluid, its presence ensuring tube-like fiber morphology, several subsequent electrospinning studies incorporated more precious liquids, e.g., phase change materials,[17−19] liquid crystals (LC),[20−36] and shear thickening fluids,[37] to remain as a functional core inside the fibers. These specially selected core liquids enhance the composite fibers with dynamic and responsive performance that the sheath polymer itself is incapable of, while the coaxial fiber geometry provides a powerful means of encapsulating the liquids—which are unspinnable on their own—in a flexible form factor with high surface-to-volume ratio. Several modifications of the fundamental core–sheath electrospinning process have been explored, such as triple-phase coaxial electrospinning[a], enabled by adding a third nested capillary, which can yield fibers with an intermediate layer between the innermost core and the outermost sheath.[38−41] With noncoaxial electrospinning using multiple bundled capillaries inside an outer capillary that flows the sheath solution, fibers were produced with multiple core channels, consisting of identical[42] or different[18,27] materials.

Received: July 8, 2021
Revised: October 20, 2021
Published: November 4, 2021

https://doi.org/10.1021/acs.langmuir.1c01824
Langmuir 2021, 37, 13265–13277

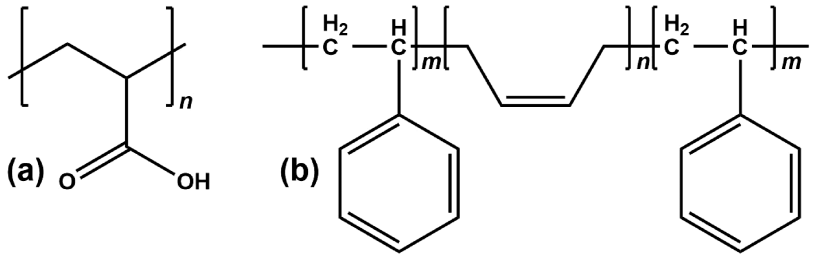

Figure 1. Chemical structures of (a) poly(acrylic acid) (PAA) and (b) polystyrene-*block*-poly-*cis*-butadiene-*block*-polystyrene (SBS).

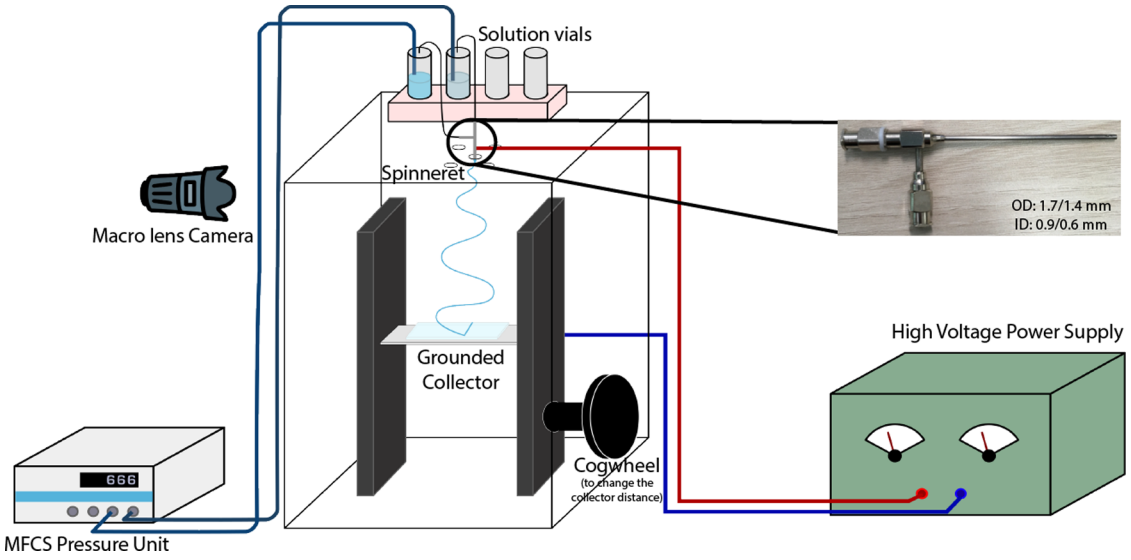

Figure 2. Schematic representation of the electrospinning setup. MFCS is the pressure control unit that controls the liquid flow. Inset: The spinneret used for the experiments.

Core−sheath fibers were also obtained using single-phase electrospinning, relying on radial phase separation during spinning.[23,28,32,35,36] Using the different variations of core−sheath fiber electrospinning, functional composite fibers have been produced for a variety of application scenarios, such as sustained release of drugs,[11,40,43−52] growth factor,[53,54] genes,[54,55] or live cells;[56−58] enhanced thermal insulation;[17−19] sensing of volatile organic compounds;[25,29,32,59] generation of wavy polymer structures;[60] or sound damping.[37]

Despite the strong interest in core−sheath electrospinning, the answer to the critical question of whether the core and sheath liquids should be miscible or not remains elusive. The original confusion remains, with different teams publishing conflicting views on the matter, both for core−sheath electrospinning and for the closely related challenge of core−sheath electrospray. Several papers reported on spinning cores and sheaths that are fully miscible,[14,15,37,41,43−46,49,53,58,61,62] some emphasizing the importance of low interfacial tension, γ_{cs}, between the two liquids.[15,63] Others have maintained that cores and sheaths should be immiscible,[16−18,30,42,55,64−66] often referring to the original Li and Xia work, which even showed evidence of loss of core−sheath structure when miscible fluids were spun.[16] In our own research, we have encountered problems with both approaches, frequently failing to produce core−sheath fibers either due to excessive γ_{cs} between immiscible liquids or due to miscible liquids without a well-defined interface fusing together, leaving no core−sheath structure in the produced fibers. Given the scarcity of publications of negative results, we believe other teams may have faced similar issues without reporting them.

The purpose of this paper is to clarify the situation by conducting a thorough and systematic investigation of core−sheath interfacial phenomena and how they are affected by (im-)miscibility between the two liquids, using a liquid crystal (LC) mixture as a model fiber-functionalizing core fluid that is nonvolatile and nonpolymeric, and three representative polymer solutions for the sheath. We focus particularly on the quality of the Taylor cone, of fundamental importance to the success of any electrospinning process, since the jet that will form the fiber emanates from the Taylor cone apex. We recently demonstrated that humidity in the spinning environment can ruin the quality and stability of the Taylor cone and that certain core fluids during coaxial electrospinning can amplify this sensitivity to humidity.[67] We now move the attention from the Taylor cone outside to the core−sheath interface, where we find that neither complete miscibility nor complete immiscibility is advisable: the former triggers sheath gelation and loss of core−sheath structure; the latter gives rise to core breakup in the jet, often already in the Taylor cone. The ideal is partial miscibility with a miscibility gap creating a distinct core−sheath interface, yet its interfacial tension γ_{cs} is much reduced since the two bounding phases contain the same constituents, only at different compositions. The low γ_{cs} allows an uninterrupted core flow from the inner spinneret needle to the Taylor cone apex, where it enters the jet that forms the fiber, and it also prevents the Rayleigh−Plateau instability from breaking up the continuous core within the jet. We also believe

https://doi.org/10.1021/acs.langmuir.1c01824
Langmuir 2021, 37, 13265−13277

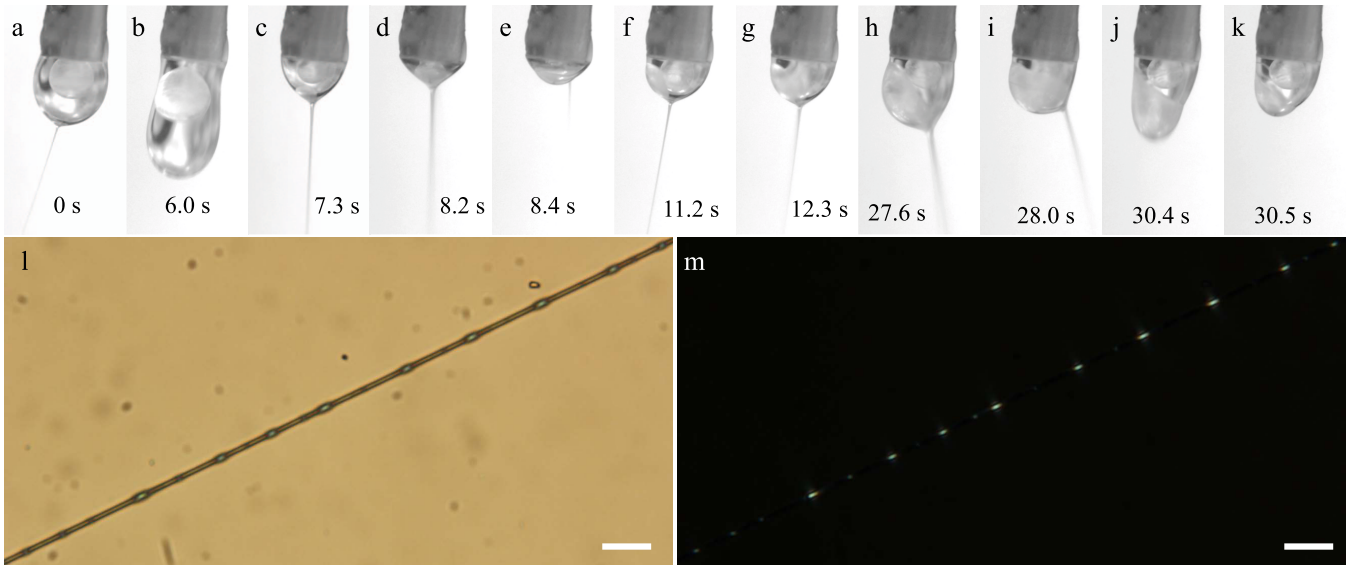

Figure 3. Top row: Taylor cone at different stages during electrospinning the LC core into an 11.5% w/w PAA-in-pure water sheath solution. The images are extracted from Supporting Information Movie S1, the time stamps relating to the start of the movie. The outer needle of the spinneret (1.7 mm diameter) appears slightly inclined at the top of every image because the camera was not oriented perfectly; in reality, the spinneret was vertically oriented. Bottom row: polarizing optical microscope (POM) images (l: without analyzer; m: between crossed polarizers) of the best-quality fiber produced during this experiment, exhibiting regularly spaced beads filled with LC. Scale bars are 20 μm.

that solutal Marangoni flow, to the best of our knowledge not previously discussed in the context of core−sheath electrospinning, can have a highly disruptive influence, and we find that the problem can be avoided by premixing a small fraction of sheath solvent into the core prior to electrospinning.

EXPERIMENTAL SECTION

Polymer Solutions and Liquid Crystals. Poly(acrylic acid) (PAA; $\overline{M_w}$ 450 kg/mol, Figure 1a), a polymer soluble in both water and ethanol, was purchased from Sigma-Aldrich and either dissolved in anhydrous ethanol (purchased from VWR) to prepare a 10% w/w solution or in ultrapure deionized water (Sartorius Arium system, resistivity 18.2 MΩ·cm) to make an 11.5% w/w PAA−water solution. Polystyrene-*block*-poly-*cis*-butadiene-*block*-polystyrene (SBS; 30% w/w styrene; $\overline{M_w}$ 140 kg/mol, Figure 1b) was also purchased from Sigma-Aldrich and dissolved in tetrahydrofuran (THF, from Sigma-Aldrich) to prepare a 10% w/w solution. For the core material, we used the multicomponent nematic liquid crystal mixture RO-TN 651 (proprietary composition), sourced from F. Hoffman-La Roche (Basel, Switzerland), on its own or mixed with 10% w/w of ethanol. We measured the surface tension of pure RO-TN 651 to be 32.33 ± 0.02 mN/m (at 20 °C); the surface tension of ethanol (at 20 °C) is 22.31 mN/m.[68] We could not measure the surface tension of the mixture of RO-TN 651 with 10% w/w ethanol because this mixture wets the needle used to make a pendant drop (even when a needle made from poly(tetrafluoroethylene), PTFE is employed). Nevertheless, we expect that the surface tension of the ethanol/RO-TN 651 mixture falls within the range of 22−32 mN/m, bounded by the values corresponding to the pure components. All materials were used as received without further purification.

Electrospinning Parameters. The dual-phase spinneret used for electrospinning, consisting of coaxially mounted stainless steel needles (external/internal diameter of the inner needle: 0.9/0.6 mm; of the outer needle: 1.7/1.4 mm), was purchased from Y-Flow. The outer needle of the spinneret has dents to keep the inner needle in the center and, at the same time, to provide an ohmic contact between the two needles that ensures they are at the same electrical potential. The spinneret was stored in ethanol when not in use and, prior to and after experiments, was thoroughly rinsed with fresh 96% w/w ethanol to remove any material residues. Before starting the electrospinning process, the spinneret was carefully dried to avoid any possible cross contamination from the lower-grade ethanol used for cleaning. This was achieved by flushing the spinneret with compressed air and storing it at 25 °C for a few hours.

Figure 2 shows a schematic representation of the electrospinning setup. It is housed inside an acrylic box, with a mobile collector wrapped in aluminum foil and the spinneret inserted with vertical needle orientation from the top. The fluids are pumped to the respective spinneret needle through tubes connected to fluid vials pressurized by a microfluidic pressure unit (Fluigent, model MFCS-EZ, maximum pressure 1034 mbar, uncertainty ± 0.3 mbar), and the electrical potential of the spinneret is controlled by connecting the outer needle to a high-voltage power supply (γ High Voltage, model ES30R-5W/DAM/RS232). The Taylor cone was imaged using a macro lens (Tokina AT-X Pro) mounted on a camera (Pixelink D755). Representative still frames were extracted from the movies and then digitally enhanced for clarity using "Adjust image" in Keynote (Apple), setting Saturation at −100%, the right-most Levels parameter to 53%, and the middle one to 40% (Figures 3, 5, and 6) or 47% (Figure 7). In Figures 3, 5, and 6, Exposure and Shadows were additionally adjusted to 100%.

Fibers were collected freely hanging on a copper wire frame and on hydrophobized glass microscopy slides to avoid wetting and collapse of the filled fibers.[27,69] These slides were prepared by cleaning 25 mm × 75 mm borosilicate glass microscopy slides (Carl Roth) with alternating rinses of isopropanol and ultrapure deionized water before surface activation with a handheld corona generator for at least 30 s. The plasma-treated slides were then immediately immersed in an aqueous solution of 2% v/v *N*,*N*-dimethyl-[*N*-octadecyl-3-aminopropyl]trimethoxysilyl chloride (DMOAP, 42% in methanol, Sigma-Aldrich) and allowed to stand for at least 15 min, with gentle shaking halfway through the soaking procedure to ensure that the solution adequately coated and functionalized the glass slides. The slides were then removed from the treatment solution, rinsed several times with deionized water, and dried under vacuum at 120 °C for at least 30 min.

Establishment of Phase Diagram between RO-TN 651 and Ethanol. Vials of volume 2 mL were half-filled with each mixture, prepared by measuring out target volumes of first LC and then ethanol using Eppendorf pipettes and weighing the sample after each addition step. To minimize evaporation of ethanol and condensation of water, the vials were closed immediately after addition of the

https://doi.org/10.1021/acs.langmuir.1c01824
Langmuir 2021, 37, 13265−13277

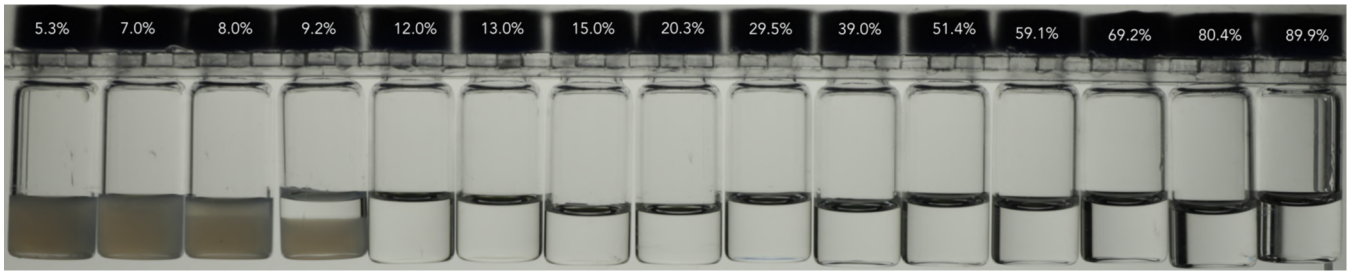

Figure 4. Sequence of vials with RO-TN 651 and gradually increasing concentration of anhydrous ethanol from left to right; the indicated percentages at the top refer to the mass fraction of ethanol. Because the nematic phase is turbid and sinks to the bottom, it is easy to recognize, although the phase separation had not completed in the 8.0% sample at the time of photography (about 20 min after the last sample preparation). We conclude the existence of a miscibility gap extending from around ∼7.5% w/w to around ∼11% w/w ethanol.

ethanol. After all samples had been prepared, each vial was shaken vigorously for about 1 min on a vortex mixer to ensure complete mixing. After this, the series of sealed vials were left to stand overnight in an air-conditioned lab with the temperature set to 21 °C, before the photograph shown in Figure 4 was captured.

Optical Characterization. Once collected, the fibers were optically characterized using a polarizing optical microscope (POM; Olympus BX-51) with a camera (Olympus DP73). POM characterization was carried out in transmission mode between crossed polarizers or with the analyzer removed.

Interfacial Tensiometry. Interfacial tension measurements were performed using a pendant drop tensiometer (Goniometer OCA 15EC from Dataphysics). The density of the solutions for interfacial tensiometry was measured using a Mettler Toledo DE45 Delta range densitometer. Both density and interfacial tension measurements were performed at room temperature.

RESULTS AND DISCUSSION

Coaxial Spinning with Aqueous PAA Sheath and LC Core: Impact of Excessive Interfacial Tension. When attempting to electrospin the LC RO-TN 651, which has negligible miscibility with water, as a core inside the PAA−water sheath solution, the relatively high γ_{cs} (measured to be 9.13 ± 0.3 mN/m at 20 °C; see Supporting Information Movie S5) causes significant problems, as seen from a detailed frame-by-frame analysis of Supporting Information Movie S1, showing the Taylor cone dynamics during a run with flow rates optimized for maximum fiber filling. Representative still frames are shown in Figure 3a−k. It is still possible to spin fibers with encapsulated LC in this way (Figure 3l−m), but we cannot get a continuous LC core and it is a very lossy process since the required overfilling of the Taylor cone with LC (to be explained below) means that the majority of the LC pumped to the spinneret never makes it into the jet.

We initially pump only the sheath solution, starting the injection of the LC core solution once a stable PAA−water Taylor cone with consistent spinning has been established. As seen at the beginning of Supporting Information Movie S1 and in Figure 3a, the LC pumped from the inner needle forms a nearly spherical droplet inside the external sheath solution, hovering far above the Taylor cone apex from which the jet is ejected. The fibers produced at this stage of the process are thus devoid of LC since no LC makes it into the jet. Because we use a high LC flow rate, the inner droplet and the overall Taylor cone continuously grow in volume and, about 2 s into the movie, the jet stops: most likely, there is too large a voltage drop from the spinneret to the bottom of the droplet at this size. Now both sheath and core droplets grow until ∼6 s into the movie, when the sheath droplet rapidly elongates before it is cleaved (Figure 3b). The cleavage process detaches the entire LC droplet from the spinneret, and most of it—but not all—leaves the Taylor cone together with the detached sheath solution.

The remainder of the LC separated from the spinneret forms a small droplet near the bottom of the Taylor cone, from which a stable jet is again ejected. The suction from the jet pulls the bottom LC droplet toward it until that in Figure 3c connects to the Taylor cone apex such that the jet is now injected with LC. In the meantime, a new top droplet of freshly injected LC has started growing from the spinneret. Once this has become large enough to touch and merge with the bottom LC droplet, we have a brief moment with a single LC volume that extends continuously from the inner spinneret needle all the way to the jet, thus yielding an ideal coaxial Taylor cone (see Figure 3d). However, this shape of the LC volume does not minimize the core−sheath interface area, and therefore the interfacial tension (γ_{cs} = 9.13 ± 0.3 mN/m; see the Supporting Information) renders this an unstable equilibrium. The continuous LC flow very quickly collapses into a geometry with a bottom LC drop again detached from the spinneret needle; see Figure 3e. At the same time, the jet moves from the bottom of the Taylor cone to the boundary between LC and sheath solution.

The lower LC droplet—which is now larger than before due to the merger with the new LC—moves to the left, detaching from the jet, which thus again contains no LC (Figure 3f). A new droplet grows from the inner spinneret needle until it merges with the lower LC droplet (Figure 3i), which thereby acquires a size large enough that it extends past the cone apex, hence now LC is again fed into the jet. This cycle of new LC droplet growing from the spinneret needle until it is large enough to merge with the LC droplet residing at the bottom of the Taylor cone, thereby separating from the spinneret and leaving an increasingly larger lower LC droplet, repeats itself another five times, the last two steps shown in Figure 3h−i. Throughout this stage, the jet is continuously fed with LC as the Taylor cone apex is fully covered by the lower LC droplet. However, since the process requires overfeeding of the Taylor cone with LC, the process makes the inner LC droplet, and thus the overall Taylor cone, increasingly heavier, and in Figure 3j, another cleavage event occurs, removing most of the LC from the Taylor cone. Again, a fraction is left at the bottom of the Taylor cone (Figure 3k) and the full cycle repeats itself.

While this trick of overfeeding the Taylor cone with LC thus leads to core injection into the jet a large fraction of the time, it comes at the cost of very significant loss of LC every time a droplet is pinched off from the Taylor cone, in addition to the problems that the macroscopic drop may cause if it lands on

https://doi.org/10.1021/acs.langmuir.1c01824
Langmuir 2021, 37, 13265−13277

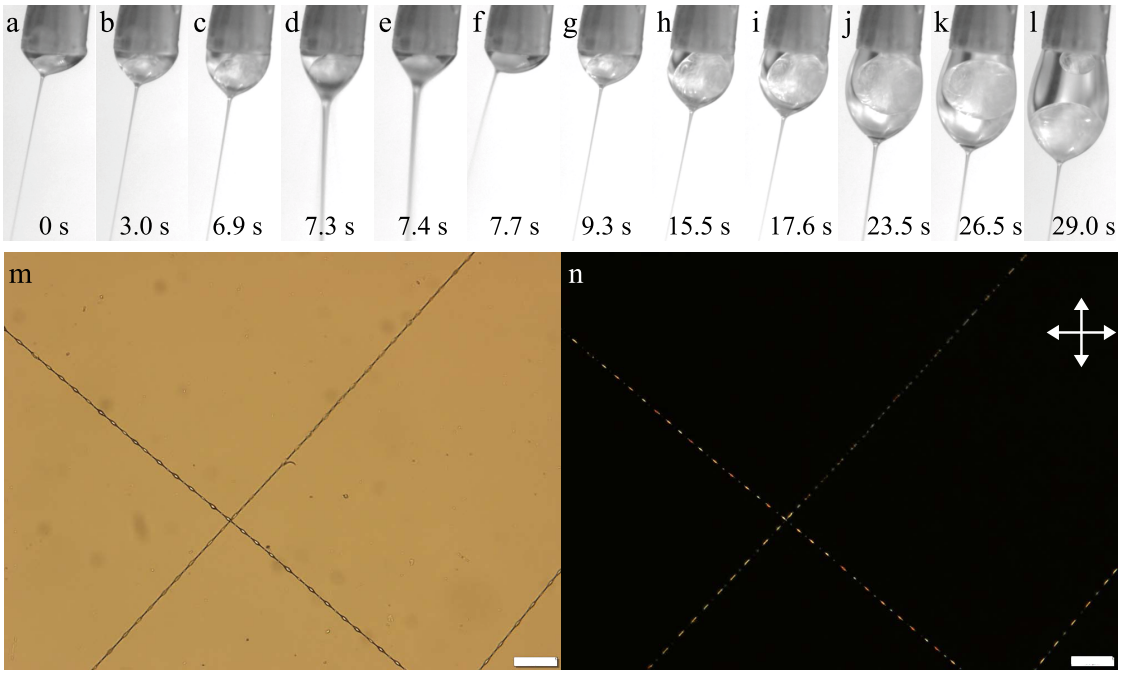

Figure 5. Top row: Taylor cone at different stages during electrospinning the LC core into a 10% w/w PAA in pure ethanol sheath solution. The images are extracted from Supporting Information Movie S2, the time stamps relating to the start of the movie. The outer needle of the spinneret (1.7 mm diameter) appears at the top of every image, slightly inclined because the camera was not oriented perfectly; in reality, the spinneret was vertically oriented. Bottom row: POM images (m: without analyzer; n: between crossed polarizers, as indicated by double-headed arrows) of the best-quality fiber produced during this experiment, exhibiting regularly spaced beads filled with LC. Scale bars are 50 μm.

the fiber mat. Note that horizontal electrospinning cannot be used in this mode, since we rely on gravity to push the detached lower LC droplet on top of the jet. Moreover, even during the period when the jet is fed with LC, the relatively high γ_{cs} continues to cause problems within the jet, triggering an internal Rayleigh–Plateau instability that breaks up the continuous core into a train of discrete LC droplets. The result is that the best fibers produced with this core–sheath combination are beaded, with discrete pockets of LC regularly spaced along the fibers; see the example in Figure 3l–m.

Replacing Water with Ethanol in the Sheath Solution. While RO-TN 651 is practically insoluble in water, the mixture is partially soluble in ethanol. Figure 4 shows that about 7.5% w/w anhydrous ethanol destabilizes the nematic phase at room temperature, and the miscibility gap between the ethanol-poor nematic phase and ethanol-rich isotropic phase extends to between 9.2 and 12.0% w/w. Although we cannot establish the mole percentages since we do not know the composition of the commercial RO-TN 651 mixture, the miscibility gap appears to be somewhat narrower than that of ethanol and the commonly used single-component LC 5CB, which at room temperature extends from ∼13 to ∼23 mol %.[70] At no point do we see two isotropic phases in coexistence in Figure 4. The partial miscibility of RO-TN 651 and ethanol, and the miscibility gap starting at low ethanol concentrations, render an experiment using PAA dissolved in ethanol as sheath and RO-TN 651 as core highly interesting. The miscibility gap ensures that a transient, yet well-defined interface exists between core and sheath, even if they start mixing, as the core is continuously replenished with fresh LC from the spinneret. At the same time, the nonzero miscibility means that the phases on both sides of the interface contain the same chemical substances, only at different concentrations. We can thus expect a much lower γ_{cs} than the ca. 9 mN/m measured for the case where water-dissolved PAA is the sheath solution. We indeed confirm this while attempting to measure the interfacial tension of a pendant RO-TN 651 drop in a bath of a PAA/ethanol solution. Although a stable RO-TN 651 drop cannot be formed at equilibrium, a drop with a well-defined fluid interface is formed while the LC phase is ejected from the needle into the polymer solution. When the LC flow is stopped, the LC drop slightly increases in size (presumably due to ethanol from the bath mixing with the LC) and the boundary between the two fluids becomes decreasingly sharp (see Figure S1, Movie S6, and the corresponding discussion).

The result can be seen in Supporting Information Movie S2, with representative still images collected in Figure 5, showing that the situation is still far from ideal. Initially (Figure 5a–c), the inner LC core can be distinguished, as being surrounded by an increasingly turbid mixed phase that grows with time from bottom to top of the Taylor cone. During this stage, the core LC appears to be disconnected from the jet, leading to its continuous increase in volume until it connects to the jet in Figure 5d. The jet suddenly broadens greatly as much of the collected LC is ejected from the Taylor cone which rapidly diminishes in size (d–f). Around 10 s into the movie (Figure 5g–h), flow patterns are clearly seen, and the LC droplet appears to disconnect from the jet. The LC is still attached to the spinneret, however, so the droplet hovers further and further above the apex of the Taylor cone as the latter continues to grow in size (i, j). The LC eventually detaches from the spinneret 26.5 s into Supporting Information Movie S2 (Figure 5k), settling at the bottom of the Taylor cone in Figure 5l, after which the jet is again fed with LC. The situation now resembles that of Figure 3, with a bottom LC droplet resting on top of the jet ejection point and a top droplet attached to the spinneret needle growing in size until the two

https://doi.org/10.1021/acs.langmuir.1c01824
Langmuir 2021, 37, 13265−13277

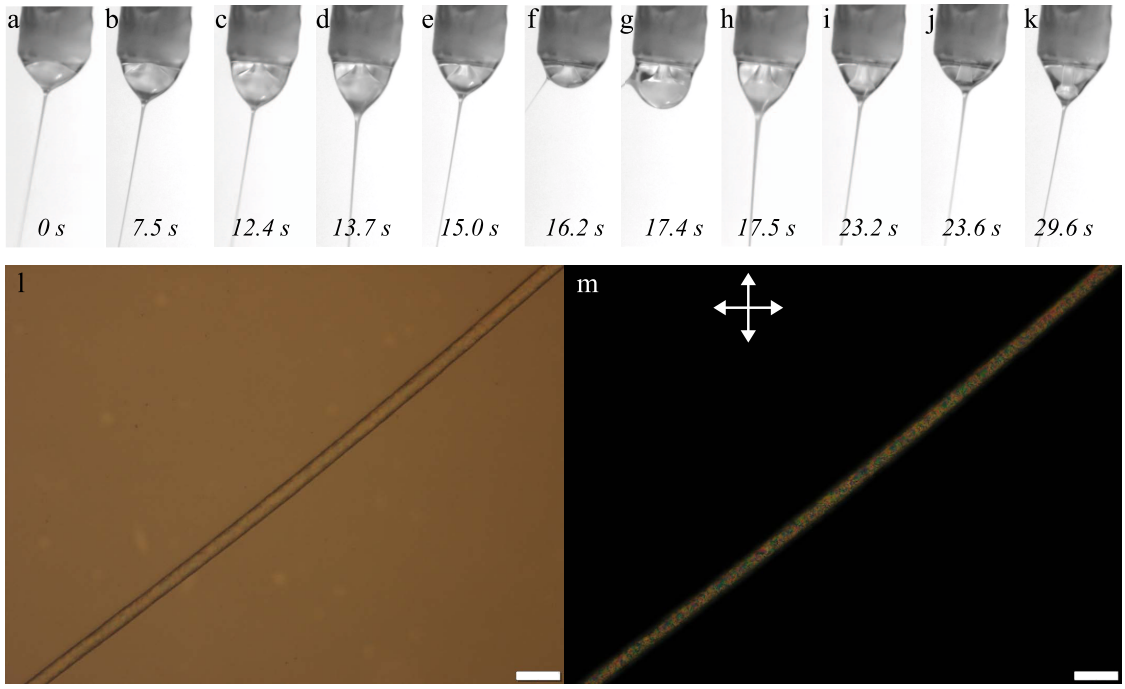

Figure 6. Top row: Taylor cone at different stages during electrospinning a core of LC with 10% w/w of ethanol added into a 10% w/w PAA in pure ethanol sheath solution. The images are extracted from Supporting Information Movie S3, the time stamps relating to the start of the movie. The outer needle of the spinneret (1.7 mm diameter) appears at the top of every image, slightly inclined because the camera was not oriented perfectly; in reality, the spinneret was vertically oriented. Bottom row: POM images (m: without analyzer; n: between crossed polarizers, as indicated by double-headed arrows) of the best-quality fiber produced during this experiment, exhibiting continuous filling of LC. Scale bars are 50 μm.

LC volumes merge and/or the Taylor cone becomes so large that it detaches from the spinneret.

We believe that the problems seen in this experiment arise because γ_{cs} is not constant within the Taylor cone: we expect a continuous gradient in γ_{cs} from the top of the spinneret, where pure LC comes in contact with pure PAA/ethanol solution, to the point further down along the core–sheath interface where enough mixing of the two liquids should have occurred to reach the miscibility gap. From this level and downward, we can expect an extremely low γ_{cs} between the coexisting nematic and isotropic phases. As a result of this spatial variation in γ_{cs} along the axis defined by the spinneret, we anticipate that the solutal Marangoni effect[71,72] sets up a new internal flow along the internal LC–polymer solution interface. Since this flow is directed from low to high γ_{cs}, it is counter-directed to the top–down flow from the spinneret (assuming that the LC droplet is in contact with both the spinneret and the apex of the Taylor cone). We thus get a circular flow pattern around the core–sheath interface, with the innermost LC moving downward while the interface is moving upward, promoting mixing and disturbing the interface, in turn causing new Marangoni stresses. This circular flow can be visualized in Supporting Information Movie S2.

In parallel, we expect to have another Marangoni effect-driven flow at the outer surface of the Taylor cone (i.e., at the air–PAA/ethanol interface). Cooling due to evaporation of ethanol leads to water condensation from the atmosphere,[67] rendering the surface tension between sheath solution and air, γ_{sa}, higher at the bottom of the air–PAA solution interface than at the top, where fresh ethanol solution without water emerges from the spinneret. This flow is from the top to the bottom (along the outer interface), thus reinforcing the natural flow within the sheath solution. In summary, we thus have the pressure-induced downward-directed flow at the very center of the Taylor cone where fresh LC is injected as core liquid; upward-directed flow at the core–sheath interface thanks to the solutal Marangoni effect; and downward-directed flow at increased speed along the Taylor cone outside, given by the sum of the pumped-out sheath solution and the thermal Marangoni effect. We can thus expect a highly complex process with multiple vortices within the Taylor cone, in combination with mixing of water into the sheath solution from the outside and a certain degree of mixing with core at the inside. Elaborate flow visualization experiments are needed to draw clear conclusions about the features of both the solutal and thermal Marangoni flows (e.g., their strength) and their interplay with the other hydrodynamic patterns inherently involved in the electrospinning process; while such experiments would be highly interesting, they are beyond the scope of this study.

The produced fibers are again beaded, with LC within the beads; see Figure 5m,n. This suggests that the mixing of ethanol from the sheath into the LC core is not fast enough to significantly reduce γ_{cs} below the level where it triggers the Rayleigh–Plateau instability within the jet prior to sheath solidification. Indeed, when preparing the experiment in Figure 4, we noticed that diffusion of LC and ethanol across the nematic–isotropic phase boundary is slow, motivating the active vortex mixing. Even if the Marangoni effects induce some active mixing in the Taylor cone, this is not enough to give the core and sheath fluids forming the compound jet so much of each other's constituents that γ_{cs} loses its impact. To reach that state, we need to adjust the core composition already prior to spinning.

https://doi.org/10.1021/acs.langmuir.1c01824
Langmuir 2021, 37, 13265–13277

Optimum Spinning Conditions by Adding Ethanol also to the Core. To reduce the impact of Marangoni flow, we add 10% w/w of ethanol to RO-TN 651 and fill this into the vial for core liquid. Note that this has brought us more than halfway into the miscibility gap; hence, we can expect a minimum γ_{cs} between the nematic phase and its coexisting isotropic phase. It also means that we have phase separation in the reservoir from which the core liquid is pumped, but we know that we are pumping only the nematic phase as core because we use pneumatic pumping rather than syringe pumps, and we place the tip of the needle taking the core liquid at the bottom of the vial. Based on the experiment in Figure 4, we can estimate the amount of ethanol in the nematic phase in the miscibility gap, which is our core liquid in this new experiment, to be about 7.5% w/w. The advantage of this approach is that γ_{cs} is significantly reduced already when the two liquids first come into contact, a slight further reduction happening on the way down from the spinneret orifice as LC diffuses out into the ethanol-PAA solution, bringing its composition closer to that of the equilibrium isotropic phase bounding the miscibility gap. A gradient in γ_{cs}, inducing Marangoni flow, thus still exists, as visible in Supporting Information Movie S3 (showing the full experiment) and in Figure 6 (summarizing the key observations), but it is not strong enough that the induced flow can disrupt the coaxial spinning. The effect could probably be canceled out completely by adding LC to the sheath solution until it has the composition of the isotropic phase in the miscibility gap, but as the LC is not a good solvent for PAA, this would cause other problems. We find that tuning the core composition to that of the miscibility gap boundary, while keeping the sheath solution free of LC, is sufficient to produce good coaxial fibers.

From an applied point of view, the single most important observation in Supporting Information Movie S3 is that the LC flow is uninterrupted throughout the entire experiment: we can easily confirm a continuous stream of LC from the inner spinneret needle orifice to the Taylor cone apex, and from there into the jet, in every frame. This is despite the fact that we exchanged the collector about halfway into the movie, causing significant temporary alterations of the electric field profile with strong shape changes of the overall Taylor cone shape. However, the experiment actually contains much more information, revealing important data on the phase separation and the interfaces present within the Taylor cone, as the following detailed analysis highlights.

When the core enters the Taylor cone, it quickly builds up a turbid volume from the bottom of the Taylor cone, filling most of it in Figure 6a. Over the next few seconds, the overall Taylor cone grows vertically downward, the lower turbid LC volume retaining a roughly constant size and moving downward, with a narrower stream of core flow connecting it to the inner spinneret needle; see Figure 6b–d. At the same time, it becomes increasingly clear that a near-horizontal boundary between two isotropic phases exists, separating the nearly pure sheath solution freshly emerged from the outer spinneret needle from the lower Taylor cone part, which has an air interface with weaker curvature just below the boundary, best seen in panel (b). We thus have two phase boundaries in the Taylor cone: a lower one between nematic and isotropic phases, rich and poor in RO-TN 651, respectively, and an upper boundary between two phases that are both isotropic. The latter type of phase separation is not present in the mixtures of RO-TN 651 and pure anhydrous ethanol, as seen in Figure 4. We conjecture that the presence of PAA in the sheath solution creates a small second miscibility gap, between the pure PAA-in-ethanol sheath solution emerging from the spinneret and the slightly LC-enriched isotropic ethanol-PAA solution that is in equilibrium with the nematic core. Another possibility is that water condensing onto the Taylor cone from the air[67] shifts the phase diagram to such an extent that an isotropic–isotropic phase separation takes place at very low LC concentration, similar to what is seen with 5CB–ethanol solutions.[70] Importantly, with RO-TN 651 as core, neither phase boundary destabilizes the spinning process, so the interfacial tension of each boundary must be very low.

The LC flow is generally clearer at the top than at the bottom, probably because of shear alignment of the director as the LC exits the spinneret, but this alignment is lost when the core flow hits the boundary to air near the Taylor cone apex, leading to strong light scattering. The boundary between the isotropic phases moves upward and is almost flush with the spinneret in panels (c)–(d), but, in panel (e), it has moved down a bit. Around this time in the experiment, we switched to a different collector, temporarily yet considerably distorting the electric field. As a result, the Taylor cone gets smaller and, in panel (f), the symmetry is broken, the jet moving to one side. The Taylor cone distortion reaches its extreme situation in panel (g). In panel (h), the new collector is in place and the jet moves down to the bottom of the Taylor cone, which is now nearly cylindrically symmetric. Over the next few seconds, the Taylor cone shrinks somewhat again, adopting a true cone shape in panel (i), where the horizontal upper phase boundary is easily distinguished. The Taylor cone fluctuates slightly in size after the collector switch, reaching its minimum size in panel (j). In panel (k), the final steady-state situation is shown, with a Taylor cone that is largely conical in shape, a distinct horizontal isotropic–isotropic boundary just below the spinneret orifice, and an LC core flow that is almost cylindrical throughout the top two-thirds of the Taylor cone, broadening only near the bottom.

Throughout the whole process, the core flow is uninterrupted, and the jet only experiences the moving-around at the height of the disturbance due to the collector change. Apart from this moment (lasting about a second), a continuous core–sheath jet is ejected from the apex of the Taylor cone. Also the produced fibers are continuously—and richly—filled with LC (Figure 6l–m), demonstrating that γ_{cs} is too low to trigger the Rayleigh–Plateau instability within the jet. Our attempts to measure γ_{cs} of this system using a pendant ethanol/RO-TN 651 drop in a PAA/ethanol bath failed: a stable drop could not be formed (see Supporting Information Movie S8 and the discussion in the Supporting Information). Nevertheless, the very low effective interfacial tension is clear from the nonminimizing behavior of the interface. Since any remaining ethanol in the core is easily evaporated after spinning, its presence during the spinning process will not affect the behavior of the LC core when the fibers are used.

Case of Complete Core–Sheath Miscibility. If one only considers the impact of γ_{cs}, the best option might appear to be to eliminate the interface entirely by choosing a core and a sheath that are fully miscible, as then a smooth concentration gradient can form all the way from pure sheath to pure core without any discontinuity. Without an interface, there is also no interfacial tension and the problems encountered so far will not arise. However, this option leads to other problems: first of all, the loss of core–sheath structure that already Li and Xia

https://doi.org/10.1021/acs.langmuir.1c01824
Langmuir 2021, 37, 13265–13277

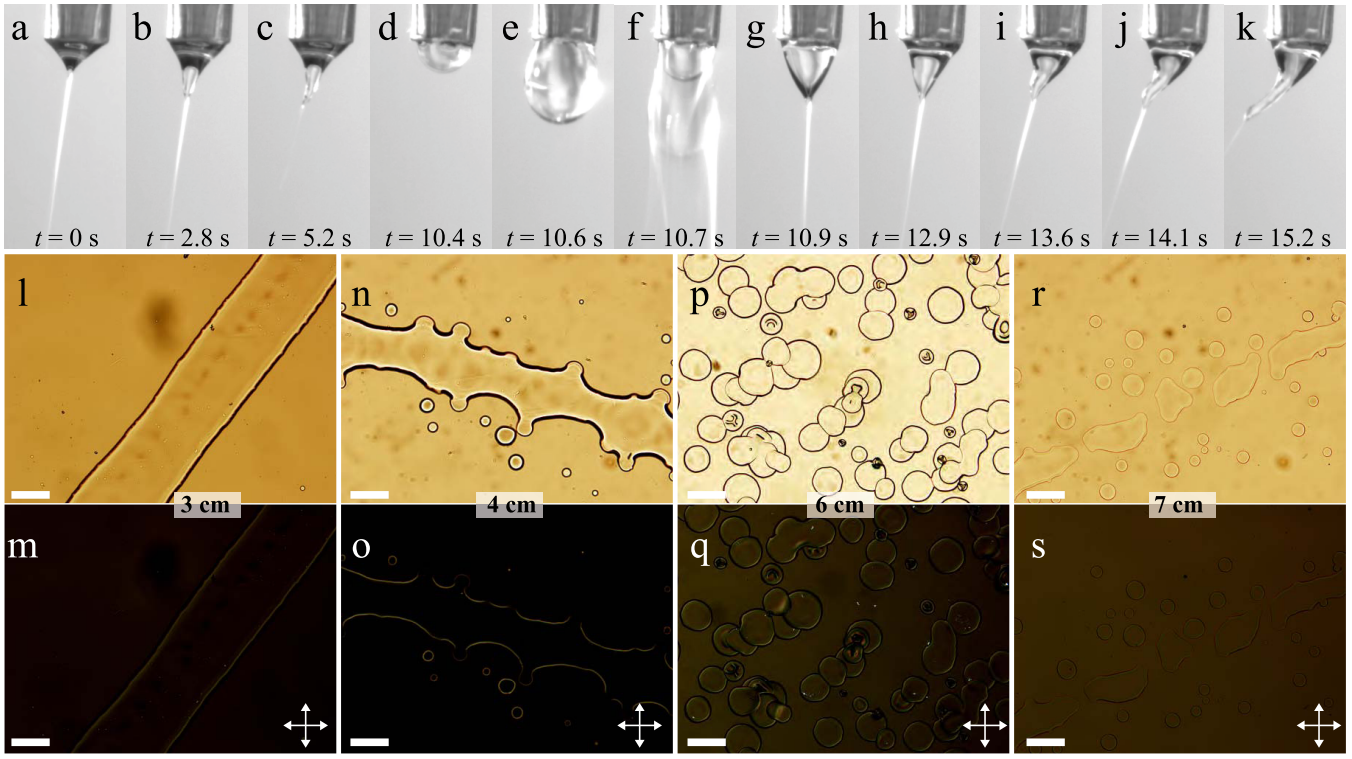

Figure 7. Top row: Taylor cone at different stages during electrospinning a core of RO-TN 651, with 10% w/w added THF, into a 10% w/w SBS in THF sheath solution. The images are extracted from Supporting Information Movie S4, the time stamps relating to the start of the movie. The outer needle of the spinneret (1.7 mm diameter) appears at the top of every image, slightly inclined because the camera was not oriented perfectly; in reality, the spinneret was vertically oriented. Bottom rows: POM images (l, n, p, r: without analyzer; m, o, q, s: between crossed polarizers, as indicated by double-headed arrows) of the spinning product collected at 3, 4, 6, and 7 cm below the spinneret, respectively. Scale bars are 10 μm.

noted in their pioneering work.[16] This is particularly critical when—as in the present work—the core is a low molar mass liquid, since then we cannot rely on the low miscibility of polymeric solutes to prevent or at least slow down core−sheath mixing. Even more critically, if core and sheath are fully miscible but the core is not a good solvent for the sheath polymer (typically the case with functional core materials like LCs), then the loss of sheath solvent into the core and core liquid moving into the sheath will rapidly deteriorate the quality of the sheath solution from the perspective of dissolving the polymer. The core effectively becomes an internal coagulation bath, as used in traditional wet spinning to rapidly solidify the polymer. If the sheath solvent is volatile, the polymer concentration in the sheath solution also rapidly decreases and/or water is condensed from the air, adding yet another nonsolvent for many polymers. The combined result is that the Taylor cone is strongly distorted and often clogged within seconds or minutes, disrupting the spinning process.

To demonstrate these problems, we choose styrene-butadiene-styrene (SBS) block copolymer dissolved in tetrahydrofuran (THF) as a relevant example of a sheath solution that is highly miscible with RO-TN 651. This sheath is interesting because several groups have successfully electrospun SBS dissolved in THF (and co-solvents) into highly stretchable elastomeric fiber mats,[73] which may then serve as a basis for stretchable electronic composites,[74] light-emitting diodes (LEDs),[75] or wearable organic vapor sensors.[76] We have ourselves tried to use SBS as a sheath for LC core-functionalized fibers (with and without addition of dimethylformamide (DMF) as a co-solvent), but without success. In the experiment shown in Supporting Information Movie S4 and Figure 7, the reasons for the failure are clearly revealed.

During the first 10 s of the experiment, only sheath solution is spun and we initially see an excellent Taylor cone in Figure 7a. However, even without any core being injected, we see that THF as the sole solvent is not ideal: some 2 s into the movie, the tip of the Taylor cone starts elongating (b), clearly demonstrating that it is no longer in a fully liquid state. The volatile THF evaporates too quickly, and probably the consequent cooling of the Taylor cone also induces condensation of water,[67] which dissolves in THF but is a nonsolvent for SBS. The result is gelation of the Taylor cone toward its apex, which, in panel (c), even gives it a clearly asymmetric distortion.

Because of the gelation, the spinneret is wiped clean (seen in Supporting Information Movie S4) and directly afterward (d) we start the injection of the LC core, easily recognized inside the Taylor cone by its turbid character. This initially stops the ejection of the jet and the compound Taylor cone grows in size (e) until the sheath breaks, without breaking off the core (f). Directly afterward, at 10.9 s into the movie (Figure 7g), a good core−sheath Taylor cone can be seen, with the core extending continuously from the spinneret orifice to the Taylor cone apex, from which a compound jet is ejected. However, already in panel (g) one can notice a horizontal boundary of the sheath just below the spinneret orifice, and in panel (h), we clearly see that the Taylor cone curvature is different above and below this boundary. This suggests that the sheath solution starts to gel below the boundary, allowing the Taylor cone to extend more vertically here than above the boundary. Importantly, this boundary was never seen prior to injecting the LC (see panels

https://doi.org/10.1021/acs.langmuir.1c01824
Langmuir 2021, 37, 13265−13277

a−c); hence, it is the core acting as coagulation bath that is causing this deterioration of the Taylor cone.

In panel (h), we can even start distinguishing a second boundary further down, which becomes very clear in panel (i). Below the second boundary, the Taylor cone loses its cylindrical symmetry and it distorts leftward in the image. The distortion increases in size over the next few seconds (j) until that in panel (k) is so strong that reliable spinning from the Taylor cone is no longer possible. We wipe the spinneret clean just after (k), but it takes less than 4 s until the Taylor cone again deforms so strongly that spinning is stopped; see Supporting Information Movie S4. Although the rapid evaporation of the volatile THF already causes problems for the single-phase spinning (this is probably why Fong and Reneker[73] and Park et al.[74] used THF−DMF solvent mixtures for spinning), we see that the situation is dramatically worsened by the introduction of the core liquid that is fully miscible, without any miscibility gap, with the sheath solvent.

The elimination of core−sheath interface in the Taylor cone indeed has the advantage that the core is drawn very well into the jet, even when the Taylor cone is as distorted as in Figure 7k. But this is of little use to us: first, because it is only a matter of seconds until spinning is stopped due to Taylor cone gelation, and, second, because the core−sheath structure is lost in the jet. This is seen in panels (l)−(s), showing samples that have been collected on glass slides at different distances below the spinneret. A slide held at only 3 cm below the spinneret shows continuous ribbons, but they are very broad as no significant jet stretching could take place and much liquid still remains in the fiber; see Figure 7l−m. Importantly, there is no trace of a core−sheath structure, and the image between crossed polarizers (m) reveals that there is no liquid crystalline behavior at any point in the ribbon.

Moving further down to 4 cm below the spinneret (n−o), the ribbon has strongly undulated edges, indicating that the Rayleigh−Plateau instability is about to break it into droplets. Indeed, several droplets surround the broad ribbon that runs across the image from left to right. As before, there is neither any sign of core−sheath structure nor of liquid crystalline behavior. At a 6 cm distance (p−q), the instability has entirely broken up the jet and we see only large droplets, and at 7 cm (r−s), we see some smaller droplets and some larger regions where nearby droplets have apparently merged with—as usual—no sign of core−sheath structure or of liquid crystalline behavior. Note that much of the volatile THF should have evaporated at this point, and, in experiments without an LC core, we have indeed frequently succeeded in spinning SBS fibers in this way. However, with an LC core, its complete miscibility with the sheath solution and its non-solid state mean that the sample remains liquid, removing any trace of fibers at this stage. While the LC is not a good solvent for SBS, it is compatible enough to act as a plasticizer.

Comparison with Earlier Studies. We end by briefly revisiting some of the previously published papers discussed in the beginning in light of the new knowledge brought about by experiments. Considering first the early papers with miscible solvents by Sun et al.[14] and Yu et al.,[15] we note that both deal with polymer solutions as cores, with the exception of one experiment by Sun et al. where the core was a THF solution of palladium(II) acetate. The entangled nature of polymer solutions and the general difficulty to mix two different polymers makes it credible that no significant mixing between core and sheath polymers takes place during the residence time in the Taylor cone when core and sheath are both polymeric. We also note that the solvents of the core and sheath solutions can be grouped into three categories: (i) identical solvents or solvent mixtures (all cases in ref 15 belong to this category), (ii) immiscible solvents (e.g., water and chloroform) but with the addition of a co-solvent that is miscible with both other solvents (in the same example ethanol in water), and (iii) different miscible solvents, but neither is a nonsolvent for any polymer (e.g., a PLA-dichloromethane sheath solution was used with the palladium acetate-THF core solution in one of the experiments of Sun et al.,[14] but PLA is soluble also in THF). Cases (i) and (iii) obviously give no relevant γ_{cs}, whereas case (ii) has γ_{cs} greatly reduced by the presence of the co-solvent soluble in both phases.

We can thus conclude that these situations all avoid phase separation and Rayleigh−Plateau instabilities by keeping γ_{cs} very low; gelation is avoided by not using any nonsolvents for the polymers used; and loss of core−sheath structure is avoided by ensuring that the time from core and sheath meeting until the fiber sheath solidifies is kept much shorter than the characteristic mixing time of core and sheath solutions. Also the fabrication of hollow tubes and rods in tubes by Zussman et al.[61] used polymeric core as well as sheath in identical solvents (DMF), but here also acetone was added as a co-solvent for the poly(methyl methacrylate) (PMMA) core solution. This is interesting since acetone is a nonsolvent for the PAN in the sheath; hence, the core acted as an internal coagulation bath, speeding up the solidification of the sheath. Obviously, some fine tuning is required to prevent this coagulation from starting prematurely in the Taylor cone; this may be why 40% DMF was included in the PMMA core solution.

In this context, a most interesting study is that by Luo and Edirisinghe of nonpolymeric core liquids, including water and glycerol, stabilizing electrospinning of polymer solutions as sheaths, when the same polymer solutions without a core only electrospray.[77] They conducted a thorough study of miscibility of the components, finding that high γ_{cs} can lead to well-defined fibers. While they also pointed out initially that a high γ_{cs} promotes the Rayleigh−Plateau instability, they drew the conclusion that the fiber formation was supported by the high γ_{cs}, although the mechanism for this was not clear. In light of our results and those of Zussman et al.,[61] we believe that the main reason for the transition from electrospray to electrospinning when using water as core liquid is that it acted as an internal coagulation bath, since the sheath solvent was miscible with water. This was not the case when using glycerol as core, but here the much greater viscosity, 3 orders of magnitude greater than that of water, is likely to be important.

The encapsulation of an industrial oil (Elf SAE-15W50) as a core inside DMF-dissolved PVP by Díaz et al.[63] and Díaz Gómez et al.,[62] as well as inside water-dissolved PEO by Díaz Gómez et al.,[62] is interesting, as Díaz et al. point out that low γ_{cs} is required,[63] yet the oil−water interface when using aqueous PEO as sheath should have quite significant γ_{cs}. However, the industrial oil actually contains surfactants;[63] hence, this is an example where surfactant addition is a viable means of reducing γ_{cs}. This approach is unfortunately not straightforward to use when working with LC cores because surfactants can strongly impact the LC alignment and even bring in emulsified water, with strong impact on the LC phase behavior.[27] Despite the low γ_{cs} (values on the order of 1 mN/m were mentioned), the produced fibers were strongly beaded,

https://doi.org/10.1021/acs.langmuir.1c01824
Langmuir 2021, 37, 13265−13277

but this may also be due to a mismatch in elongational viscosities between core and sheath.

The approach to use identical solvents in sheath and core to minimize γ_{cs} was used also by He et al.[44] (PLA in hexafluoroisopropanol, HFIP, as sheath and the drug TCH in HFIP as core), but here the nonpolymeric nature of TCH could be expected to make retained core−sheath structure more difficult. The authors used a very high electric field (4 kV/cm), kept the core flow rate low, and let the inner needle protrude beyond the end of the outer needle in the coaxial spinneret. These are all features that minimize the residence time of core and sheath in the Taylor cone, which probably was kept small by the high electric field (no information about Taylor cone was provided). While López-Rubio et al. also used the same core and sheath solvent—water—in their study of bacterial inclusions in PVA sheath fibers, this fact was not discussed explicitly.[58] However, since they obtained similar results using single-phase as with coaxial electrospinning, it is not obvious that a distinct core−sheath structure prevailed. In both cases, beaded fibers with bacteria contained in the beads were observed, but, given the size of the bacteria, this structure may have been driven by the bacterial cargo rather than by the coaxial spinning approach. Several studies with miscible or partially miscible cores and sheaths have made no detailed comments on the problems related to core−sheath stability,[30,34,37,41,43,45,46,49,53] but we note that several fall into category (ii) or (iii) above, and it is not unlikely that the particular combinations were found empirically by trial and error.

Returning to the paper by Li and Xia,[16] finally, which strongly promoted immiscible core and sheath, we note that the mineral oil used as core is actually not immiscible with the ethanol used as sheath solvent. The Food and Agriculture Organization of the United Nations states that mineral oil is "sparingly soluble in ethanol",[78] which means that this combination of core and sheath is ideal, as they are neither fully miscible nor immiscible, but have a miscibility gap, as with RO-TN 651 and ethanol studied by us here. Since the same holds for paraffin oil/wax, and also for chloroform and DMF as solvents, this explains the success of all other coaxial electrospinning papers stating a need for immiscible core and sheath,[17−19,38,42,66] inspired by the original paper by Li and Xia. We can also conclude that these studies did, in fact, not work with immiscible, but with partially miscible liquids, but the significance of this distinction was not clear at the time. Other papers that emphasize the needs for immiscible core and sheath liquids, such as the microtube electrospinning by Dror et al.[65] or the gene delivery fibers spun by Saraf et al.,[55] achieve success by using mixed solvents, giving a common or at least miscible component between core and sheath.

CONCLUSIONS

By comparing core−sheath electrospinning of a nonpolymeric and nonvolatile LC core in three different sheath solutions (one miscible, one immiscible, and one partially miscible with the LC), we have demonstrated that the optimum combination is partially miscible core and sheath liquids. When the two liquids have a miscibility gap in the phase diagram that does not reach all the way to either pure component, a distinct core−sheath interface can be maintained throughout the spinning process, yet the interfacial tension γ_{cs} can be kept very low, since both liquids contain the same chemical constituents, only at different compositions. This prevents phase separation in the Taylor cone, droplet formation due to a Rayleigh−Plateau instability in the jet, as well as loss of core−sheath structure due to complete mixing. In this way, the production of fibers with continuous core−sheath morphology can be ensured, of great value when the core adds functionality to the fiber. Importantly, the core should not be spun pure, but enough of the sheath solvent should be added to reach the miscibility gap of the phase diagram: otherwise, strong Marangoni stresses and, in turn, complex flow patterns can arise in the Taylor cone as a consequence of local variations of γ_{cs}, preventing stable core−sheath spinning. While our experiments were conducted with an LC core, these conclusions are perfectly applicable to any other core−sheath combination.

ASSOCIATED CONTENT

Supporting Information

The Supporting Information is available free of charge at https://pubs.acs.org/doi/10.1021/acs.langmuir.1c01824.

Interfacial tension characterization of the spinning solutions; snapshots of the interfacial tension measurements using the pendant drop technique of RO-TN 651 to a solution of 10% w/w PAA in anhydrous ethanol (Figure S1); electrospinning parameters and conditions (Table S1) (PDF)

Taylor cone recorded during electrospinning RO-TN 651 as core and an aqueous solution of 11.5% w/w PAA as sheath (Movie S1) (MP4)

Taylor cone recorded during electrospinning RO-TN 651 as the core and a solution of 10% w/w PAA in anhydrous ethanol as sheath (Movie S2) (MP4)

Taylor cone recorded during electrospinning of 10% w/w anhydrous ethanol in RO-TN 651 core and a solution of 10% w/w PAA in anhydrous as sheath (Movie S3) (MP4)

Taylor cone during electrospinning of 10% w/w THF in RO-TN 651 as the core and a 10% w/w SBS in THF, as sheath solution (Movie S4) (MP4)

Interfacial tension measurement using the pendant drop technique with a drop of RO-TN 651 injected at 0.5μL/s into a bath of aqueous solution of 11.5% w/w PAA (Movie S5) (MP4)

Interfacial tension measurement using the pendant drop technique with a drop of RO-TN 651 injected at 0.1μL/s into a bath of 10% w/w PAA solution in anhydrous ethanol (Movie S6) (MP4)

Interfacial tension measurement using the pendant drop technique with a drop of RO-TN 651 injected at 0.05μL/s into a bath of 10% w/w PAA solution in anhydrous ethanol (Movie S7) (MP4)

Interfacial tension measurement using the pendant drop technique with a drop of 10% w/w anhydrous ethanol in RO-TN 651 injected at 0.1μL/s into a bath of 10% w/w PAA solution in anhydrous ethanol (Movie S8) (MP4)

AUTHOR INFORMATION

Corresponding Author

Jan P. F. Lagerwall − *Experimental Soft Matter Physics Group, University of Luxembourg, L-1511 Luxembourg, Luxembourg;* orcid.org/0000-0001-9753-1147; Phone: +352 46 66 44 6219; Email: jan.lagerwall@lcsoftmatter.com; Fax: +352 46 66 44 36219

Authors

Shameek Vats − *Experimental Soft Matter Physics Group, University of Luxembourg, L-1511 Luxembourg, Luxembourg*

Manos Anyfantakis − *Experimental Soft Matter Physics Group, University of Luxembourg, L-1511 Luxembourg, Luxembourg;* orcid.org/0000-0002-4572-5641

Lawrence W. Honaker − *Experimental Soft Matter Physics Group, University of Luxembourg, L-1511 Luxembourg, Luxembourg; Laboratory of Physical Chemistry and Soft Matter, Wageningen University & Research, 6703 DE Wageningen, The Netherlands*

Francesco Basoli − *Department of Engineering, Università Campus Bio-Medico di Roma, 00128 Rome, Italy*

Complete contact information is available at: https://pubs.acs.org/10.1021/acs.langmuir.1c01824

Notes

The authors declare no competing financial interest.

■ ACKNOWLEDGMENTS

Funding for this research was provided under the European Union's H2020 Programme/ERC Grant Agreement No. 648763 (consolidator project INTERACT) and by an Aide à la formation-recherche grant (LIMEFLOW, grant number 9784104) and a CORE Junior grant (COReLIGHT, grant number C18/MS/12701231) from the Luxembourg National Research Fund. The authors thank Nicolas Tournier, Dr. Hakam Agha, and Dr. Ulrich M. Siegel for assistance in constructing the experimental setup; Anna Nauclér and Edvard Nauclér for assistance in establishing the phase diagram in Figure 4; Dr. Anupam Sengupta for allowing access to his laboratory; Dr. Vamseekrishna Ulaganathan for his assistance in performing interfacial tension measurements; and Dr. Anshul Sharma, Dr. Catherine G. Reyes, Dr. V.S.R. Jampani, and Katrin Schelski for fruitful discussions.

■ ADDITIONAL NOTE

[a]Some refer to this as "triaxial" spinning, but this is unfortunately an incorrect and even misleading terminology; both the spinnerets and the fibers are uniaxial, as indeed required by a coaxial geometry.

■ REFERENCES

(1) Formhals, A. Process and Apparatus for Preparing Artificial Threads. U.S. Patent US1975504A1934.

(2) Huang, Z.; Zhang, Y.; Kotaki, M.; Ramakrishna, S. A review on polymer nanofibers by electrospinning and their applications in nanocomposites. *Compos. Sci. Technol.* **2003**, *63*, 2223−2253.

(3) Li, D.; Xia, Y. Electrospinning of Nanofibers: Reinventing the Wheel? *Adv. Mater.* **2004**, *16*, 1151−1170.

(4) Greiner, A.; Wendorff, J. Electrospinning: A fascinating method for the preparation of ultrathin fibres. *Angew. Chem., Int. Ed.* **2007**, *46*, 5670−5703.

(5) Rutledge, G.; Fridrikh, S. Formation of fibers by electrospinning. *Adv. Drug Delivery Rev.* **2007**, *59*, 1384−1391.

(6) Reneker, D.; Yarin, A. Electrospinning jets and polymer nanofibers. *Polymer* **2008**, *49*, 2387−2425.

(7) Lu, X.; Wang, C.; Wei, Y. One-Dimensional Composite Nanomaterials: Synthesis by Electrospinning and Their Applications. *Small* **2009**, *5*, 2349−2370.

(8) Xue, J.; Wu, T.; Dai, Y.; Xia, Y. Electrospinning and Electrospun Nanofibers: Methods, Materials, and Applications. *Chem. Rev.* **2019**, *119*, 5298−5415.

(9) Yarin, A. Coaxial Electrospinning and Emulsion Electrospinning of Core-shell Fibers. *Polym. Adv. Technol.* **2011**, *22*, 310−317.

(10) Yoon, J.; Yang, H.; Lee, B.; Yu, W. Recent Progress in Coaxial Electrospinning: New Parameters, Various Structures, and Wide Applications. *Adv. Mater.* **2018**, *30*, No. e1704765.

(11) Pant, B.; Park, M.; Park, S.-J. Drug Delivery Applications of Core-Sheath Nanofibers Prepared by Coaxial Electrospinning: A Review. *Pharmaceutics* **2019**, *11*, No. 305.

(12) Han, D.; Steckl, A. J. Coaxial Electrospinning Formation of Complex Polymer Fibers and their Applications. *ChemPlusChem* **2019**, *84*, 1453−1497.

(13) Rathore, P.; Schiffman, J. Beyond the Single-Nozzle: Coaxial Electrospinning Enables Innovative Nanofiber Chemistries, Geometries, and Applications. *ACS Appl. Mater. Interfaces* **2021**, *13*, 48−66.

(14) Sun, Z.; Zussman, E.; Yarin, A.; Wendorff, J.; Greiner, A. Compound core-shell polymer nanofibers by co-electrospinning. *Adv. Mater.* **2003**, *15*, 1929−1932.

(15) Yu, J. H.; Fridrikh, S. V.; Rutledge, G. C. Production of submicrometer diameter fibers by two-fluid electrospining. *Adv. Mater.* **2004**, *16*, 1562−1566.

(16) Li, D.; Xia, Y. Direct Fabrication of Composite and Ceramic Hollow Nanofibers By Electrospinning. *Nano Lett.* **2004**, *4*, 933−938.

(17) McCann, J.; Marquez, M.; Xia, Y. Melt coaxial electrospinning: A versatile method for the encapsulation of solid materials and fabrication of phase change nanofibers. *Nano. Lett.* **2006**, *6*, 2868−2872.

(18) Wang, N.; Chen, H.; Lin, L.; Zhao, Y.; Cao, X.; Song, Y.; Jiang, L. Multicomponent Phase Change Microfibers Prepared by Temperature Control Multifluidic Electrospinning. *Macromol. Rapid Commun.* **2010**, *31*, 1622−1627.

(19) Lu, Y.; Xiao, X.; Fu, J.; Huan, C.; Qi, S.; Zhan, Y.; Zhu, Y.; Xu, G. Novel smart textile with phase change materials encapsulated core-sheath structure fabricated by coaxial electrospinning. *Chem. Eng. J.* **2019**, *355*, 532−539.

(20) Lagerwall, J. P. F.; McCann, J. T.; Formo, E.; Scalia, G.; Xia, Y. Coaxial Electrospinning of Microfibres With Liquid Crystal in the Core. *Chem. Commun.* **2008**, *42*, 5420−5422.

(21) Enz, E.; Baumeister, U.; Lagerwall, J. Coaxial Electrospinning of Liquid Crystal-containing Poly(vinyl Pyrrolidone) Microfibers. *Beilstein J. Org. Chem.* **2009**, *5*, No. 58.

(22) Enz, E.; Lagerwall, J. P. F. Electrospun microfibres with temperature sensitive iridescence from encapsulated cholesteric liquid crystal. *J. Mater. Chem.* **2010**, *20*, 6866−6872.

(23) Buyuktanir, E. A.; Frey, M. W.; West, J. L. Self-assembled, Optically Responsive Nematic Liquid Crystal/polymer Core-shell Fibers: Formation and Characterization. *Polymer* **2010**, *51*, 4823−4830.

(24) Liang, H.-L.; Enz, E.; Scalia, G.; Lagerwall, J. Liquid Crystals in Novel Geometries prepared by Microfluidics and Electrospinning. *Mol. Cryst. Liq. Cryst.* **2011**, *549*, 69−77.

(25) Kim, D. K.; Hwang, M.; Lagerwall, J. P. F. Liquid crystal-functionalization of electrospun polymer fibers. *J. Polym. Sci., Part B: Polym. Phys.* **2013**, *51*, 855−867.

(26) Scalia, G.; Enz, E.; Calò, O.; Kim, D. K.; Hwang, M.; Lee, J. H.; Lagerwall, J. P. F. Morphology and Core Continuity of Liquid-crystal-functionalized, Coaxially Electrospun Fiber Mats Tuned Via the Polymer Sheath Solution. *Macromol. Mater. Eng.* **2013**, *298*, 583−589.

(27) Kye, Y.; Kim, C.; Lagerwall, J. Multifunctional responsive fibers produced by dual liquid crystal core electrospinning. *J. Mater. Chem. C* **2015**, *3*, 8979−8985.

(28) Wang, J.; Jákli, A.; West, J. Morphology Tuning of Electrospun Liquid Crystal/Polymer Fibers. *ChemPhysChem* **2016**, *17*, 3080−3085.

(29) Reyes, C. G.; Sharma, A.; Lagerwall, J. P. Non-electronic gas sensors from electrospun mats of liquid crystal core fibers for detecting volatile organic compounds at room temperature. *Liq. Cryst.* **2016**, *43*, 1986−2001.

(30) Lin, J.; Chen, C.; Chen, L.; Chuang, Y.; Huang, S.; Lee, C.-R. Morphological appearances and photo-controllable coloration of dye-doped cholesteric liquid crystal/polymer coaxial microfibers fabricated by coaxial electrospinning technique. *Opt. Express* **2016**, *24*, 3112−3126.
(31) Bertocchi, M. J.; Ratchford, D. C.; Casalini, R.; Wynne, J. H.; Lundin, J. G. Electrospun Polymer Fibers Containing a Liquid Crystal Core: Insights into Semiflexible Confinement. *J. Phys. Chem. C* **2018**, *122*, 16964−16973.
(32) Wang, J.; Jákli, A.; West, J. L. Liquid crystal/polymer fiber mats as sensitive chemical sensors. *J. Mol. Liq.* **2018**, *267*, 490−495.
(33) Dicker, K. T.; Ratchford, D.; Casalini, R.; Thum, M. D.; Wynne, J. H.; Lundin, J. G. Surfactant Modulated Phase Transitions of Liquid Crystals Confined in Electrospun Coaxial Fibers. *Langmuir* **2020**, *36*, 7916−7924.
(34) Thum, M. D.; Ratchford, D. C.; Casalini, R.; Wynne, J. H.; Lundin, J. G. Azobenzene-Doped Liquid Crystals in Electrospun Nanofibrous Mats for Photochemical Phase Control. *ACS Appl. Nano Mater.* **2021**, *4*, 297−304.
(35) Mamuk, A. E.; Koçak, Ç.; Demirci Dönmez, ÇE. Production and characterization of liquid crystal/polyacrylonitrile nano-fibers by electrospinning method. *Colloid Polym. Sci.* **2021**, *299*, 1209−1221.
(36) Jasiurkowska-Delaporte, M.; Juszyńska-Gałązka, E.; Sas, W.; Zieliński, P. M.; Baranowska-Korczyc, A. Soft versus hard confinement effects on the phase transitions, and intra- and inter-molecular dynamics of 6BT liquid crystal constrained in electrospun polymer fibers and in nanopores. *J. Mol. Liq.* **2021**, *331*, No. 115817.
(37) Bertocchi, M. J.; Vang, P.; Balow, R. B.; Wynne, J. H.; Lundin, J. G. Enhanced Mechanical Damping in Electrospun Polymer Fibers with Liquid Cores: Applications to Sound Damping. *ACS Appl. Polym. Mater.* **2019**, *1*, 2068−2076.
(38) Chen, H.; Wang, N.; Di, J.; Zhao, Y.; Song, Y.; Jiang, L. Nanowire-in-microtube Structured Core/shell Fibers Via Multifluidic Coaxial Electrospinning. *Langmuir* **2010**, *26*, 11291−11296.
(39) Liu, W.; Ni, C.; Chase, D. B.; Rabolt, J. F. Preparation of Multilayer Biodegradable Nanofibers by Triaxial Electrospinning. *ACS Macro Lett.* **2013**, *2*, 466−468.
(40) Han, D.; Steckl, A. Triaxial electrospun nanofiber membranes for controlled dual release of functional molecules. *ACS Appl. Mater. Interfaces* **2013**, *5*, 8241−8245.
(41) Jiang, S.; Duan, G.; Zussman, E.; Greiner, A.; Agarwal, S. Highly flexible and tough concentric triaxial polystyrene fibers. *ACS Appl. Mater. Interfaces* **2014**, *6*, 5918−5923.
(42) Zhao, Y.; Cao, X.; Jiang, L. Bio-mimic Multichannel Microtubes By a Facile Method. *J. Am. Chem. Soc.* **2007**, *129*, 764−765.
(43) He, C.-L.; Huang, Z.-M.; Han, X.-J.; Liu, L.; Zhang, H.-S.; Chen, L.-S. Coaxial Electrospun Poly(L-Lactic Acid) Ultrafine Fibers for Sustained Drug Delivery. *J. Macromol. Sci., Part B* **2006**, *45*, 515−524.
(44) He, C.-L.; Huang, Z.-M.; Han, X.-J. Fabrication of drug-loaded electrospun aligned fibrous threads for suture applications. *J. Biomed. Mater. Res., Part A* **2009**, *89*, 80−95.
(45) Wang, C.; Yan, K.-W.; Lin, Y.-D.; Hsieh, P. C. H. Biodegradable Core/Shell Fibers by Coaxial Electrospinning: Processing, Fiber Characterization, and Its Application in Sustained Drug Release. *Macromolecules* **2010**, *43*, 6389−6397.
(46) Jiang, Y.; Mo, H.; Yu, D. Electrospun drug-loaded core-sheath PVP/zein nanofibers for biphasic drug release. *Int. J. Pharm.* **2012**, *438*, 232−239.
(47) Yu, D.; Yu, J.; Chen, L.; Williams, G.; Wang, X. Modified coaxial electrospinning for the preparation of high-quality ketoprofen-loaded cellulose acetate nanofibers. *Carbohydr. Polym.* **2012**, *90*, 1016−1023.
(48) Zamani, M.; Prabhakaran, M.; Ramakrishna, S. Advances in drug delivery via electrospun and electrosprayed nanomaterials. *Int. J. Nanomed.* **2013**, *8*, 2997−3017.
(49) Yu, D.; Wang, X.; Li, X.; Chian, W.; Li, Y.; Liao, Y. Electrospun biphasic drug release polyvinylpyrrolidone/ethyl cellulose core/sheath nanofibers. *Acta Biomater.* **2013**, *9*, 5665−5672.
(50) Chou, S.; Carson, D.; Woodrow, K. Current strategies for sustaining drug release from electrospun nanofibers. *J. Controlled Release* **2015**, *220*, 584−591.
(51) Wang, Q.; Yu, D.; Zhang, L.; Liu, X.; Deng, Y.; Zhao, M. Electrospun hypromellose-based hydrophilic composites for rapid dissolution of poorly water-soluble drug. *Carbohydr. Polym.* **2017**, *174*, 617−625.
(52) Khoshnevisan, K.; Maleki, H.; Samadian, H.; Shahsavari, S.; Sarrafzadeh, M.; Larijani, B.; Dorkoosh, F.; Haghpanah, V.; Khorramizadeh, M. Cellulose acetate electrospun nanofibers for drug delivery systems: Applications and recent advances. *Carbohydr. Polym.* **2018**, *198*, 131−141.
(53) Sahoo, S.; Ang, L.; Goh, J.; Toh, S. Growth factor delivery through electrospun nanofibers in scaffolds for tissue engineering applications. *J. Biomed. Mater. Res., Part A* **2010**, *93*, 1539−1550.
(54) Ji, W.; Sun, Y.; Yang, F.; van den Beucken, J.; Fan, M.; Chen, Z.; Jansen, J. Bioactive electrospun scaffolds delivering growth factors and genes for tissue engineering applications. *Pharm. Res.* **2011**, *28*, 1259−1272.
(55) Saraf, A.; Baggett, L.; Raphael, R.; Kasper, F.; Mikos, A. Regulated non-viral gene delivery from coaxial electrospun fiber mesh scaffolds. *J. Controlled Release* **2010**, *143*, 95−103.
(56) Townsend-Nicholson, A.; Jayasinghe, S. N. Cell Electrospinning: a Unique Biotechnique for Encapsulating Living Organisms for Generating Active Biological Microthreads/Scaffolds. *Biomacromolecules* **2006**, *7*, 3364−3369.
(57) Klein, S.; Kuhn, J.; Avrahami, R.; Tarre, S.; Beliavski, M.; Green, M.; Zussman, E. Encapsulation of Bacterial Cells in Electrospun Microtubes. *Biomacromolecules* **2009**, *10*, 1751−1756.
(58) López-Rubio, A.; Sanchez, E.; Sanz, Y.; Lagaron, J. Encapsulation of living bifidobacteria in ultrathin PVOH electrospun fibers. *Biomacromolecules* **2009**, *10*, 2823−2829.
(59) Pschyklenk, L.; Wagner, T.; Lorenz, A.; Kaul, P. Optical Gas Sensing with Encapsulated Chiral-Nematic Liquid Crystals. *ACS Appl. Polym. Mater.* **2020**, *2*, 1925−1932.
(60) Chiu, Y.; Weng, C.; Tseng, H.; Hsu, H.; Chen, J. Snake Tracks in Polymer Land: Wavy Polymer Structures via Selective Solvent Vapor Annealing. *Langmuir* **2020**, *36*, 9780−9785.
(61) Zussman, E.; Yarin, A.; Bazilevsky, A.; Avrahami, R.; Feldman, M. Electrospun Polyaniline/Poly(methyl methacrylate)-Derived Turbostratic Carbon Micro-/Nanotubes. *Adv. Mater.* **2006**, *18*, 348−353.
(62) Díaz Gómez, J. E.; Marín, Á. G.; Marquez, M.; Barrero, A.; Loscertales, I. G. Encapsulation and suspension of hydrophobic liquids via electro-hydrodynamics. *Biotechnol. J.* **2006**, *1*, 963−968.
(63) Díaz, J. E.; Barrero, A.; Márquez, M.; Loscertales, I. G. Controlled encapsulation of hydrophobic liquids in hydrophilic polymer nanofibers by co-electrospinning. *Adv. Funct. Mater.* **2006**, *16*, 2110−2116.
(64) Loscertales, I.; Barrero, A.; Guerrero, I.; Cortijo, R.; Marquez, M.; Ganan-Calvo, A. Micro/nano encapsulation via electrified coaxial liquid jets. *Science* **2002**, *295*, 1695−1698.
(65) Dror, Y.; Salalha, W.; Avrahami, R.; Zussman, E.; Yarin, A.; Dersch, R.; Greiner, A.; Wendorff, J. One-step production of polymeric microtubes by co-electrospinning. *Small* **2007**, *3*, 1064−1073.
(66) Chan, K.; Kotaki, M. Fabrication and morphology control of poly (methyl methacrylate) hollow structures via coaxial electrospinning. *J. Appl. Polym. Sci.* **2008**, *111*, 408−416.
(67) Reyes, C. G.; Lagerwall, J. P. F. Disruption of Electrospinning due to Water Condensation into the Taylor Cone. *ACS Appl. Mater. Interfaces* **2020**, *12*, 26566−26576.
(68) Vazquez, G.; Alvarez, E.; Navaza, J. M. Surface tension of alcohol + water from 20 to 50 °C. *J. Chem. Eng. Data* **1995**, *40*, 611−614.
(69) Kim, D. K.; Lagerwall, J. P. F. Influence of Wetting on Morphology and Core Content in Electrospun Core-Sheath Fibers. *ACS Appl. Mater. Interfaces* **2014**, *6*, 16441−16447.

https://doi.org/10.1021/acs.langmuir.1c01824
Langmuir 2021, 37, 13265−13277

(70) Reyes, C. G.; Baller, J.; Araki, T.; Lagerwall, J. P. F. Isotropic-isotropic phase separation and spinodal decomposition in liquid crystal−solvent mixtures. *Soft Matter* **2019**, 6044−6054.
(71) Scriven, L.; Sternling, C. The Marangoni effects. *Nature* **1960**, *187*, 186−188.
(72) Fanton, X.; Cazabat, A. Spreading and instabilities induced by a solutal Marangoni effect. *Langmuir* **1998**, *14*, 2554−2561.
(73) Fong, H.; Reneker, D. H. Elastomeric nanofibers of styrene−butadiene−styrene triblock copolymer. *J. Polym. Sci., Part B: Polym. Phys.* **1999**, *37*, 3488−3493.
(74) Park, M.; Im, J.; Shin, M.; Min, Y.; Park, J.; Cho, H.; Park, S.; Shim, M.; Jeon, S.; Chung, D.; Bae, J.; Park, J.; Jeong, U.; Kim, K. Highly stretchable electric circuits from a composite material of silver nanoparticles and elastomeric fibres. *Nat. Nanotechnol.* **2012**, *7*, 803−809.
(75) Lin, C.; Jiang, D.; Kuo, C.; Cho, C.; Tsai, Y.; Satoh, T.; Su, C. Water-Resistant Efficient Stretchable Perovskite-Embedded Fiber Membranes for Light-Emitting Diodes. *ACS Appl. Mater. Interfaces* **2018**, *10*, 2210−2215.
(76) Marriam, I.; Wang, X.; Mebyetekerwa, M.; Chen, G.; Zabihi, F.; Pionteck, J.; Peng, S.; Ramakrishna, S.; Yang, S.; Zhu, M. A bottom-up approach to design wearable and stretchable smart fibers with organic vapor sensing behaviors and energy storage properties. *J. Mater. Chem. A* **2018**, *6*, 3633−13643.
(77) Luo, C.; Edirisinghe, M. Core-liquid-induced transition from coaxial electrospray toelectrospinning of low-viscosity poly (lactide-co-glycolide) sheath solution. *Macromolecules* **2014**, *47*, 7930−7938.
(78) The Food and Agriculture Organization of the United Nations. Mineral Oil (Medium Viscosity). In *FAO JECFA Monographs*; FAO, 2013; Vol. *14*.

https://doi.org/10.1021/acs.langmuir.1c01824
Langmuir 2021, 37, 13265−13277

Supplementary Information for "Stable electrospinning of core-functionalized coaxial fibers enabled by the minimum-energy interface given by partial core–sheath miscibility"

Shameek Vats[a], Manos Anyfantakis[a], Lawrence W. Honaker[a,c], Francesco Basoli[b], and Jan P.F. Lagerwall[a]

[a] *Experimental Soft Matter Physics Group, University of Luxembourg, L-1511 Luxembourg, Luxembourg*

[b] *Department of Engineering, Università Campus Bio-Medico di Roma, 00128 Rome, Italy*

[c] *Laboratory of Physical Chemistry and Soft Matter, Wageningen University & Research, 6703 DE Wageningen, The Netherlands*

Discussion about interfacial tension experiments

RO-TN 651-(PAA/water) system

To measure the interfacial tension of the RO-TN 651-(PAA/water) system, we used a stainless steel needle to make a pendant drop of the LC phase inside a bath of a PAA/water solution (11.5% w/w). The experiments were performed at 20∘C. From three independent measurements (i.e., using three different drops), we measured an average value of 9.13±0.30 mN/m (the error is the standard deviation).

The SI Movie 5 shows a representative example of such a drop. Even at very large volumes (up to 35 μL; beyond this volume the drop profile exceeds the imaging window), the drop is neither strongly deformed by gravity, nor can it be detached by the needle (unless we perturb it mechanically). This is attributed to the very low density difference between RO-TN 651 (1.0469 g/cm^3) and the PAA/water solution (1.0358 g/cm^3), respectively, which minimizes the effect of gravity on the drop. After we measured the interfacial tension in the stationary drop, we performed a few cycles of first pushing the needle against the drop, and then pulling it away from the drop. It can be clearly seen in SI Movie 5 that the drop responds to these

perturbations by quickly relaxing into its equilibrium quasi-spherical shape, indicating that 9 mN/m is indeed a significant (albeit generally low) interfacial tension.

RO-TN 651-(PAA/ethanol) system

To perform interfacial tension experiments with the RO-TN 651-(PAA/ethanol) system, we used a stainless steel needle to create a pendant drop of the LC phase inside a bath of a PAA/ethanol solution (10.0% w/w). The experiments were performed at 21∘C. SI Movie 7 shows the production of LC drops inside the polymer solution bath. Even by employing a very low flow rate (0.05 μL/s), a stable drop cannot be formed. Instead, a series of small drops connected by a transient LC jet are produced. The LC jet seems to progressively dissolve in the PAA/ethanol solution, leading to individual RO-TN 651 drops that move towards the bottom of the sample cell due to gravity. Interestingly, drops that come into contact do not coalesce (within the time of the experiment), indicating some extent of stabilization, presumably by PAA chains adsorbing onto the LC-polymer solution interface. In addition, the ejected drops seem to slightly increase in size as they sediment. This suggests that swelling of the LC drop due to ethanol diffusing into its interior might take place. This is further supported by the observation that the drop-solution interface becomes less well-defined, macroscopically, as seen from the decreasing sharpness of the fluid boundary. This qualitative picture is in accordance with the phase behavior of the RO-TN 651-(PAA/ethanol) system (Fig.4) that shows that the two phases are fully miscible at very low ethanol concentrations; the pendant drop experiment described here is analogous to this case, considering that we have droplets with volumes on the order of microliters inside a bath with volume on the order of a few milliliters.

Even if we stop dosing the LC after a first drop is formed, this drop does not remain stable; the LC keeps flowing, even though there is no external pressure imposed on the syringe. The inability to make a stationary drop prevents us from measuring the equilibrium interfacial tension of the RO-TN 651-(PAA/ethanol) system. SI Movie 6 shows the early

stage of the formation of a LC drop, under the optimum conditions we identified (target drop volume 1 μL, flow rate 0.1 μL/s); higher flow rates led to a pronounced ejection of LC drops connected by a LC jet, whereas lower flow rates resulted in the case where the LC drop is not in full contact with the whole orifice of the needle. Under these experimental conditions, a well-defined drop can be formed, which is followed by the formation of a second drop that is however highly non-spherical (due to the broken jet created in its front). Fig. S1 shows snapshots from the formation of the first drop, with $t = 0$ s corresponding to the time where the first image of the shown series was recorded. Clearly, the drop shape analysis cannot give reliable interfacial tension values because the pendant drop is not stationary (pendant drop tensiometry requires a stationary drop, the shape of which is dictated by the balance of surface tension and gravity). Despite this fact, we show in Fig. S1 fits of the drop profile; as can be seen, we can fit reasonably well the shape of the pendant drop recorded in the first two images (i.e., 0 and 0.46 s), while the fitting becomes worse for longer times. Although the calculated, transient interfacial tension values (about 3 mN/m) cannot be trusted absolutely, we get an idea about their order of magnitude; they are very low. This picture of a diminishing interfacial tension between the RO-TN 651 and the PAA/ethanol phases is consistent with what would one expect for an interface formed by two phases consisting of the same chemical constituents, but at different compositions.

(RO-TN 651/ethanol)-(PAA/ethanol) system

To conduct interfacial tension experiments with the (RO-TN 651/ethanol)-(PAA/ethanol) system, we used a stainless steel needle to make a pendant drop of the ethanol-containing LC phase inside a bath of a PAA/ethanol solution (10.0% w/w). The experiments were performed at 21∘C. A few problems that prevent the formation of a well-defined, stable pendant drop of LC are shown in SI Movie 8. First, as the LC phase is pushed through the needle, a soft, solid-like phase of irregular shape emerges first. We believe this is highly concentrated (and perhaps gelled) PAA/ethanol solution that was previously left at the

opening of the needle. This can be due to drying of a portion of this solution that was left at the tip of the needle while it is removed from the solution bath in order to be cleaned. Without this cleaning cycle, we are not able to form a pendant drop at all. Furthermore, as more LC is flushed through the needle, an irregularly shaped LC drop emerges which surrounds the solid-like polymer solution phase. At longer times, and with more LC emerging from the orifice, more drops are formed that are initially separated from the first LC drop before they eventually merge to form a large, irregularly-shaped LC drop. The difficulty in merging, in conjunction with the irregular shape of the LC-polymer solution interface (which is nevertheless well-defined), suggests that the LC phase is stabilized by the polymer solution, presumably by PAA chains adsorbing onto the fluid interface. While interesting, these observations clearly show that pendant drop tensiometry is not an appropriate method to measure the interfacial tension of this highly complex system.

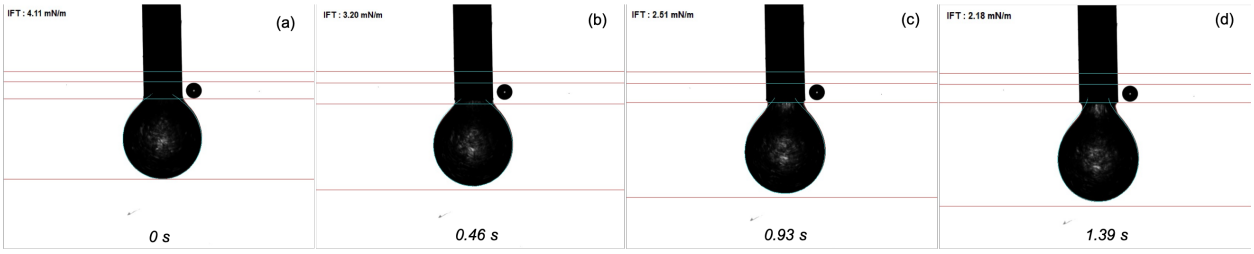

Figure S1: Snapshots of the interfacial tension measurements using pendant drop technique of ROTN 651 to a solution of 10% w/w PAA in anhydrous ethanol. These still frames are extracted from SI movie 6, the outer diameter of the stainless steel needle used for the measurements is 0.51 mm.

Electrospinning Parameters

Table S1 gives the electrospinning parameters used in the experiments.

Table S1: Electrospinning parameters and conditions.

		Relative Humidity(%)	Temperature (∘ C)	Distance (cm)	Voltage (kV)	Flow rate (ml/h)	
Sheath	Core					Sheath	Core
11.5% w/w PAA in water	RO-TN 651	25	22.6	15	9.8	5.1	0.24
10% w/w PAA in anhydrous ethanol	RO-TN 651	24	22.1	15	6.9	19.68	0.24
10% w/w PAA in anhydrous ethanol	10% w/w anhydrous ethanol in RO-TN 651	36	22.6	15	5.4	15.3	0.42

SI Videos

SI Movie 1: Movie of the Taylor cone recorded during electrospinning RO-TN 651 as core and an aqueous solution of 11.5% w/w PAA as sheath. The outer diameter of the spinneret needle is 1.7 mm and the electrospinning parameters and conditions are listed in the Table S1. This movie corresponds to Figure 3.

SI Movie 2: Movie of the Taylor cone recorded during electrospinning RO-TN 651 as the core and a solution of 10% w/w PAA in anhydrous ethanol as sheath. The outer diameter of the spinneret needle is 1.7 mm and the electrospinning parameters and conditions are listed in the Table S1. This movie corresponds to Figure5.

SI Movie 3: Movie of the Taylor cone recorded during electrospinning of 10% w/w anhydrous ethanol in RO-TN 651 core and a solution of 10% w/w PAA in anhydrous as sheath. The outer diameter of the spinneret needle is 1.7 mm and the electrospinning parameters and conditions are listed in the Table S1. This movie corresponds to Figure 6.

SI Movie 4: Movie of the Taylor cone during electrospinning of 10% w/w THF in RO-TN 651 as the core and a 10% w/w SBS in THF, as sheath solution. The outer diameter of the spinneret needle is 1.7 mm. This movie corresponds to the Figure 7.

SI Movie 5: Interfacial tension measurement using pendant drop technique with a drop of RO-TN 651 immersed in a bath of aqueous solution of 11.5%w/w PAA. The flow rate of the pendant drop is 0.5 μL/s and the diameter of the stainless steel needle used is 0.51 mm.

SI Movie 6: Interfacial tension measurement using pendant drop technique with a drop of RO-TN 651 immersed in a bath of 10%w/w PAA solution in anhydrous ethanol. The flow rate of the pendant drop is 0.1 μL/s and the diameter of the stainless steel needle used is 0.51 mm.

SI Movie 7: Interfacial tension measurement using pendant drop technique with a drop of RO-TN 651 immersed in a bath of 10%w/w PAA solution in anhydrous ethanol. The flow rate of the pendant drop is 0.05 μL/s and the diameter of the stainless steel needle used is 0.51 mm.

SI Movie 8: Interfacial tension measurement using pendant drop technique with a drop of 10% w/w anhydrous ethanol in RO-TN 651 immersed in a bath of 10%w/w PAA solution in anhydrous ethanol. The flow rate of the pendant drop is 0.1 μL/s and the diameter of the Teflon needle used is 0.8 mm.

2

Macromolecular Materials and Engineering
www.mame-journal.de

Electrospinning Ethanol–Water Solutions of Poly(Acrylic Acid): Nonlinear Viscosity Variations and Dynamic Taylor Cone Behavior

*Shameek Vats, Lawrence W. Honaker, Margaret W. Frey, Francesco Basoli, and Jan P.F. Lagerwall**

Electrospinning of polymer solutions is a multifaceted process that depends on the careful balancing of many parameters to achieve a desired outcome, in many cases including mixtures of multiple solvents. A systematic study of how the solution viscosity η—a good probe of solvent–polymer interactions—and the electrospinnability change when poly(acrylic acid) (PAA) is dissolved in ethanol–water mixtures at varying mixing ratio is carried out. A pronounced maximum is found in η at a water-to-ethanol molar ratio of about 2:1, where the solvent mixture deviates maximally from ideal mixing behavior and partial deprotonation of carboxyl groups by water coincides synergistically with dissolution of the uncharged protonated PAA fraction by ethanol. The PAA concentration is tuned as a function of water–ethanol ratio to obtain a common value of η for all solvent mixtures that is suitable for electrospinning. For high PAA content, the Taylor cone grows in volume over time despite minimum solution flow rate, even experiencing surface gelation for ethanol-rich solutions. This is attributed to the hygroscopic nature of PAA, drawing excess water into the Taylor cone from the air during spinning.

1. Introduction

Benefiting from its versatility, small equipment footprint, and ease in combining multiple materials within one and the same fiber, electrospinning[1–5] has become a popular technique for producing nonwoven mats of responsive and functionalized polymer fibers with very high specific surface area.[6,7] The diversity of properties is greatly expanded by incorporating functional liquids that are not spinnable on their own to make multifunctional composite fibers,[8–18] using coaxial electrospinning[19–22] or in situ phase separation.[23–25] Exhibiting manifold properties and significant tunability, these fibers are attractive to apply across many areas, for example, in sensing,[12,15,26–29] sound damping,[30] dynamic patterning,[31] thermal insulation via phase-change materials,[32,33] self-healing coatings,[34] or drug release.[35–39] However, success in spinning multifunctional composite fibers requires careful optimization of the polymer solvent with respect to the functional additive: otherwise, phenomena such as phase separation and gelation can disrupt the electrospinning process.[6,40] A common strategy (also in single-phase spinning) is to use mixtures of solvents, but many papers report only a fix solvent composition, without including any systematic study of how the polymer solution properties change with solvent mixing ratio. Given that a change in solvent composition can strongly affect the polymer–solvent interactions, there is good reason to carry out such a systematic study.

In this context, poly(acrylic acid) (PAA, **Figure 1**) is interesting, as it is readily soluble in water as well as ethanol,[41,42] allowing a complete study of how mixing these two solvents affects the PAA solution and its electrospinnability. Moreover, PAA is available in high molar mass suitable for electrospinning (as confirmed by several groups reporting successful PAA nano-/microfiber production[43–45]) and it can be made insoluble after spinning via chemical crosslinking,[43,44] of value for making fiber mats that withstand liquid immersion. The system of PAA dissolved in a water–alcohol mixture is also highly illustrative of the complexities that can arise with polymers dissolved in mixed solvents.

S. Vats, L. W. Honaker, J. P. Lagerwall
Department of Physics & Materials Science
University of Luxembourg
Luxembourg City 1511, Grand Duchy of Luxembourg
E-mail: jan.lagerwall@uni.lu

L. W. Honaker
Laboratory of Physical Chemistry and Soft Matter
Wageningen University & Research
Wageningen 6703 DE, The Netherlands

M. W. Frey
College of Human Ecology
Cornell University
Ithaca, NY 14853, USA

F. Basoli
Department of Engineering
Università Campus Bio-Medico di Roma
Rome 00128, Italy

The ORCID identification number(s) for the author(s) of this article can be found under https://doi.org/10.1002/mame.202100640

DOI: 10.1002/mame.202100640

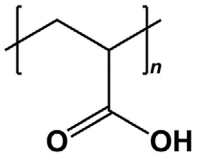

Figure 1. The structure of poly(acrylic acid) (PAA).

Studying water–ethanol solutions of polyvinylpyrrolidone (PVP), Guettari et al.[46] found that pure ethanol is a good solvent and water is a theta solvent (at the border between good and bad), while mixing reduced the performance in both directions, leading to a maximally poor solvent at about 70 mol% water. The same phenomenon was seen with water–methanol solutions of polyethylene oxide (PEO) by Shankar et al.,[47] who also demonstrated that the minimum of solvent quality coincides with a minimum of viscosity of the polymer solution. Both articles attributed the behavior to the solvent mixtures exhibiting a maximum deviation from ideal mixing behavior at a 2:1 molar ratio of water to alcohol due to competitive hydrogen bonding and formation of clusters with different solvent compositions at the molecular scale. In contrast to PVP and PEO, PAA is a polyion, that is, its pendant groups (carboxyl) are ionizable, and this can yield an even stronger sensitivity to the solvent properties. The high dielectric permittivity $\varepsilon_w \approx 78$ of water generally leaves polyions largely ionized,[48] giving rise to polyelectrolyte behavior.[49] Ethanol has a much lower permittivity than water, $\varepsilon_e \approx 25$, and we can thus expect significant counterion condensation and largely neutral PAA if it is dissolved in ethanol.

An interesting interplay between multiple phenomena should thus take place when electrospinning PAA dissolved in water–ethanol mixtures of varying compositions, because of the combined effects of a solvent changing character in a nonlinear way and the change from polyelectrolyte to neutral behavior of the solute. As a primary probe of solvent quality, we measure the shear viscosity η at low shear rate as a function of ethanol–water mixing ratio, confirming highly nonlinear behavior. To our surprise, however, PAA behaves opposite to PVP and PEO, with a maximum in η at intermediate solvent composition. This indicates that the mixed solvent has optimum properties for dissolving PAA, a finding that we attribute to the polyelectrolyte character of PAA when water is present in the solvent. We attempt to identify a PAA concentration c_{PAA} for each solvent composition that yields a value of η appropriate for electrospinning. The resulting variation in PAA concentration reveals the impact of yet another characteristic of PAA: its highly hygroscopic nature leads to significant water condensation from the air at high c_{PAA}, changing the ethanol–water balance in the Taylor cone, with strong impact on electrospinnability.

2. Results

2.1. Viscosity of PAA Solutions

The molar mass of our PAA is the same as that used by Li and Hsieh, who measured η as a function of c_{PAA} in pure water.[43] Replotting their data on a log–log scale (Figure S2, Supporting Information), a change of slope is easily recognized when c_{PAA} increases from 5% to 6% w/w. Fitting a power law function to the data, we find that the $\eta(c_{PAA})$ data are well reproduced with an exponent of 2 for c_{PAA} in the range 2–5% w/w, while, in the range 6–10% w/w, the exponent is 4.1. These exponents are well in line with the expectations for semidilute unentangled to semidilute entangled behavior, respectively[50]; hence we take c^e, $w_{PAA} \approx 5.5\%$ w/w as the critical entanglement concentration for PAA in water. This leads us to conduct our experiments with $c_{PAA} \geq 6\%$ w/w in order to have entangled solutions suitable for electrospinning.

We prepare solutions with $c_{PAA} = 6\%$, 7% , 8% , and 9% w/w in water–ethanol mixtures at 0% , 25% , 50% , 75%, and 100% w/w water, respectively, and measure η in a plate–plate rheometer as a function of oscillatory shear rate $\dot{\gamma}$. The full data are shown in the Supporting Information, Figures S3–S8, Supporting Information. Based on these data, we consider $\eta(\dot{\gamma} = 2.34\ s^{-1})$ a representative low-shear viscosity; lower $\dot{\gamma}$ gives poor measuring accuracy, possibly related to uncontrolled solvent evaporation during the long measuring time, with fluctuations in the apparent η. To get an overview of the behavior as function of water–ethanol molar ratio x_w ($x_w = 0$ corresponding to pure ethanol) as well as of c_{PAA}, we plot $\eta(\dot{\gamma} = 2.34\ s^{-1})$ as a function of x_w in **Figure 2** for $c_{PAA} = 6$, 7, and 9% w/w, respectively (see Supporting Information concerning the 8% w/w data). As an attempt to extrapolate between the experimental data points, we fitted a single-peak Gaussian function to each data set, yielding a good match to the obtained data.

The striking conclusion from Figure 2 is that all systems show a clear maximum in η for $x_w \approx 0.65$. While we thus can reproduce the findings of Guettari et al.[46] and Shankar et al.[47] in terms of extreme behavior at a water–alcohol mole ratio of 2:1, corresponding to maximally nonideal behavior of the solvent, we see the opposite extreme of maximum viscosity, suggesting maximum coil expansion and thus a maximally good solvent at this mixing ratio. We will return to the interpretation of this difference in the Discussion.

Given the strong variation in viscosity with water–ethanol ratio, it is clear that a c_{PAA} value suitable for electrospinning with one solvent composition may no longer be adequate if the water–ethanol ratio changes. We hypothesize that it will be possible to spin fibers with consistent quality across the full water–ethanol mixture window if we identify values of c_{PAA} for each solvent composition that yield a common viscosity η_0, which is tuned to be appropriate for electrospinning. We identify η_0 empirically by conducting preliminary electrospinning experiments using a solvent with water–ethanol ratio of 50:50 (by mass) and varying c_{PAA}. The best results (fibers with uniform diameter and few beads) are obtained with 7% w/w PAA, corresponding to $\eta \approx 700 - 800$ mPa·s at $\dot{\gamma} = 2.34\ s^{-1}$. For the other solvent compositions, we thus interpolate each relevant $\eta(\dot{\gamma})$ data set corresponding to Figures S3–S7, Supporting Information using an exponential fit to identify c_{PAA} that will yield $\eta_0 \approx 700$–800 mPa·s at $\dot{\gamma} = 2.34\ s^{-1}$. **Table 1** lists the compositions of the resulting PAA solutions prepared for electrospinning and Figure S9, Supporting Information shows the corresponding $\eta(\dot{\gamma})$ curves. The data for PAA in pure ethanol and in pure water, respectively, almost overlap at values slightly higher than η_0, while the data obtained with mixed solvents show some variations within the range 600–950 mPa s.

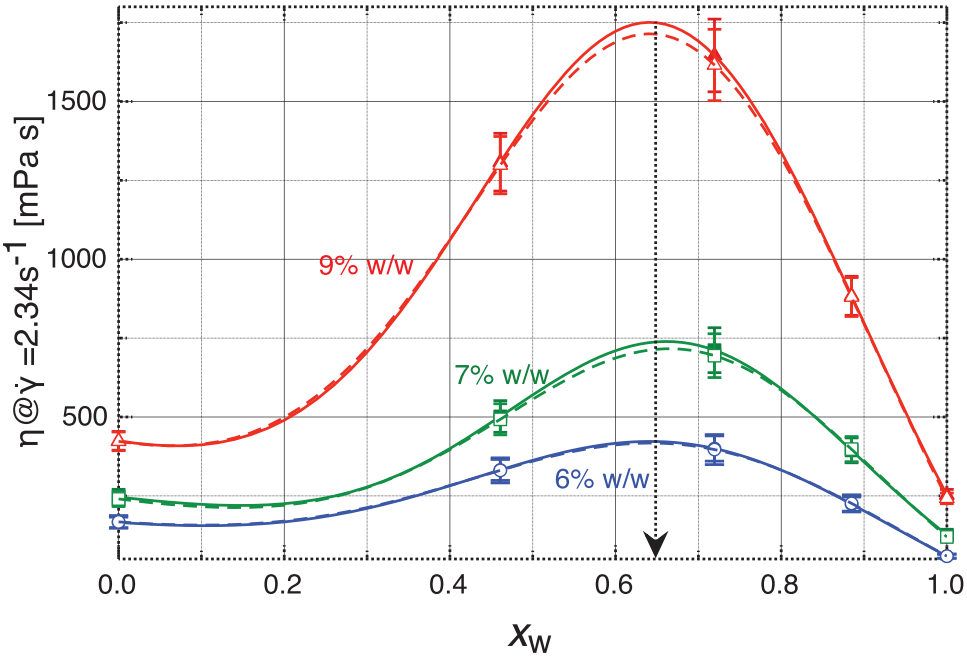

Figure 2. Low-shear rate ($\dot{\gamma}$=2.34 s^{-1}) viscosity η as a function of mole fraction of water in the ethanol–water solvent used for dissolving PAA at mass concentrations 6% , 7% , and 9% w/w, respectively. Filled symbols and continuous curves correspond to η obtained during a scan with increasing $\dot{\gamma}$, whereas empty symbols and dashed curves correspond to measurements upon decreasing $\dot{\gamma}$. The arrow highlights the solvent composition with $n_w \approx 0.65$ which appears to exhibit optimum solvent properties for PAA. The error bars are a standard deviation obtained from 4 different measurements each with increasing and decreasing shear rate.

Table 1. Concentrations (by mass) c_{PAA} of viscosity-matched solutions with different mole fractions x_w of water (or mass fractions c_w), both referring to the mixture without PAA, tailored for comparable electrospinning conditions regardless of solvent composition.

Solution	c_{PAA} [% w/w]	x_w	c_w [% w/w]
1	10	0	0
2	7.5	0.46	25
3	7	0.72	50
4	8.5	0.88	75
5	11.5	1	100

Table 2. The mean cross section diameter $\bar{d}$ with standard deviation, as obtained by measuring 100 individual cross sections in SEM images, of fibers produced from each density matched solution (compositions in Table 1), at relative humidity RH, temperature T, spinneret–collector distance L, spinning voltage V, and flow rate Q.

Solution	$\bar{d}$ [μm]	RH [%]	T [°C]	L [cm]	V [kV]	Q [mL h^{-1}]
1	2.30±0.24	29	25.1	14	7.5	0.61
2	1.30±0.13	30	24.8	14	7.5	0.65
3	1.70±0.12	30	24.5	14	7.5	0.43
4	0.67±0.06	35	26.3	14	7.5	0.23
5	1.08±0.15	35	25.9	14	7.5	0.37

2.2. Taylor Cones and Electrospun Fibers

After identifying the target viscosity η_0 and preparing PAA solutions using pure water, pure ethanol, and the three solvent mixtures, respectively, adjusting c_{PAA} to ensure $\eta \approx \eta_0$, (Table 1), we carried out electrospinning experiments to assess the suitability of each solution. The parameters for each spinning experiment are summarized in **Table 2**. During electrospinning, we paid particular attention to the Taylor cone appearance as a function of time, filming it for at least 30 s (Movies S1–S5, Supporting Information), and measuring the time that fibers are produced without the operator needing to clean the spinneret (we call this duration a "spinning cycle"). Snapshots from the beginning and end of a cycle, respectively, are shown in **Figure 3**.

Looking at the top row in Figure 3, we see that a nearideal Taylor cone develops quickly at the start of a cycle for every solution, and a stable single-jet ejection can easily be recognized in the photos. The situation is very different toward the end of a cycle, where only Solution 4 leads to a maintained stable Taylor cone and continued spinning. Although the Taylor cone in (*d'*) has grown in volume compared to (*d*), an overall stable spinning situation is seen here. For the high-ethanol content solutions 1 and 2, an unnatural distortion and elongation of the Taylor cone can be recognized, suggesting that gelation is taking place on the Taylor cone surface. Indeed, this distortion is the reason why the spinneret has to be wiped clean, ending the cycle. The distortion is present also in the Taylor cone with Solution 3, although it is not as apparent, and again this is the reason for terminating the cycle by wiping the spinneret clean.

Solution 5, where pure water is used as solvent, is different. Additionally, in this experiment, the cycle is relatively short (18 s).

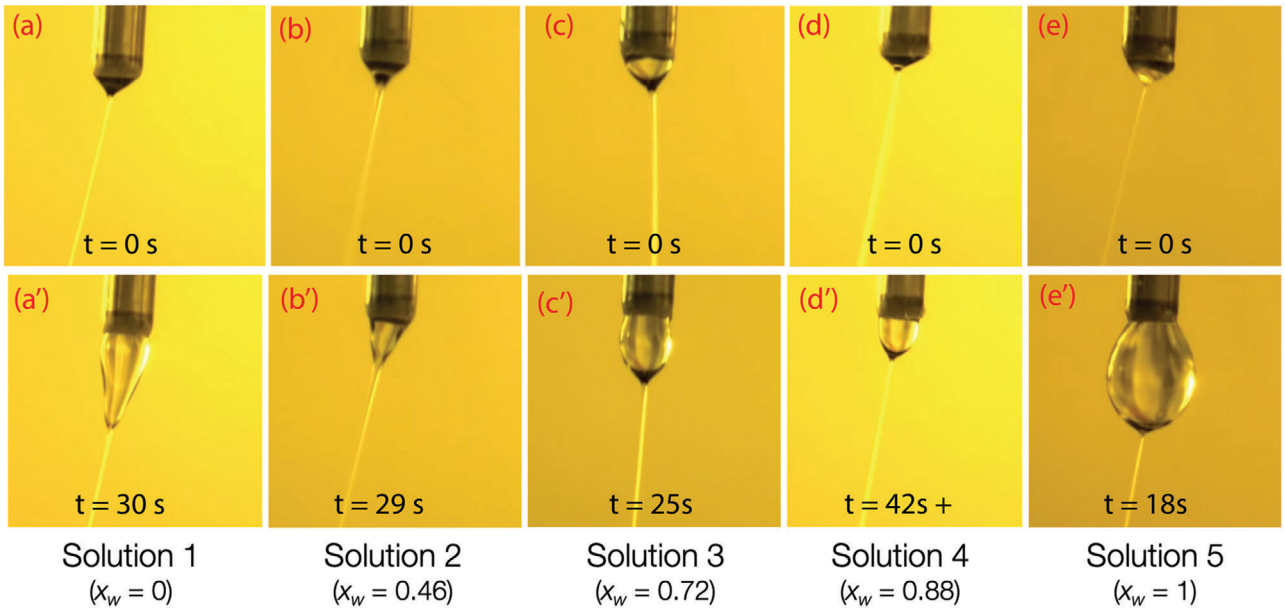

Figure 3. Taylor cone pictures of different PAA solutions (compositions in Table 1), imaged at the beginning (top row) and end (bottom row) of a spinning cycle. The spinneret was wiped clean at the end of each cycle, just after the timestamp label in the lower row, in order to restart the cycle, except for column *d*/*d*′, where spinning could continue well beyond the 42 s during which the Taylor cone was filmed (hence the t = 42 s + label in *d*′)

The reason why the spinneret has to be wiped at this point is not gelation, but rather a rapid growth of the Taylor cone to a volume where it is about to detach as a droplet. If it is not wiped off, it will land on the fiber mat and ruin the previously spun fibers. We will later return to the origin of gelation of the ethanol-rich Taylor cones and of the dramatic volume expansion of the pure-water-based Taylor cone (despite having the second lowest flow rate in the entire study, see Table 2) in the Discussion.

Our hypothesis that solutions optimized for $\eta = \eta_0$ will produce good fibers regardless of solvent composition is supported by the fact that all five solutions give smooth fibers that are free of beads, as shown in the scanning electron microscope (SEM) characterization images in **Figure 4**. However, there is a non-negligible variation of the average diameter $\bar{d}$ of the fiber cross section, spanning the range 0.6–2.3 μm. As can be seen in the histograms on the right in Figure 4 and Table 2, this variation shows a systematic correlation neither with the solvent composition x_w nor with the PAA concentration c_{PAA}. The thickest fibers are obtained with Solution 1, with a medium PAA concentration of c_{PAA} = 10% w/w at one end of the solvent composition scale, at $x_w = 0$, but the thinnest fibers are not obtained at the opposite end, but at $x_w = 0.88$. The fibers at $x_w = 1$, corresponding to the maximum PAA content c_{PAA} = 11.5% w/w, are among the thinner in the study, contrasting significantly to those obtained with $x_w = 0$ although these two solutions showed almost identical η in Figure S9, Supporting Information. The flow rate Q has significant impact, the thinnest fibers being spun with the lowest flow rate (Table 2), but there are inconsistencies also here. For instance, the greatest flow rate (Q = 0.65 mL h^{-1}) was used for Solution 2, but this produced significantly less thick fibers than Solution 1 pumped at Q = 0.61 mL h^{-1}. We will attempt to resolve these surprising and apparent inconsistencies in the following section.

3. Discussion

We first address the maximum in PAA solution viscosity at intermediate water–ethanol mixing ratios, and the maximally expanded coil size that can be assumed from this behavior. The mixing of ethanol and water is a classic example of non-ideal mixing behavior,[51–53] with a maximally negative excess volume at a water mole fraction that is often located at $x_w \approx 0.6$,[53,54] although Belda et al. report a higher value of $x_w = 0.75$.[55] This behavior is attributed to the clathrate caging of ethanol molecules by surrounding water molecules in order to maximize the number of hydrogen bonds of the latter, maximizing the enthalpy of mixing at the cost of reduced entropy, as the caging reduces the configuration space for hydrogen bonding of the water molecules.[56] The maximum deviation from ideal mixing behavior can also be seen in a maximum of viscosity of ethanol–water mixtures at $x_w \approx 0.7$.[57] However, this viscosity maximum is three orders of magnitude lower than that of the PAA solutions studied here; the impact of the viscosity of the solvent itself is thus negligible in the context of our study.

We note that the most common value $x_w \approx 0.6$[54] for maximum non-ideal water–ethanol mixing coincides rather well with $x_w \approx 0.65$ for maximum PAA solution viscosity seen in Figure 2, as well as with the minimum of solvent quality for PVP in ethanol–water mixtures studied by Guettari et al.[46] Based on dielectric spectroscopy data, Sato et al. concluded that a first critical mole fraction is $x_w = 0.82$, at which the excess activation free energy €G^E is at a maximum, corresponding to maximum ethanol–water interactions.[52] They argue that, for lower x_w, ethanol molecules form clusters, thus with microphase segregation taking place between water and ethanol. They found a second critical mole fraction of $x_w = 0.58$, near the region where most studies find the maximum negative excess volume,[54] which they

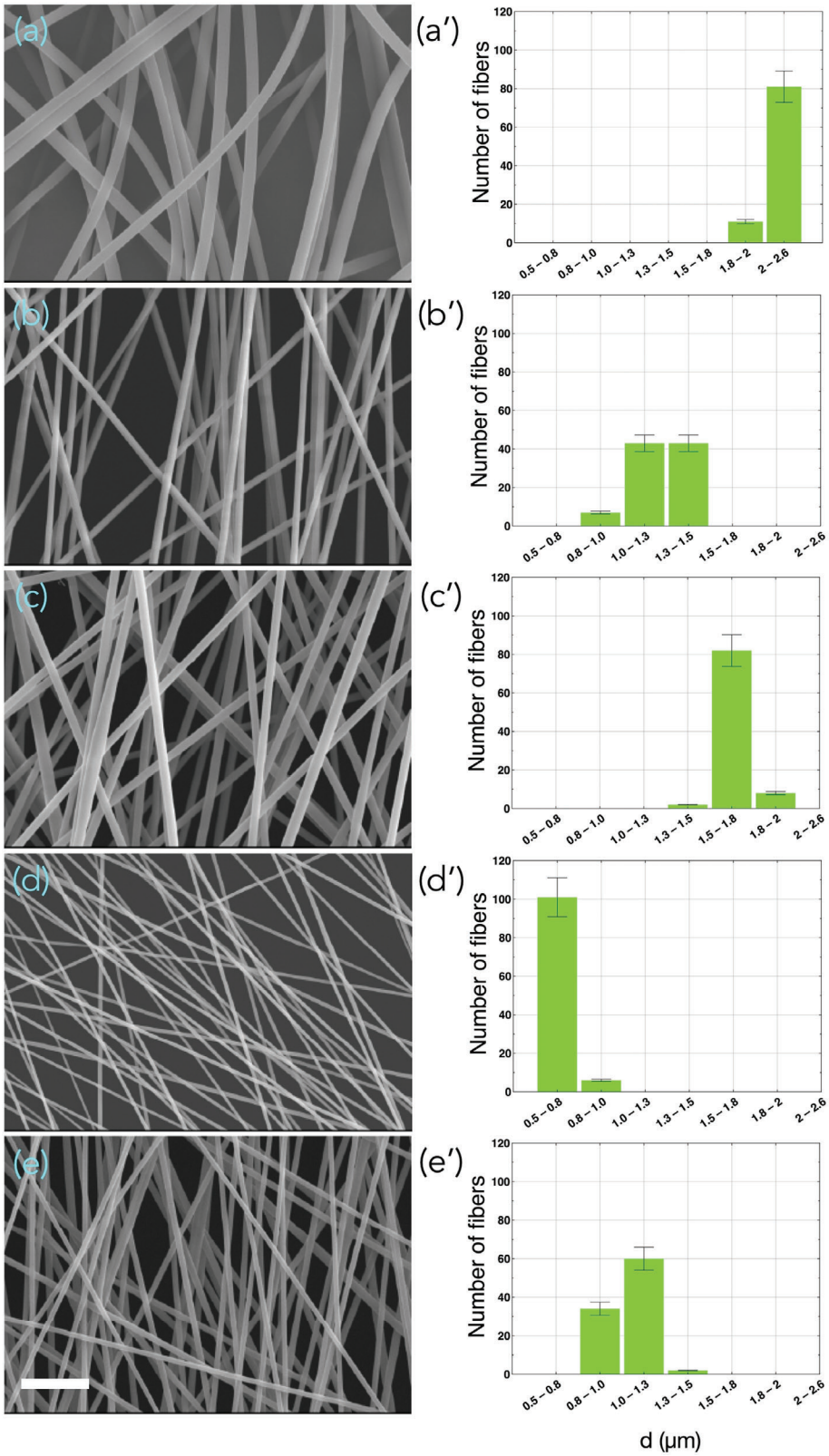

Figure 4. Left column: representative SEM images of the fibers produced from each of the five viscosity-matched solutions (compositions in Table 1). Scale bar 5 μm. Right column: histograms showing the distribution of cross section diameters d of fibers spun from each solution. The corresponding Taylor cone movies are provided in Supporting Information, and key snapshots are shown in Figure 3.The error bars on the histograms represent standard deviation.

attribute to this microphase segregation reaching its maximum, linking it to Ben-Naim's identification of this mole fraction as having maximum affinity of ethanol molecules but minimum affinity between ethanol and water.[51] We can thus conclude that the mole fraction where we find a maximum PAA solution viscosity corresponds to the conditions where the ethanol–water mixture is the furthest from ideal, with a microphase segregation of water and ethanol which is at its maximum.

The key remaining question is why this extreme condition yields maximum viscosity of PAA solutions, suggesting maximally expanded coils and an optimum solution behavior for PAA, whereas the same solvent mixture shows an extreme in poor solvent behavior for PVP.[46] We assume that this is related to the ionizable acid groups of PAA and the fact that the counter ions of the carboxyl pendants of PAA are protons (H^+), rendering the degree of ionization highly sensitive to pH. The acidic nature of PAA thus itself influences its degree of deprotonation. For aqueous PAA solutions set to pH <5 by a low molar mass acid, Swift et al. found the deprotonation of the carboxyl groups to be negligible.[58] In our case, pH<5 for $c_{PAA} \geq 6\%$ w/w for all x_w (see Figure S10, Supporting Information), which means that the average degree of ionization of PAA must be low, explaining why ethanol is overall the better solvent. Indeed, we find a slight turbidity in the solutions with high water content, whereas those with high ethanol content are clear (Figure S11, Supporting Information). However, the low pH comes from protonation of PAA in the first place; hence, ionization up to a saturation fraction does occur along the chains. This gives them polyelectrolyte character with electrostatic self repulsion along the polymer chain, increasing the persistence length and therefore expanding the coil in solution. As the ethanol fraction of the solvent increases, pH also increases, reflecting the expected reduced degree of ionization as the solvent permittivity decreases. This means a decreasing electrolyte character, with a consequent reduced impact of electrostatic coil expansion. The variation of PAA ionization should be reflected by a corresponding variation of solution conductivity, which would suggest that the fiber thickness increases with ethanol content, as high conductivity is known to decrease the fiber diameter.[1–5] However, the results in Figure 4 show a dependence on solvent composition that is not fully systematic, suggesting that the conductivity impact is overlaid by other effects, to be discussed below.

We conjecture that the maximum viscosity at constant c_{PAA} at $n_w \approx 0.65$ is a result of maximally expanded coils because of all the different aspects influencing the PAA chain interactions contributing synergistically at this apparently optimum solvent mixture composition. The benefit of water's ability to deprotonate the PAA is combined with ethanol's ability to solubilize the protonated residues (in majority), and the partial charging of the polymer expands the coil via the electrostatically increased persistence length. These effects are then amplified by the fact that the entropic penalty of microphase segregation of ethanol and water is maximized at $w_x \approx 0.6$.[52] The presence of partially ionized PAA could reduce the free energy of the solvent by having the water molecules interacting mainly with deprotonated acid groups while the ethanol interacts mainly with the protonated ones and the polymer backbone, as has indeed been suggested by molecular dynamics simulations.[59] In other words, the polymer–solvent interactions are particularly strong at $w_x \approx 0.6$, as each fraction of the polymer, protonated and deprotonated, respectively, interacts preferentially with one of the two solvent species, reducing the entropy penalty of direct ethanol–water interaction at this maximally nonideal mixing ratio. Hammouda et al. also found that a mixture of ethanol and water promotes PAA dissolution[60] and they also attributed the effect to a molecular scale solvent segregation. However, their conjecture that water dissolves mainly the carboxylate groups—regardless of degree of deprotonation—whereas the ethanol dissolves mainly the backbone would suggest that water–alcohol mixtures would be better solvents also for PVP and PEO, in contradiction with the findings of Guettari et al.[46] and Shankar et al.[47] Future more detailed investigations, in particular involving computer simulations, are needed to gain a full understanding of the phenomena.

Next, we attempt to explain the apparently unsystematic variations in fiber cross section diameter $\bar{d}$ between the five solutions used for electrospinning seen in Figure 4 and Table 2. We believe that this is due to the fact that the impact on the electrospinning results of η—which is similar for all five solutions as they were prepared—is dwarfed by the changes to the solvent composition taking place over time in the Taylor cone. This thus gives rise to the significant variations in cycle length and Taylor cone shape seen in Figure 3, but it also impacts the characteristics of the fibers that finally end up on the collector. We recently found that the cooling due to ethanol evaporation from the Taylor cone of an ethanolic PVP solution electrospun in a humid atmosphere leads to significant water condensation, which—counterintuitively—leads to gelation of the Taylor cone surface and disruption of the electrospinning process.[40] This surprising finding can be understood from the fact that water condensation actually accelerates ethanol or methanol evaporation due to the latent heat released when water condenses.[61]

We believe the same phenomenon is at play here, despite a significantly lower atmospheric humidity. Most likely, the well-known hygroscopic nature of PAA (the most common application of PAA is as a superabsorbant material due to its ability to absorb water and swell to many times its own volume) contributes to an extreme sensitivity to humidity, the PAA effectively promoting water condensation and thus triggering the enhanced ethanol evaporation. This explains why the outer surface of the Taylor cone of PAA in pure ethanol gels so quickly, terminating the spinning cycle after about 30 s in Figure 3, and it also explains why the Taylor cone always grows in volume over time within a spinning cycle, despite the flow rate being slightly lower than typical for electrospinning. In fact, Q was as low as possible in all experiments, any further reduction effectively stopping the initial Taylor cone development. If water is present in the spinning solution from the start, the impact on ethanol evaporation is reduced in magnitude, but the gelation of the Taylor cone is nevertheless strong enough to also terminate the cycle in spinning experiments with Solutions 2 and 3.

With Solution 5, there is no ethanol that can evaporate, as the solvent is pure water. In this case, consequently, the cycle is not terminated by surface gelation of the Taylor cone, but by an extreme growth of the droplet protruding from the spinneret to the point that it can hardly be described as a Taylor cone any more and where an operator must remove it in order to avoid dripping onto the fiber mat. It must be emphasized that this is not due to overfeeding because of too high flow rate; Q is the second lowest in

the study for Solution 5. Rather, we believe it is the fact that c_{PAA} is the highest of all solutions, in order to reach the targeted η_0 in this nonoptimum solvent. The large PAA loading leads to maximum impact of the hygroscopic nature of PAA, drawing in additional water from the air as spinning proceeds. While it may seem surprising that PAA could act to draw in additional water from the air when it already is in solution, one should be aware that significant phase separation takes place during electrospinning in the Taylor cone, near the apex from which the jet is ejected.[62] This means that the PAA concentration can be high locally, allowing it to absorb additional water at these locations.

We believe the low value of $\bar{d}$ seen when spinning solution 4 is the one truly representative of the viscosity-matched solutions. This solution has a quite low c_{PAA}, reducing the impact of its hygroscopic nature, and a relatively low ethanol content, eliminating the risk of Taylor cone gelation due to water condensation. The other fibers have $\bar{d}$ that are more determined by the dynamic variations of the PAA solution at the Taylor cone surface during spinning, due to water condensing from the air.

4. Conclusion

While PAA dissolves in ethanol as well as water, or any mixture of the two, its behavior changes in a highly nonlinear and nontrivial way as the solvent composition is varied. Surprisingly, the viscosity η at constant PAA concentration c_{PAA} is maximum at a water-to-ethanol mole fraction of $x_w \approx 0.65$, corresponding to maximum deviation from ideal mixing behavior of water and ethanol. We believe it provides a synergistic combination of partial deprotationation of carboxylate groups by water while the ethanol dissolves the remaining uncharged polymer fraction. Having established how η varies with x_w we find that consistent electrospinning of PAA solutions of any water–ethanol solvent ratio can be initiated with $\eta \approx 0.7$ Pa s, but the fiber cross section diameter varies in apparently inconsistent ways, and the spinneret must be regularly wiped clean, due to an unavoidable rapid growth of the Taylor cone and/or gelation in case of ethanol-rich solutions. We attribute this behavior to the extreme hygroscopic nature of PAA, leading to significant water condensation into the Taylor cone despite a spinning atmosphere with moderate relative humidity. This demonstrates the vital importance of monitoring the Taylor cone quality over time during electrospinning and paying attention to any unexpected processes taking place there, which may impact the electrospinning process.

5. Experimental Section

Polymer Solutions: Poly(acrylic acid) (PAA; $M_w = 450$ kg mol^{-1}) was purchased from Sigma-Aldrich and dissolved in anhydrous ethanol (99%, from VWR) for solutions in pure ethanol, ultrapure deionized water (conductivity 0.055 μS cm^{-1} Sartorius Arium) for solutions in pure water, or mixtures of the two solvents. Multiple PAA solutions were prepared, with various selected concentrations c_{PAA} (by mass), in water–ethanol mixtures of 0, 25, 50, 75, and 100% w/w ratio. All materials were used as received without further purification.

Viscosity Measurements: The oscillatory shear viscosity η was measured in plate-plate geometry (50 mm diameter, 1.0 mm gap) using an Anton Paar rheometer (MRC-102), controlled by Rheocompass software. The shear rate $\dot{\gamma}$ was swept from 0.1 to 10 s^{-1} and then back to 0.1 s^{-1}. All the measurements were performed at room temperature (25 °C), using a solvent trap to prevent ethanol from evaporating during the measurements.

Electrospinning: The electrospinning setup (vertical geometry, schematic in Figure S1, Supporting Information) was housed inside a closed acrylic box in order to ensure a well-defined spinning atmosphere. An 18-gauge blunt-tipped disposable stainless steel needle (outer diameter 1.20 mm), purchased from VWR, was used as the spinneret, mounted in the top of the acrylic box. To apply the electric field to drive spinning, the spinneret was connected to a high voltage power supply (Gamma High Voltage, model ES30R-5W/DAM/RS232) while the collector was grounded. The PAA solution to be spun was pumped to the spinneret using a microfluidic pressure controller (Fluigent, model MFCS-EZ, maximum pressure 1034 mbar, uncertainty ± 0.3 mbar). The Taylor cone was imaged using a digital camera (Pixelink D755) equipped with a macro lens (Tokina AT-X Pro).

For all experiments, a spinneret–collector distance of 14 cm and a spinning voltage of 7.5 kV were chosen. The temperature T and relative humidity RH were monitored during all experiments, and the flow rate Q was adjusted for maximally stable spinning for each solution. Fibers were collected freely hanging on an untreated copper wire frame.

Electron Microscopy Characterization: The fibers were characterized using a JEOL JSM-6010LA SEM (Akishima, Japan), operated at 20 kV with a working distance of 11 mm. Prior to imaging, the fibers were coated with gold (≈5 nm thickness) using a sputter coater (Quorum Q150R ES) for 100 s. The fiber cross section diameter was established by randomly selecting at least 100 fibers from the SEM images and measuring the apparent cross section using the software ImageJ (NIH, USA).

Supporting Information

Supporting Information is available from the Wiley Online Library or from the author.

Acknowledgements

Funding for this research was provided by a European Research Council Consolidator Grant (INTERACT, grant number 648763) and by an *Aide à la formation-recherche* grant (LIMEFLOW, grant number 9784104) from the Luxembourg National Research Fund. The authors thank Nicolas Tournier, Dr. Ulrich M. Siegel, Dr. Catherine G. Reyes, and Dr. Hakam Agha for assistance in constructing the experimental set-up; Dr. Alex Gansen, Claudius M. Lehr, Dr. Jörg Baller, and Prof. Jeanne H. Norton for assistance with the rheological characterization; Zornitza Tosheva for helping with SEM imaging and pH measurements; and Dr. Manos Anyfantakis and Dr. V.S.R. Jampani for fruitful discussions.

Conflict of Interest

The authors declare no conflict of interest.

Data Availability Statement

The data that support the findings of this study are available from the corresponding author upon reasonable request.

Keywords

electrospinning, ethanol, poly(acrylic acid), polymers, solvents, viscosity, water

Received: August 27, 2021
Revised: October 29, 2021
Published online:

[1] S. Ramakrishna, K. Fujihara, W.-E. Teo, T.-C. Lim, Z. Ma, *An Introduction to Electrospinning and Nanofibers Electrospinning Process*, Vol. *3*, World Scientific, Singapore **2005**.
[2] G. Rutledge, S. Fridrikh, *Adv. Drug Delivery Rev.* **2007**, *59*, 1384.
[3] D. Reneker, A. Yarin, *Polymer* **2008**, *49*, 2387.
[4] J. H. Wendorff, S. Agarwal, A. Greiner, *Electrospinning: Materials, Processing, and Applications*, Wiley-VCH, Weinheim **2012**.
[5] J. Xue, T. Wu, Y. Dai, Y. Xia, *Chem. Rev.* **2019**.
[6] M. Urbanski, C. G. Reyes, J. Noh, A. Sharma, Y. Geng, V. S. R. Jampani, J. P. F. Lagerwall, *J. Phys.: Condens. Matter* **2017**, *29*, 133003.
[7] J. H. Park, G. C. Rutledge, *Macromolecules* **2017**, *50*, 5627.
[8] M. Jasiurkowska-Delaporte, E. Juszyńska-Gałązka, W. Sas, P. M. Zieliński, A. Baranowska-Korczyc, *J. Mol. Liq.* **2021**, *331*, 115817.
[9] A. E. Mamuk, Ç. Koçak, Ç. E. Demirci Dönmez, *Colloid Polym. Sci.* **2021**.
[10] K. T. Dicker, D. Ratchford, R. Casalini, M. D. Thum, J. H. Wynne, J. G. Lundin, *Langmuir* **2020**, *36*, 7916.
[11] G. Scalia, E. Enz, O. Calò, D. K. Kim, M. Hwang, J. H. Lee, J. P. F. Lagerwall, *Macromol. Mater. Eng.* **2013**, *298*, 583.
[12] D. K. Kim, M. Hwang, J. P. F. Lagerwall, *J. Polym. Sci., Part B: Polym. Phys.* **2013**, *51*, 855.
[13] E. Enz, V. La Ferrara, G. Scalia, *ACS Nano* **2013**, *7*, 6627.
[14] A. L. Medina-Castillo, J. F. Fernández-Sánchez, A. Fernández-Gutiérez, *Adv. Funct. Mater.* **2011**, *21*, 3488.
[15] E. Enz, J. P. F. Lagerwall, *J. Mater. Chem.* **2010**, *20*, 6866.
[16] E. Enz, U. Baumeister, J. Lagerwall, *Beilstein J. Org. Chem.* **2009**, *5*, 58.
[17] J. P. F. Lagerwall, J. T. McCann, E. Formo, G. Scalia, Y. Xia, *Chem. Commun.* **2008**, *42*, 5420.
[18] J. E. Díaz, A. Barrero, M. Márquez, I. G. Loscertales, *Adv. Funct. Mater.* **2006**, *16*, 2110.
[19] P. Rathore, J. Schiffman, *ACS Appl. Mater. Interfaces* **2021**, *13*, 48.
[20] D. Han, A. Steckl, *Chempluschem* **2019**, *84*, 1453.
[21] A. Yarin, *Polym. Adv. Technol.* **2011**, *22*, 310.
[22] L. Bellan, H. Craighead, *Polym. Adv. Technol.* **2011**, *22*, 304.
[23] J. Wang, A. Jákli, J. L. West, *J. Mol. Liq.* **2018**, *267*, 490.
[24] J. Wang, A. Jákli, J. West, *ChemPhysChem* **2016**, *17*, 3080.
[25] E. A. Buyuktanir, M. W. Frey, J. L. West, *Polymer* **2010**, *51*, 4823.
[26] S. Ji, Y. Li, M. Yang, *Sens. Actuators, B* **2008**, *133*, 644.
[27] Y. Kye, C. Kim, J. P. F. Lagerwall, *J. Mater. Chem. C* **2015**, *3*, 8979.
[28] C. G. Reyes, A. Sharma, J. P. F. Lagerwall, *Liq. Cryst.* **2016**, *43*, 1986.
[29] L. Pschyklenk, T. Wagner, A. Lorenz, P. Kaul, *ACS Appl. Polym. Mater.* **2020**, *2*, 1925.
[30] M. J. Bertocchi, P. Vang, R. B. Balow, J. H. Wynne, J. G. Lundin, *ACS Appl. Polym. Mater.* **2019**, *1*, 2068.
[31] M. D. Thum, D. C. Ratchford, R. Casalini, J. H. Wynne, J. G. Lundin, *ACS Appl. Nano Mater.* **2021**, *4*, 297.
[32] N. Wang, H. Chen, L. Lin, Y. Zhao, X. Cao, Y. Song, L. Jiang, *Macromol. Rapid Commun.* **2010**, *31*, 1622.
[33] J. McCann, M. Marquez, Y. Xia, *Nano. Lett.* **2006**, *6*, 2868.
[34] J. Park, P. Braun, *Adv. Mater.* **2009**, *22*, 496.
[35] B. Pant, M. Park, S.-J. Park, *Pharmaceutics* **2019**, *11*, 305.
[36] K. Khoshnevisan, H. Maleki, H. Samadian, S. Shahsavari, M. Sarrafzadeh, B. Larijani, F. Dorkoosh, V. Haghpanah, M. Khorramizadeh, *Carbohydr. Polym.* **2018**, *198*, 131.
[37] S. Chou, D. Carson, K. Woodrow, *J. Controlled Release* **2015**, *220*, 584.
[38] W. Ji, Y. Sun, F. Yang, J. van den Beucken, M. Fan, Z. Chen, J. Jansen, *Pharm. Res.* **2011**, *28*, 1259.
[39] A. Saraf, L. Baggett, R. Raphael, F. Kasper, A. Mikos, *J. Controlled Release* **2010**, *143*, 95.
[40] C. G. Reyes, J. P. Lagerwall, *ACS Appl. Mater. Interfaces* **2020**, *12*, 26566.
[41] K. Terao, in *Encyclopedia of Polymeric Nanomaterials* (Eds: S. Kobayashi, K. Müllen), Springer, Berlin, Heidelberg **2021**, pp. 1–6.
[42] J. O. Iroh, in *Polymer Data Handbook* (Ed: J. Mark), Oxford University Press, New York **1999**, pp. 558–560.
[43] L. Li, Y. Hsieh, *Nanotechnology* **2005**, *16*, 2852.
[44] Y. B. Truong, J. Choi, J. Mardel, Y. Gao, S. Maisch, M. Musameh, I. L. Kyratzis, *Macromol. Mater. Eng.* **2017**, *302*, 1700024.
[45] I. Ismail, N. Bakar, T. Ling, N. Ideris, Z. Zain, N. Radacsi, *Mater. Today: Proc.* **2019**, *17*, 574.
[46] M. Guettari, A. Belaidi, S. Abel, T. Tajouri, *J. Solution Chem.* **2017**, *46*, 1404.
[47] R. Shankar, R. R. Klossner, J. T. Weaver, T. Koga, J. H. van Zanten, W. E. Krause, C. M. Colina, F. Tanaka, R. J. Spontak, *Soft Matter* **2009**, *5*, 304.
[48] G. Smolyakov, J.-M. Catala, N. Kutsevol, M. Rawiso, in *Modern Problems of Molecular Physics* (Eds: L. A. Bulavin, A. V. Chalyi), Springer, Cham **2018**, pp. 133–147.
[49] X. Meng, Y. Du, Y. Liu, E. B. Coughlin, S. L. Perry, J. D. Schiffman, *Macromolecules* **2021**, *54*, 5033.
[50] S. K. Tiwari, S. S. Venkatraman, *Mater. Sci. Eng.: C* **2012**, *32*, 1037.
[51] A. Ben-Naim, *J. Chem. Phys.* **1977**, *67*, 4884.
[52] T. Sato, A. Chiba, R. Nozaki, *J. Chem. Phys.* **1999**, *110*, 2508.
[53] J. Ott, J. Sipowska, M. Gruszkiewicz, A. Woolley, *J. Chem. Thermodyn.* **1993**, *25*, 307.
[54] I. Abdulagatov, L. A. Akhmedova-Azizova, N. Azizov, *Fluid Phase Equilib.* **2014**, *376*, 1.
[55] R. Belda, J. V. Herráez, O. Diez, *Phys. Chem. Liq.* **2004**, *42*, 467.
[56] D. Chandler, *Nature* **2005**, *437*, 640.
[57] S. Song, C. Peng, *J. Dispersion Sci. Technol.* **2008**, *29*, 1367.
[58] T. Swift, L. Swanson, M. Geoghegan, S. Rimmer, *Soft Matter* **2016**, *12*, 2542.
[59] S. Srikant, S. S. Muralidharan, U. Natarajan, *Mol. Simul.* **2013**, *39*, 145.
[60] B. Hammouda, F. Horkay, M. L. Becker, *Macromolecules* **2005**, *38*, 2019.
[61] C. Law, T. Xiong, C. Wang, *Int. J. Heat Mass Transfer* **1987**, *30*, 1435.
[62] C. Wang, T. Hashimoto, *Macromolecules* **2020**, *53*, 9584.

Supplementary Information for "Electrospinning ethanol–water solutions of poly(acrylic acid): non-linear viscosity variations and sensitivity to air humidity"

Shameek Vats, Lawrence W. Honaker, Margaret W. Frey, Francesco Basoli, and Jan P.F. Lagerwall

A Electrospinning set-up and conditions

Figure S1 shows a schematic of the electrospinning setup discussed in the Experimental section and used for these experiments.

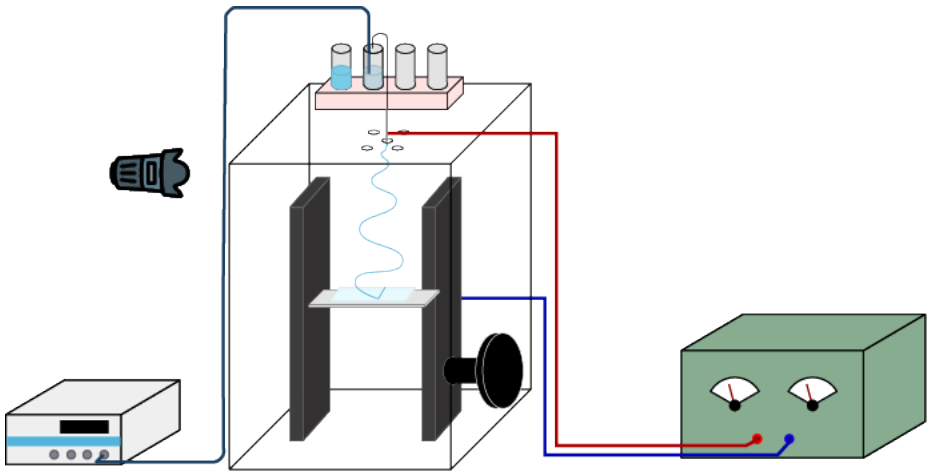

Figure S1: The schematics of the setup used for electrospinning microfibers

The parameters under which spinning took place are shown in Table S1.

Table S1: Electrospinning parameters and conditions

PAA Concentration	Relative Humidity(%)	Temperature (°C)	Distance (cm)	Voltage (kV)	Flow rate (ml/h)
10% w/w	29	25.1	14	7.5	0.61
7.5% w/w	30	24.8	14	7.5	0.65
7% w/w	30	24.5	14	7.5	0.43
8.5% w/w	35	26.3	14	7.5	0.23
11.5% w/w	35	25.9	14	7.5	0.37

The flow rates indicated in Table S1 were calculated from the Hagen-Poiseuille equation (equation 1) for the pressure drop between two ends of a pipe or tube:

$$\Delta p = \frac{8\eta L Q}{\pi R^4} \tag{1}$$

where Δp is the pressure difference between the ends of the tube, Q the volumetric flow rate, η the viscosity, R the cross-sectional radius of the tube, and L its length. Simple rearrangement allows us to express Q in terms of the input parameters (most notably, Δp, L, and R):

$$Q = \frac{\Delta p \pi R^4}{8\eta L} \tag{2}$$

The parameters used in equation 2 to calculate the flow rates are indicated in Table S2.

B PAA solutions and their viscosities

To establish the critical entanglement concentration of our PAA in water, we replot the viscosity data from Li and Hsieh [43], obtained for the same type of PAA, in log-log scale, together with best power

PAA concentration (∼w/w)	η (Pa·s)	R (m) $\times 10^{-4}$	L (m)	Δ p (mbar)	Q (ml/h)
10%	0.86	4.0	0.343	50	0.61
7.5%	0.65	4.0	0.343	40	0.65
7%	0.73	4.0	0.343	30	0.43
8.5%	0.9	4.0	0.343	20	0.23
11.5%	0.85	4.0	0.343	30	0.37

Table S2: The measured values of the parameters used to calculate the flow rate.

law fits to these data, in Fig. S2. The linear character with twice the slope at high concentration suggest that $c_{PAA} \approx 5.5$ % w/w corresponds to the critical entanglement concentration.

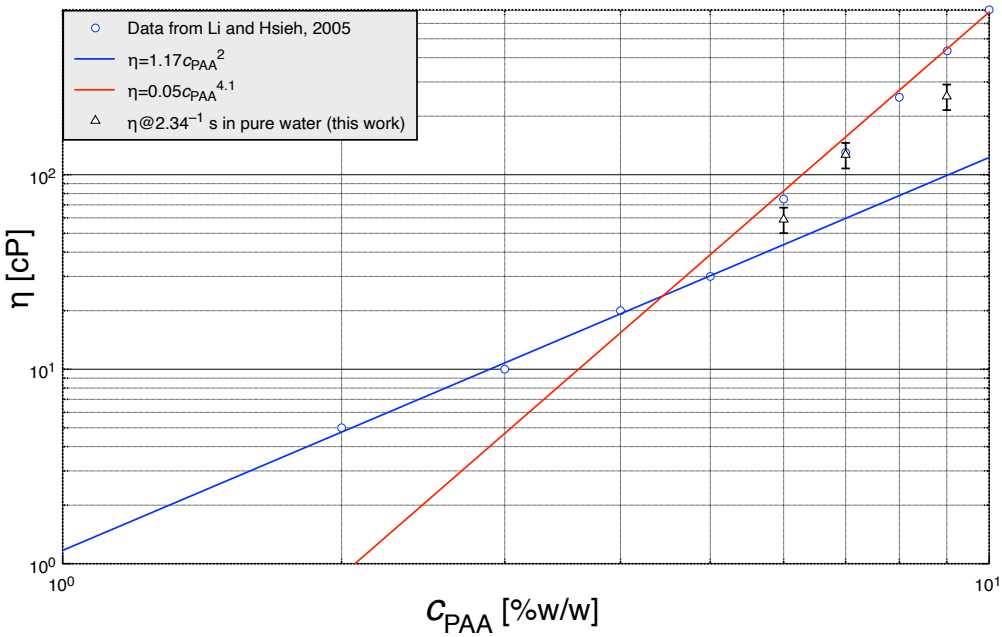

Figure S2: Log-log plot of shear viscosity η versus PAA concentration c_{PAA} in water, using experimental data extracted from Li and Hsieh [43] as well as data from this study. The two power law curves are best fits to the Li and Hsieh data at $c_{PAA} < 5.5$ % w/w and > 5.5 % w/w, respectively, corresponding to unentangled and entangled solution behavior. The error bars represent a standard deviation obtained from four different measurements, each with increasing and decreasing shear rate.

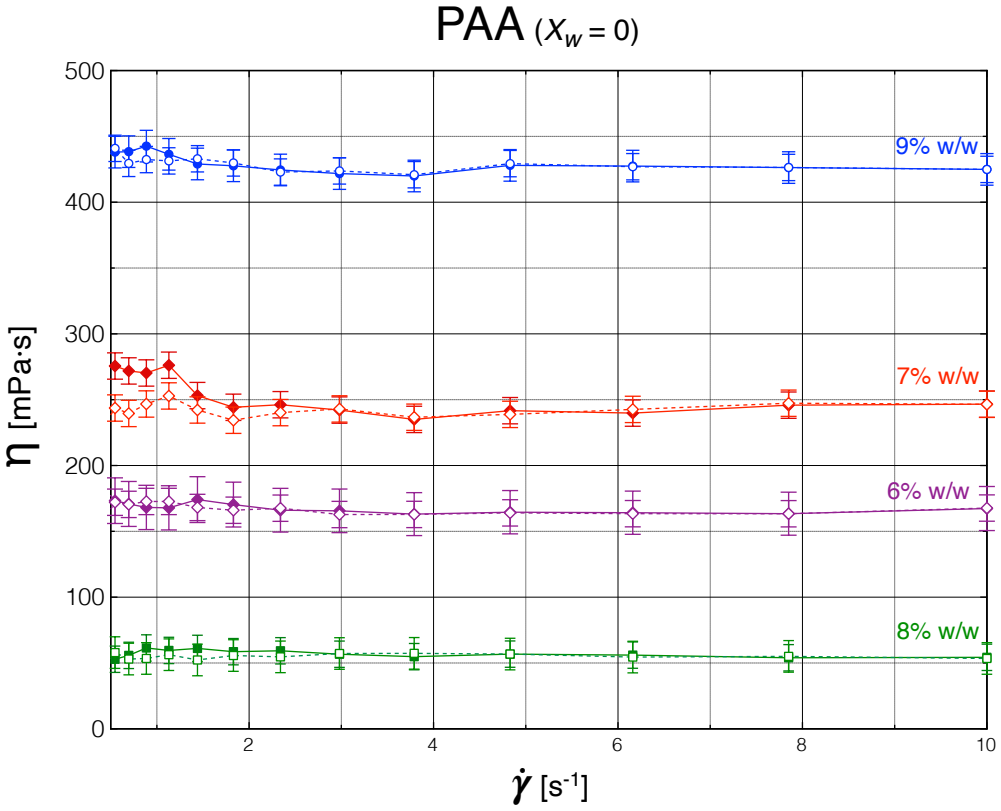

Figure S3: Viscosity η as a function of shear rate $\dot{\gamma}$ for different mass concentrations c_{PAA} of PAA, dissolved in pure ethanol. The error bars represent a standard deviation obtained from four different measurements, each with increasing and decreasing shear rate.

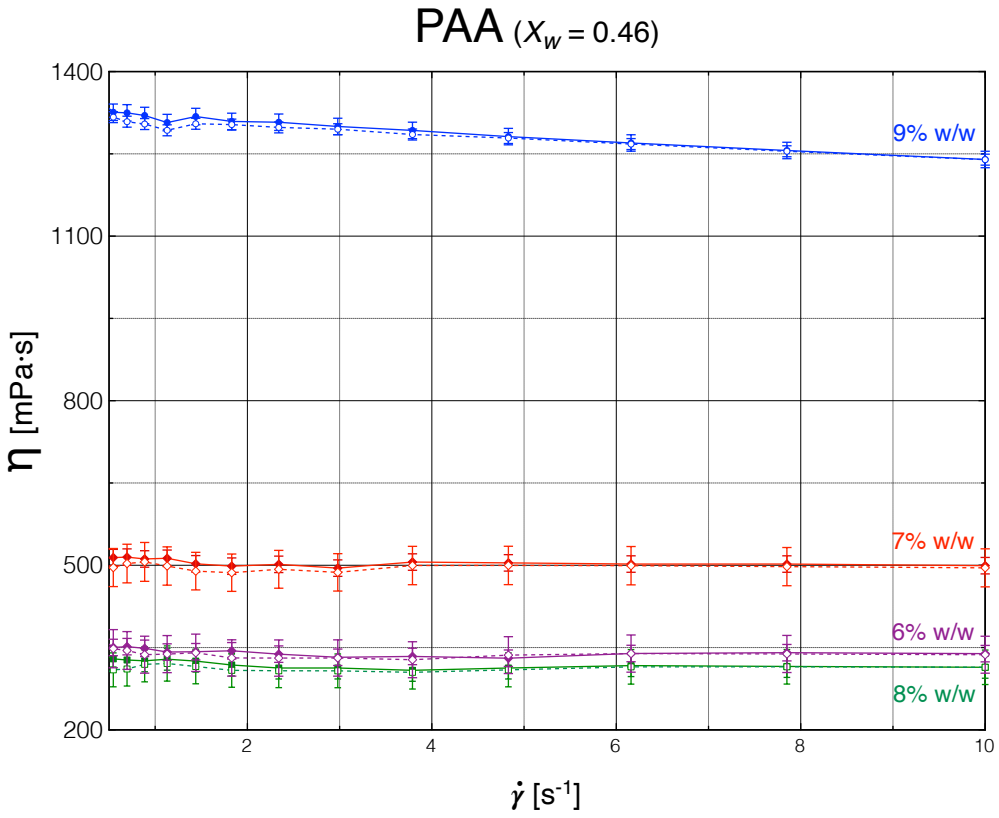

Figure S4: Viscosity η as a function of shear rate $\dot{\gamma}$ for different mass concentrations c_{PAA} of PAA, dissolved in a mixture of water and ethanol with $X_W = 0.46$. The error bars represent a standard deviation obtained from four different measurements, each with increasing and decreasing shear rate.

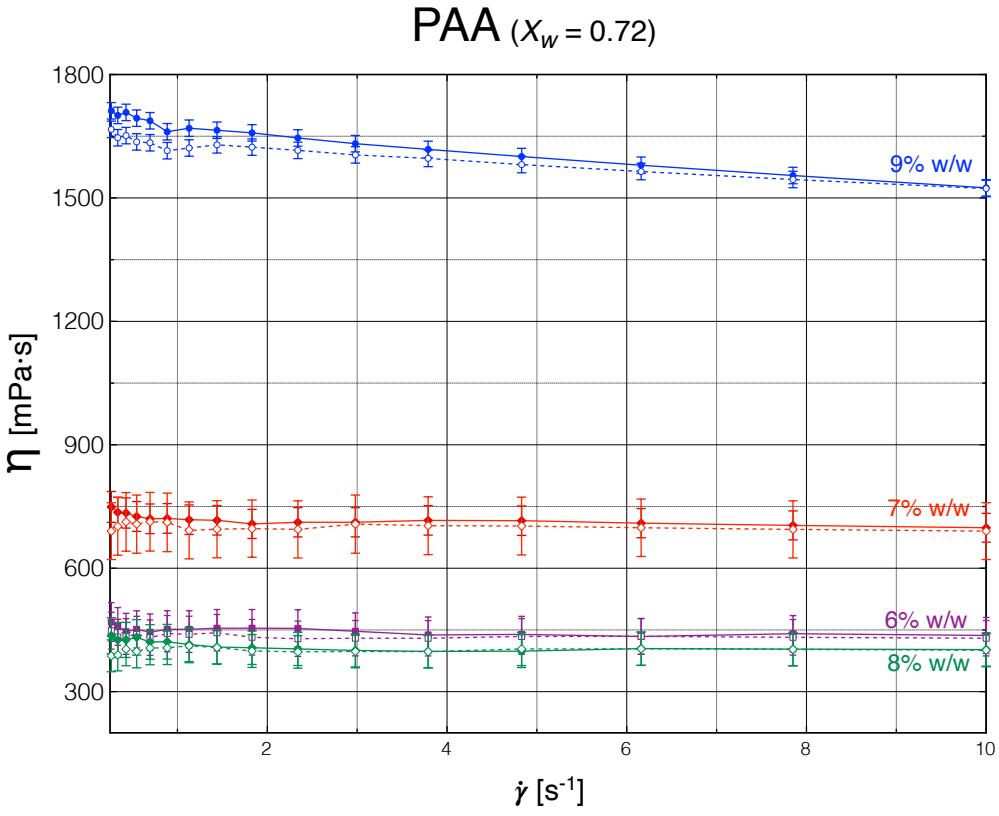

Figure S5: Viscosity η as a function of shear rate $\dot{\gamma}$ for different mass concentrations c_{PAA} of PAA, dissolved in a mixture of water and ethanol with $X_W = 0.72$. The error bars represent a standard deviation obtained from four different measurements, each with increasing and decreasing shear rate.

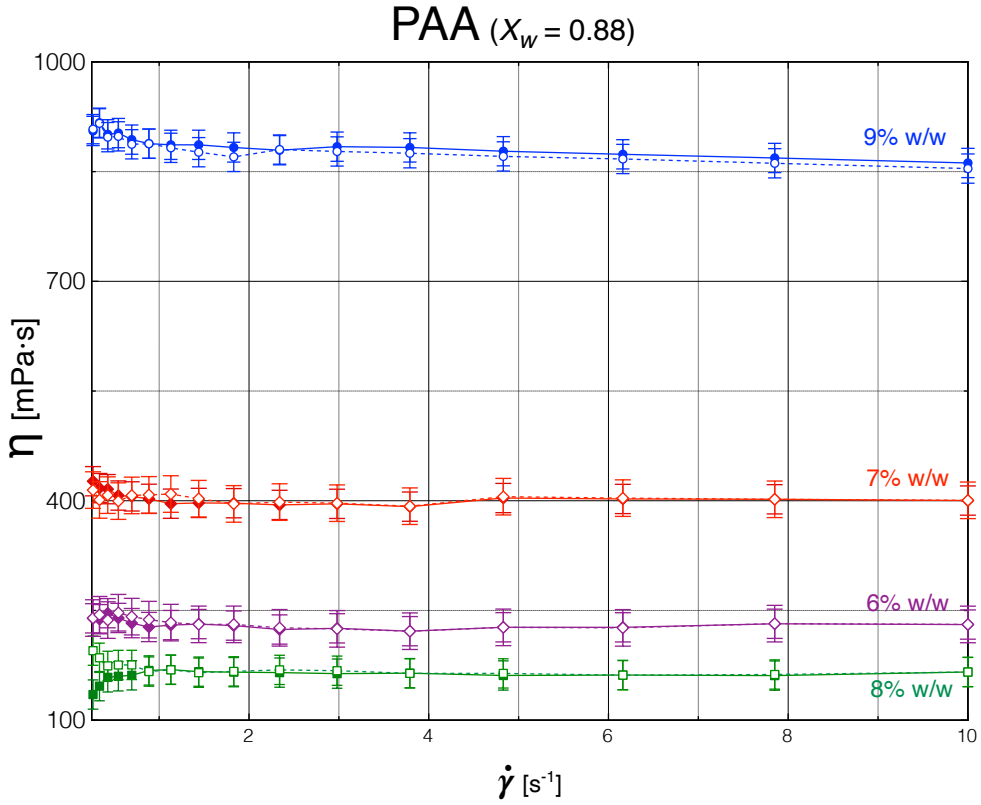

Figure S6: Viscosity η as a function of shear rate $\dot{\gamma}$ for different mass concentrations c_{PAA} of PAA, dissolved in a mixture of water and ethanol with $X_W = 0.88$. The error bars represent a standard deviation obtained from four different measurements, each with increasing and decreasing shear rate.

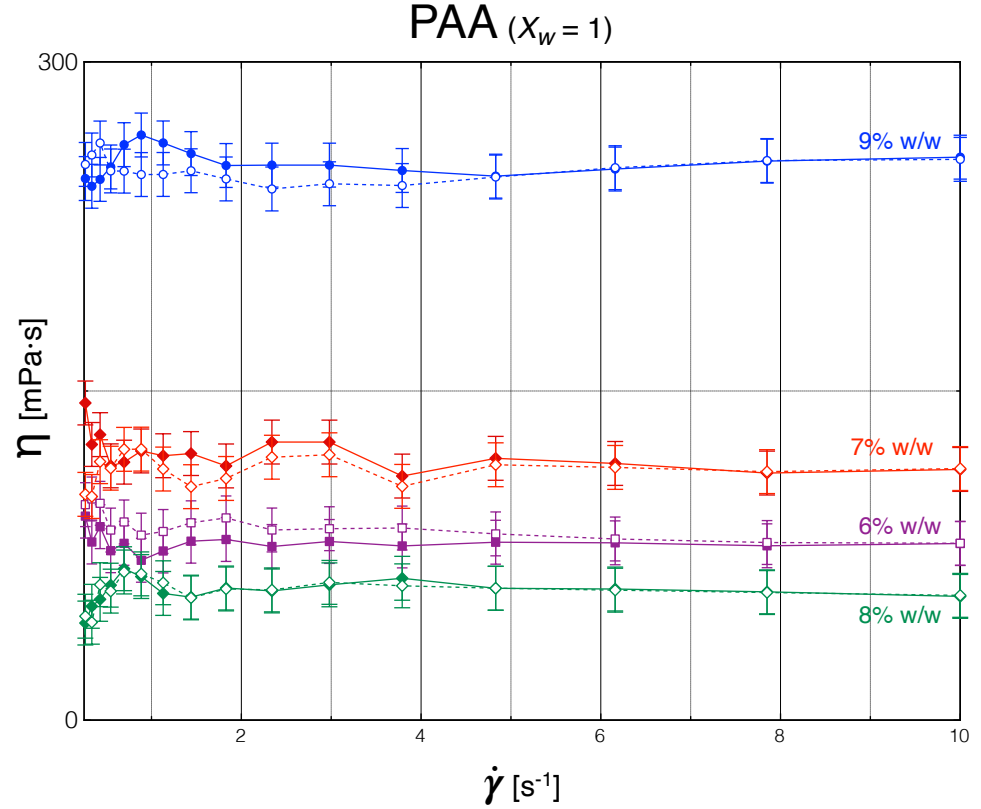

Figure S7: Viscosity η as a function of shear rate $\dot{\gamma}$ for different mass concentrations c_{PAA} of PAA, dissolved in pure water. The error bars represent a standard deviation obtained from four different measurements, each with increasing and decreasing shear rate.

C Anomalous 8% w/w PAA

The reason that $c_{PAA} = 8\%$ w/w is excluded from Fig. 2 in the main paper is that this concentration displayed anomalous behavior during the viscosity measurements. Throughout four attempts we could not get reproducible values, and in one attempt the instrument repeatedly produced negative η. The data at $\dot{\gamma} = 2.34\ \mathrm{s}^{-1}$ from all four attempts, for all five solvent compositions investigated, are shown in Fig. S8, for both increasing and decreasing shear rate $\dot{\gamma}$. We conclude that the PAA solution in this concentration range exhibits a behaviour outside the measurement conditions of the rheometer; hence we do not include them in Fig. 2. A possible reason for the anomaly may be that this particular c_{PAA} range is subject to strong flow-induced phase separation by spinodal decomposition even at the rather low $\dot{\gamma}$ studied here, [62] yielding a highly inhomogeneous sample that the rheometer cannot handle. While the observation is very interesting, its proper elucidation falls outside the scope of the present work.

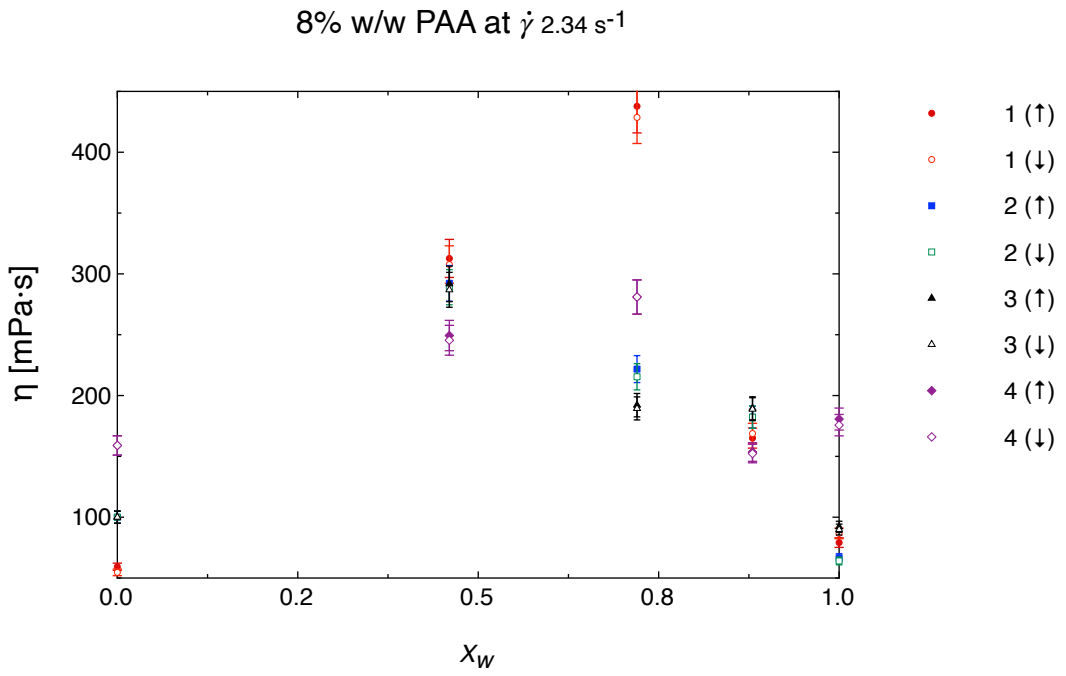

Figure S8: Rheometer output for the viscosity of 8% w/w PAA solutions at a shear rate of $\dot{\gamma} = 2.34\ \mathrm{s}^{-1}$, prepared with different water–ethanol ratios. The upwards arrow with solid data points shows increasing shear rate, while the downward arrow with hollowed data points show decreasing shear rate. The error bars represent the standard deviation calculated from six measurements.

D Viscosities of solutions optimized for electrospinning

The variation in viscosity η at a shear rate of $\dot{\gamma}$=2.34 s^{-1} for the five solutions tuned to have $\eta \approx \eta_0$, making them appropriate for electrospinning regardless of solvent composition, is shown in Fig. S9. The compositions of the solutions are summarized in Table 1 in the main paper.

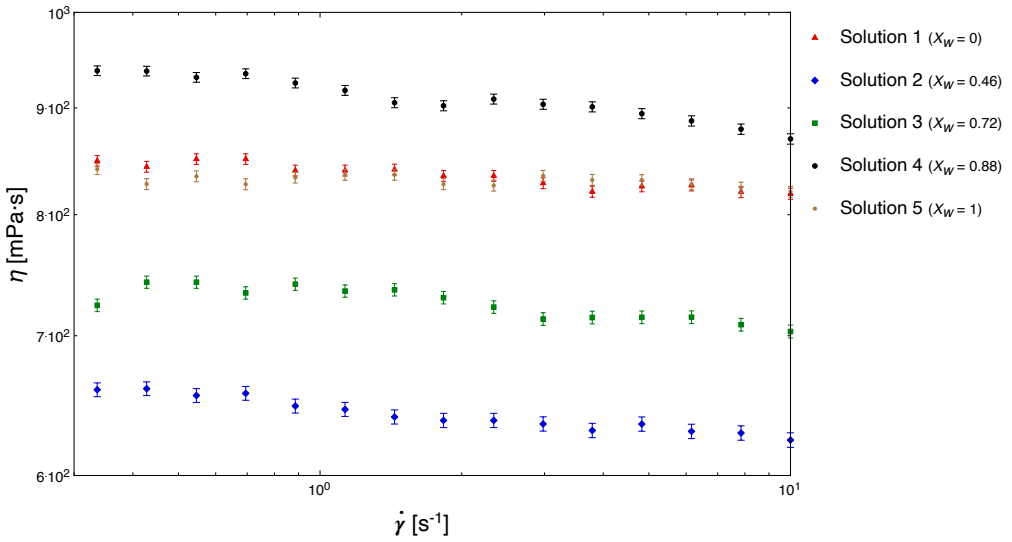

Figure S9: Log-log plot of shear viscosity (η) vs. shear rate ($\dot{\gamma}$) for the PAA solutions in Table 1, with PAA concentration c_{PAA} optimized for constant viscosity regardless of water–ethanol ratio of the solvent mixture. The error bars represent a standard deviation obtained from three different measurements.

E pH measurements

Fresh PAA solutions of 6%, 8%, and 9% w/w were prepared for the pH measurements which were carried out using Hanna pH 211 Microprocessor pH meter at room temperature. The pH values for all the PAA concentration were measured to be lower than 5.

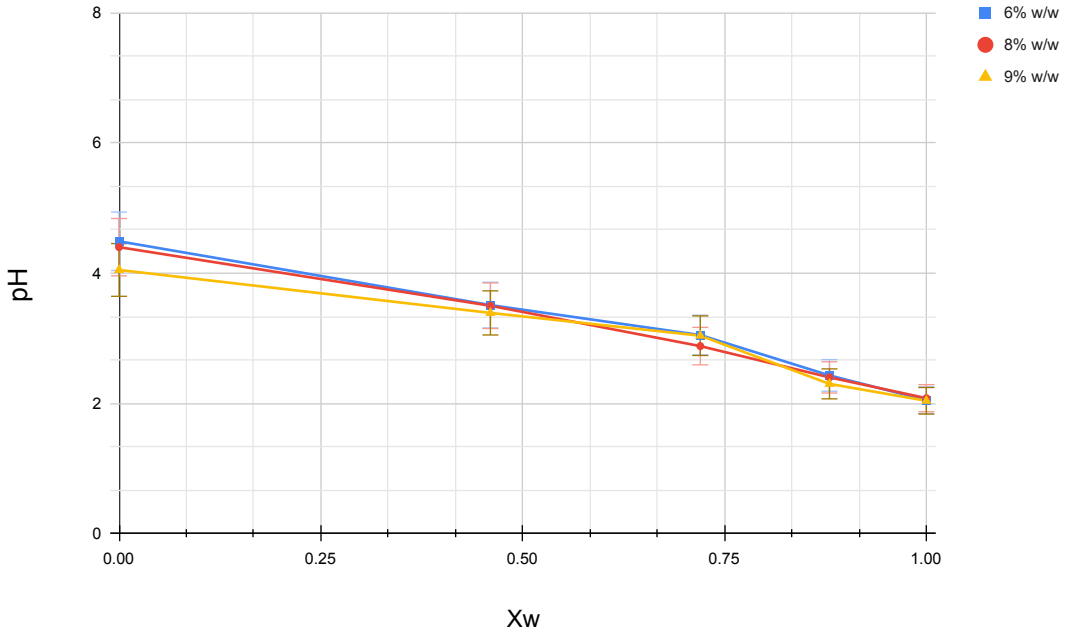

Figure S10: pH values of 6%, 8%, and 9% PAA in different mass ratios of ethanol and water. The error bars represent a standard deviation obtained from three different measurements.

F Visual appearance of PAA solutions with different solvent compositions

Figure S11 shows that solutions of PAA in pure water appear more turbid. As we increase the amount of ethanol in the solution, the turbidity is reduced and the solution becomes clearer (L to R). The samples were imaged after mixing for 30 s on a vortex mixer.

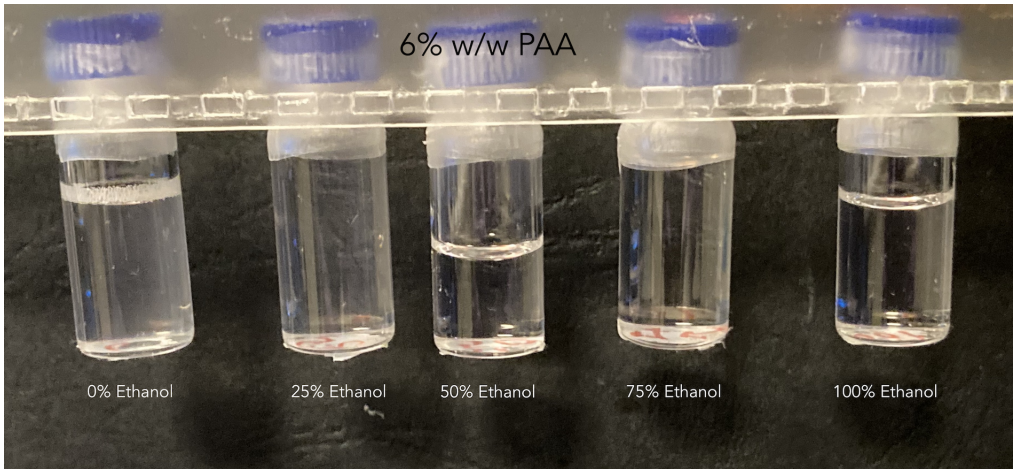

Figure S11: 6% w/w PAA solutions prepared from different ratios of ethanol and water as solvent.

G SI Videos

SI movie 1: Movie of the Taylor cone recorded during electrospinning of Solution 1 ($X_w = 0$), as listed in Table 1. The diameter of the spinneret needle is 1.20 mm and the electrospinning parameters and conditions are listed in the Table S1. This movie corresponds to Figure 3 (a) and (a').
SI movie 2: Movie of the Taylor cone recorded during electrospinning of Solution 2 ($X_w = 0.46$), as listed in Table 1. The diameter of the spinneret needle is 1.20 mm and the electrospinning parameters and conditions are listed in the Table S1. This movie corresponds to Figure 3 (b) and (b').
SI movie 3: Movie of the Taylor cone recorded during electrospinning of Solution 3 ($X_w = 0.72$), as listed in Table 1. The diameter of the spinneret needle is 1.20 mm and the electrospinning parameters and conditions are listed in the Table S1. This movie corresponds to Figure 3 (c) and (c').
SI movie 4: Movie of the Taylor cone recorded during electrospinning of Solution 4 ($X_w = 0.88$), as listed in Table 1. The diameter of the spinneret needle is 1.20 mm and the electrospinning parameters and conditions are listed in the Table S1. This movie corresponds to Figure 3 (d) and (d').
SI movie 5: Movie of the Taylor cone recorded during electrospinning of Solution 5 ($X_w = 1$), as listed in Table 1. The diameter of the spinneret needle is 1.20 mm and the electrospinning parameters and conditions are listed in the Table S1. This movie corresponds to Figure 3 (e) and (e').

3

LIQUID CRYSTALS
https://doi.org/10.1080/02678292.2021.2005166

Taylor & Francis
Taylor & Francis Group

Combining responsiveness and durability in liquid crystal-functionalised electrospun fibres with crosslinked sheath

S. Vats[a], L.W. Honaker[a,b], F. Basoli[c] and J.P.F. Lagerwall[a]

[a]Department of Physics & Materials Science, University of Luxembourg, Luxembourg City, Luxembourg; [b]Laboratory of Physical Chemistry and Soft Matter, Wageningen University & Research, Wageningen, The Netherlands; [c]Department of Engineering, Campus Bio-Medico Di Roma, Rome, Italy

ABSTRACT

Responsive functional composite fibre mats that are mechanically stable and impervious to water exposure are produced by coaxial electrospinning of thermotropic liquid crystal (LC) core inside a water-based solution of poly(vinyl alcohol) (PVA) and poly(acrylic acid) (PAA) forming the sheath. Because thermotropic LCs usually cannot be spun inside water-based solutions due to excessive interfacial tension γ, a n enabling step is the addition of ethanol or dioxane to the LC as a co-solvent compatible with both core and sheath fluids. This reduces γ sufficiently that coaxial jet spinning is possible. After spinning, thermal cross-linking of the PVA+PAA sheath yields LC-functionalised fibres that can be manipulated by hand and remain intact even upon full immersion in water. The LC core retains its behaviour, nematics showing well-aligned birefringence and transitioning to isotropic upon heating above the clearing point, and cholesterics showing selective reflection which is even enhanced upon water immersion due to the removal of sheath scattering. Our results pave the way to producing LC-functionalised responsive fibre mats using durable polymer sheaths, thereby enabling numerous innovative applications in wearable technology, and they also open new opportunities to study LCs in confinement, without visible impact of the container walls.

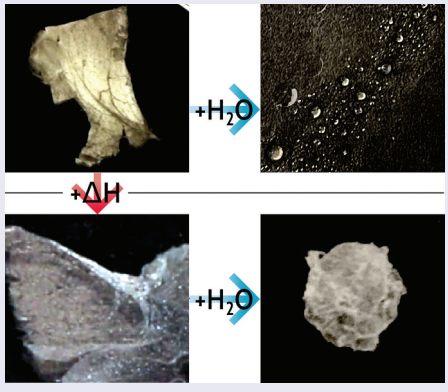

ARTICLE HISTORY
Received 17 September 2021
Accepted 8 November 2021

KEYWORDS
Liquid crystals; cylindrical confinement; functional fibres; electrospinning; crosslinked polymers; water resistance; wearable technology

1. Introduction

Non-woven mats of thin composite fibres produced by electrospinning, in which a polymeric sheath confines and protects one or several cores of liquid crystal (LC), have the potential to be of significant practical value [1–3], as they can bring the strongly responsive behaviour of LCs into contexts where they were previously inaccessible. Offering flexibility, breathability and extreme light weight, and combining a textile form factor, high surface-to-volume ratio, and the liquid fluidity yet anisotropic functionality of the LC, these mats could be particularly suitable for clothing-integrated sensors of, e.g. temperature [4–6], strain [4], light [7,8] or volatile organic compound exposure [2,9–11], or for textiles with enhanced mechanical properties [12,13].

Two approaches have been followed for electrospinning fibres with LC cores. Single-phase spinning can be used, in which polymer and LC are co-dissolved in a common solvent and a coaxial core–sheath structure arises as a result of *in situ* phase separation as the solvent evaporates in flight [9,14–16]. Alternatively, the LC and polymer solution are separated from the start, the LC

CONTACT J.P.F. Lagerwall jan.lagerwall@lcsoftmatter.com
Supplemental data for this article can be accessed here.

being introduced as one or multiple cores within the flowing polymer solution using a spinneret with nested channels, in a coaxial geometry for the most common case that only one core is targeted [2,4,17]. Several interesting proofs of concept have been demonstrated using both methods, but the transition from experiments in the research lab to production of functional mats that can be conveniently applied in wearable technology has been slow. Two major obstacles – in many ways related – are of particular importance.

First, the range of polymers used for the sheath has been very limited, most successful experiments being performed with polyvinylpyrrolidone (PVP) [2,4,6–8,10,11]. A sheath of PVP is inappropriate for many applications due to its poor mechanical stability, lack of convenient crosslinking means, and strong sensitivity to humidity. The sensitivity to humidity is very much present also at the stage of spinning in case of the popular choice to use 4′-n-pentylbiphenyl-4-carbonitrile (5CB) as core LC and ethanol-dissolved PVP as sheath: water condensing from the air onto the Taylor cone raises the temperature range of a large miscibility gap between two different isotropic phases in the 5CB-ethanol phase diagram to ambient temperatures [18], triggering uncontrolled multi-interface phase separation that disrupts spinning [19].

The low number of polymers explored for the sheath is a direct consequence of the second obstacle, namely that many textile grade polymers are so chemically similar to the LC that the solvents needed to dissolve the polymer also dissolve the LC very well, and after the solvent evaporates, the LC mixes with the polymer as a plasticiser. Whether using single-phase or multi-channel spinnerets, this tends to lead to fibres that have a uniform cross-section rather than the desired core–sheath structure. The problem can also be the opposite, as in the case of water-soluble polymers like poly(vinyl alcohol) (PVA), yielding an excessively high interfacial tension to the LC that prevents spinning. Surfactants cannot be added to reduce the interfacial tension, because they may mix with the LC core, potentially even bringing in micellized water, either process with severe consequences for the LC behaviour [6].

In this paper, we present an exit strategy from these long-standing obstacles, replacing 5CB with LC mixtures that do not exhibit isotropic–isotropic phase separation in ethanol–water mixtures, using PVA as well as poly (acrylic acid) (PAA) as polymer (Figure 1), and dissolving them in a mixture of water and ethanol. Additionally, either ethanol or dioxane is added to the LC core, yielding a core–sheath interfacial tension sufficiently low to retain the core-sheath geometry defined by our dual-channel spinneret. As PVA and PAA can be crosslinked together after spinning [20,21], the final fibre mats have sufficient mechanical durability to allow manipulation by hand and they can even be immersed into water without dissolving or the LC leaking out.

2. Materials and methods

2.1. Polymer solutions and liquid crystals

Poly(acrylic acid) (PAA; $\bar{M}_w = 450\,\mathrm{kg \cdot mol^{-1}}$, a polymer soluble in both water and ethanol, was purchased from Sigma-Aldrich and dissolved in anhydrous ethanol (purchased from VWR). Poly (vinyl alcohol) (PVA, $\bar{M}_w = 85 - 124\,\mathrm{kg \cdot mol^{-1}}$, 85–87% hydrolysed, Sigma Aldrich), highly soluble in water but sparingly soluble (at low concentrations) in ethanol, was dissolved in ultrapure deionised water (conductivity 0.055 $\mu\mathrm{S \cdot cm^{-1}}$, Sartorius Arium). To achieve maximum crosslinking, a PVA-PAA solution containing equal number of carboxylate and hydroxyl groups was prepared from two separate stock solutions of PAA in anhydrous ethanol and PVA in water. The two stock solutions were then mixed together to form a solution with 10% w/w of polymer (PVA+PAA) (see the SI for detailed information).

For the core materials, we used the nematic liquid crystal mixture RO-TN 651 (F. Hoffman-La Roche, Basel, Switzerland), both pure and mixed with 25% w/w CB15 ((*S*)-4-cyano-4′-(2-methylbutyl)biphenyl, 98%, Synthon GmbH), a chiral dopant added to produce a red-reflecting LC mixture ($\lambda \approx 650$ nm). In order to facilitate the spinning process, we added either anhydrous ethanol or 1,4-dioxane (>99%, Sigma Aldrich) to the core. All materials were used as received without further purification.

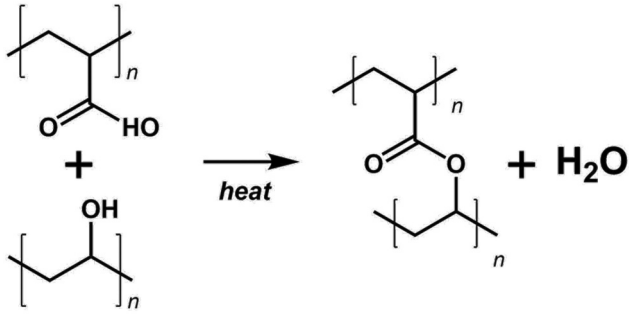

Figure 1. The chemical structures of poly(acrylic acid) (PAA), top left, and poly(vinyl alcohol) (PVA), bottom left, and the esterification reaction used to crosslink the two with each other (right).

2.2. Electrospinning parameters

The stainless steel coaxial spinneret (inner diameter: 0.9/0.6 mm; outer diameter: 1.7/1.4 mm) used for electrospinning was purchased from Y-Flow. The outer needle of the spinneret has dents to hold the inner needle in the centre. While not in use, the spinneret was stored in ethanol, and prior to each experiment, the spinneret was carefully cleaned with rinses of 96% w/w ethanol to remove any residues and then thoroughly dried using compressed air at room temperature. The electrospinning setup consisted of a mobile collector wrapped in aluminium foil, placed inside an acrylic box. The spinneret, connected to a microfluidic pressure unit (Fluigent, model MFCS-EZ, maximum pressure 1034 mbar, uncertainty $\pm$ 0.3 mbar) and a high voltage power supply (Gamma High Voltage, model ES30R-5 W/DAM/RS232), was inserted from the top of the box. The Taylor cone (the electrostatically deformed pendant drop from which the fibre-forming jet is ejected in electrospinning) was imaged using a macro lens (Tokina AT-X Pro) mounted on a camera (Pixelink D755). Figure 2 shows a schematic representation of the electrospinning setup.

The electrospinning conditions for nematic and cholesteric core are summarised in Table S2 and S3, respectively. Fibres were collected freely hanging on a copper wire frame and on hydrophobized glass microscopy slides to avoid wetting and collapse of the filled fibres [6,22]. These slides were prepared by cleaning 25 mm $\times$ 75 mm borosilicate glass microscopy slides (Carl Roth) with alternating rinses of isopropanol and deionised water before surface activation with a handheld corona generator for at least 30 s. The plasma-treated slides were then immediately immersed in an aqueous solution of 2% v/v *N,N*-dimethyl-[*N*-octadecyl-3-aminopropyl]trimethoxysilyl chloride (DMOAP, 42% in methanol, Sigma Aldrich) and allowed to stand for at least 15 min, with gentle shaking halfway through the soaking procedure to ensure that the solution adequately coated and functionalised the glass slides. The slides were then removed from the treatment solution, rinsed several times with deionised water, and dried under vacuum at 120°C for at least 30 min.

2.3. Optical characterisation

Once collected, the fibres were optically characterised using a polarising microscope (Olympus BX-51) with camera (Olympus DP73) and by scanning electron microscope (SEM). POM characterisation was carried out in transmission mode with the addition of a Linkam heating/cooling stage (T95 series LTS120E, Surrey, UK) to control the temperature of the sample during imaging. SEM imaging of the fibres was performed using a JEOL JSM-6010LA (Akishima, Japan) scanning electron microscope operated at 20 kV with working distance of 11 mm. The fibres were coated with gold ($\sim$ 5 nm thickness) using a sputter coater (Quorum Q150R ES) for 100 s prior to SEM observation.

2.4. Crosslinking of fibres

After electrospinning, the unfilled and filled fibres were thermally crosslinked through heat-induced esterification by heating under ambient pressure at 130°C for 30 min in an oven (Thermo Scientific Vacutherm).

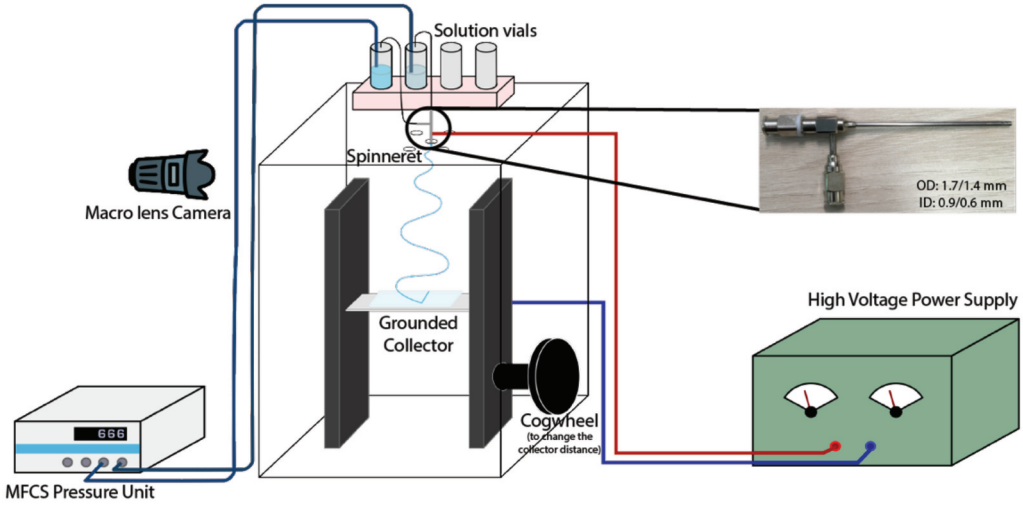

Figure 2. (Colour online) Schematic representation of the electrospinning setup. The MFCS is the pressure control unit that controls the liquid flow. Inset: The spinneret used for the experiments.

Crosslinking was verified by immersing a fibre mat sample in water; crosslinking was deemed successful when the fibres failed to dissolve after 24 hours immersion.

3. Results and discussion

3.1. Optimisation of the sheath solution

Inspired by the success of Truong et al. in electrospinning mixed PVA–PAA single-phase fibres that could be crosslinked after production [21] by means of an esterification reaction between the two polymers (Figure 1), we base our sheath solution on this mixture. In this first study, for simplicity, we add PVA and PAA at equimolar carboxyl and hydroxyl group ratio, requiring a slightly higher mole fraction of PVA since it is not fully hydrolysed (see calculation in Supplemental Online Material). An advantage of using PAA as the crosslinking partner to PVA is that PAA – in contrast to PVA – can be dissolved very well in ethanol. This allows us to use a mixture of water and ethanol as sheath solvent, of great benefit to the coaxial electrospinning experiments, as the interfacial tension to the core is lower than with a purely aqueous sheath solution. Preliminary experiments show that 7% w/w of polymer (1:1 mass ratio of PVA and PAA) can be well dissolved in a solvent consisting of 25% w/w ethanol and 75% w/w water, see Supplemental Figure S1.

Before initiating experiments with LC core we spin single-phase fibres from the ethanol–water solution of PVA and PVA and test the effect of crosslinking. We increase the overall polymer content to 10% w/w for the sheath solution to be used for the coaxial spinning. Well-formed fibre mats can easily be spun from the solution and crosslinking by thermal treatment renders them insoluble in water: as shown in Supplemental Figure S2, an uncrosslinked fibre mat dissolves completely within 24 hours when water is poured onto it, while the crosslinked fibre mat, electrospun with identical parameters, shows no sign of dissolution.

3.2. Coaxial electrospinning of composite fibres with nematic core

While the presence of ethanol in the sheath solution significantly reduces the interfacial tension γ to the LC core compared to the case when pure water is used as sheath solvent, γ still appears to be too high if a pure LC core is used, as evidenced by incomplete fibre filling or difficulties to get the LC injected into the jet leaving the Taylor cone, from which the fibres are formed. We therefore add ethanol also to the nematic LC mixture and use the resulting mixture as core. The presence of ethanol in both core and sheath fluids allows fibres that are continuously filled with nematic core to be spun, as shown in Figure 3; hence, γ has apparently been reduced to an acceptable range.

The maximum concentration of ethanol to be added to the core is empirically found to be 30% w/w: a higher ethanol content leads to dilution of the sheath fluid once the two fluids come into contact in the Taylor cone, reducing its stability and even leading to electrospraying rather than spinning. This suggests that the polymer solution becomes insufficiently entangled to prevent the Plateau–Rayleigh instability from breaking up the jet when such a core is used. We attribute this to the reduction of solvent quality for the PVA as the ethanol content in the sheath becomes too high, leading to chain collapse, as well as to the overall reduction of polymer concentration when ethanol flows from core to sheath. This may be further amplified by the ability of a Taylor cone with a high amount of ethanol to condense water from the air, due to the cooling as ethanol evaporates [19]. To avoid these problems while minimising γ, we add 30% w/w ethanol to the LC unless stated otherwise.

When electrospinning challenging fluid combinations like these, it is imperative to carefully monitor the evolution of the Taylor cone from which the fibres

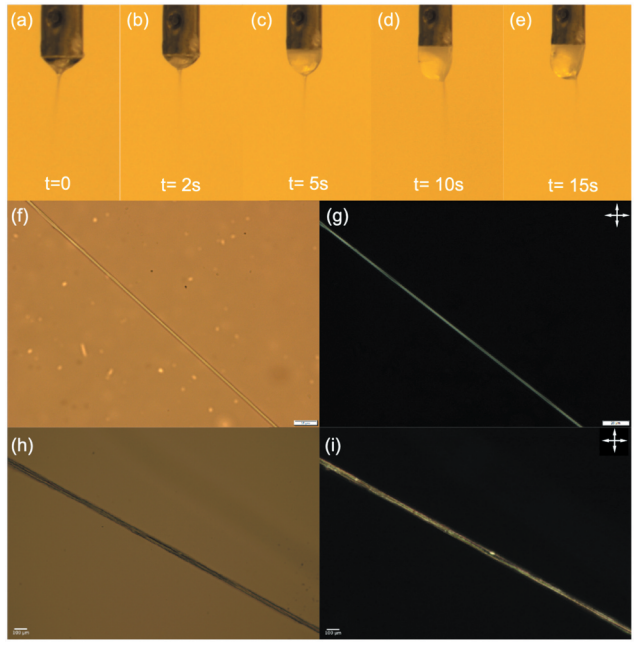

Figure 3. (Colour online) Taylor cone (a-e) and micrographs of the uncrosslinked (f & g) and crosslinked (h & i) PVA-PAA fibres filled with the nematic LC RO-TN 651, observed with transmission polarising optical microscopy between and without crossed polarisers (crossed double-headed arrows). Scale bars 20 µm. Corresponding movie of the Taylor cone attached as Supplemental Movie 1.

are ejected during spinning. We show representative photos from a successful spinning experiment in Figure 3(a–e). We start by pumping only the sheath solution and applying the voltage, until a symmetrical and stable Taylor cone has been established. As the core is introduced, we see in Figure 3(a) that the Taylor cone exhibits an overall rather turbid character, rendering the coaxial flow somewhat difficult to see. The core is naturally turbid since it is a bulk nematic phase without uniform orientation of its director field, and the reason for the sheath also becoming turbid is most likely an effect of ethanol diffusing from the core to the sheath. An increase in ethanol content significantly beyond the chosen 25% w/w makes the solvent increasingly poor for PVA, such that it approaches phase separation and becomes turbid. Nevertheless, the spinning situation is stable and the core flow extends all the way from the spinneret to the cone apex, where it injects into the jet to produce coaxial fibres well filled with LC. This is confirmed by studying the as-produced fibres in POM, see Figure 3(g/i). The fibre is uniformly birefringent (Figure 3(g)) with the LC director along the fibre axis. Supplemental Movie 2 shows that the fibre shows good extinction every time the fibre is oriented along either of the polarisers, confirming the excellent uniaxial LC alignment. If the LC flow rate is too high, the Taylor cone is overfilled with LC, growing it into a spherocylindrical shape in which the strong turbidity of the LC is clearly distinguishable from that of the sheath solution, as seen in Figure 3(d). The overfilling also affects the jet ejection, which is shifted to an off-centre location in Figure 3(d–e), most likely because of the reduction in voltage from the charged spinneret to the bottom of the pendant drop. The situation can be stabilised, however, by reducing the core flow rate until the Taylor cone regains appropriate size and the jet returns to its natural position at the cone apex.

After spinning and final solvent evaporation, the PVA and PAA in the fibre sheath are crosslinked using the protocol defined in section 2.4, and then the fibres are again investigated by POM, see Figure 3(h–i). The LC remains intact in the fibre as confirmed by the birefringence still being present, see Figure 3(i). Supplemental Movie 4 shows that the fibres are still brighter at 45° angle to the polarisers than when they are aligned with the polarisers, but clearly some loss of director alignment has resulted from the crosslinking. To confirm that the birefringence is indeed due to the LC and not due to crystallised sections of the PVA and/or PAA, we heat the fibre above the clearing temperature T_c of the RO-TN 651 LC mixture, where it transitions into an isotropic liquid phase, see Figure 4. Indeed, the fibres become almost perfectly black at temperatures greater than T_c (Figure 4(c)), demonstrating that the original birefringence is solely due to the LC core, which is isotropic and thus not birefringent at high temperature. Importantly, upon cooling back below T_c, the birefringence recovers and the texture is similar to the original one (Figure 4(d)), demonstrating that the LC order recovers as it was prior to taking the core through the phase transition. In these high-magnification images, it is clear that the local texture has changed somewhat as a result of the high-temperature treatment. It appears more compartmentalised, suggesting that the crosslinking of the sheath has partially led to interruptions in the originally continuous core channel. Since many applications of LC-functionalised fibres will use cholesteric rather than nematic liquid crystals, this loss of nematic alignment is not critical, and we will see in the following that the selective reflection of an encapsulated cholesteric core is intact also after crosslinking.

3.2.1. Coaxial electrospinning of composite fibres with cholesteric core

The addition of 25% w/w of the chiral dopant CB15 to RO-TN 651 to obtain a red-reflecting cholesteric LC mixture significantly reduces T_c, since CB15 is isotropic at room temperature. Adding ethanol to this mixture led to poor results when attempting coaxial spinning, possibly due to the similarity of CB15 to 5CB, yielding a problematic isotropic–isotropic phase separation in mixtures with ethanol and water [18,19]. For this reason, we searched for an alternative solvent to be added to the cholesteric core which fulfils the need to reduce the effective interfacial tension during spinning, but

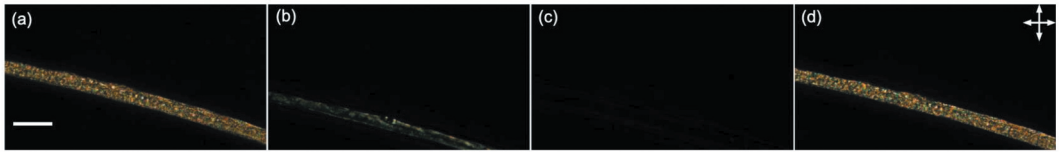

Figure 4. (Colour online) Nematic LC-filled crosslinked PVA-PAA fibres heated above the clearing point (T_c) and cooled below it. (a) Before heating; (b) LC clearing as we approach T_c; (c) the LC appearing dark upon reaching the T_c; and (d) the colours reappearing on cooling the fibres. Scale bar 20 µm. Images are extracted from Supplemental Movie 3.

without inducing phase separation between two isotropic phases. We found 1,4-dioxane to be such a solvent and thus prepared the core fluid by mixing 10% w/w of 1,4-dioxane to the cholesteric LC. When the core fluid comes into contact with the primarily water-based sheath fluid, the dioxane very rapidly mixes with the water in the sheath, while the opposite flow is negligible due to the immiscibility between the LC and water. This dynamic situation produces an extended composition gradient that results in an effective interface with low enough γ to allow stable coaxial spinning with the cholesteric LC core and the PVA–PAA solution sheath, see Figure 5.

Observation of the Taylor cone during the spinning process (Figure 5(a–e)) reveals that it changes shape over time, adopting a slightly distorted shape that indicates that some gelation is taking place at the Taylor cone surface. This may be because dioxane is a good solvent neither for PVA nor PAA; hence, the sheath solution gels as the ethanol component evaporates and dioxane takes its place, and composite fibres with continuous cholesteric LC core are obtained, as shown in Figure 5(f–g). The obtained fibres are rather thin (diameters 1–5 µm) and therefore the selective reflection of the cholesteric core is not observable by the unaided eye. However, using reflection-mode POM confirms the presence of the cholesteric LC in the fibres and the resulting red reflection. As expected for the circularly polarised selective reflection from cholesteric LCs, the colour is constantly visible as the fibre is rotated on the POM stage, irrespective of orientation with respect to the linear polarisers, see Supplemental Movie 6.

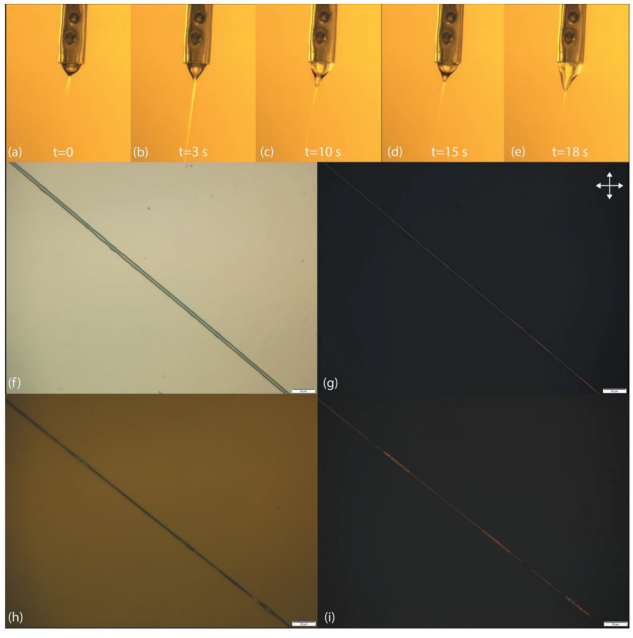

Figure 5. (Colour online) Taylor cone at (a) 0 s, (b) 3 s, (c) 10 s, (d) 15 s, and (e) 18 s and micrographs of the uncrosslinked (f & g) and crosslinked (h & i) PVA-PAA fibres filled with cholesteric LC, observed in reflection mode with polarising optical microscopy between and without crossed polarisers. Scale bars 20 µm. Corresponding Taylor cone movie attached as Supplemental Movie 5.

As for the nematic core fibres, the mats are crosslinked after all solvent has evaporated, using the same protocol as before, and the fibres are again observed with reflection-mode POM to ascertain the remaining presence of cholesteric LC, see Figure 5(h–i). There is again some loss of core continuity, but it is not very strong. Most significantly, the red reflection colour is still readily observable. To obtain fibres that do not require microscopy to detect the reflection colour, further optimisation of sheath and core fluid compositions is required in order to allow a greater core flow rate. This will allow the fibre diameter to be increased beyond ~5 µm, which is thick enough to allow the reflection colour to be seen by the naked eye, despite scattering from the sheath [4]. However, since the fibres are crosslinked and thus survive immersion in liquids that swell the sheath, we can remove the scattering from the sheath in other ways, as described below.

3.3. Confirmation of resistance to water and test of mechanical durability after crosslinking of the sheath

PAA and PVA, being water-soluble polymers, are not particularly suited on their own for making fibre mats that should be used in practical applications. With the two polymers crosslinked to each other in the sheath, however, they become very useful. In particular, crosslinking prevents dissolution, but the hygroscopic nature of both PVA and PAA still allows them to swell significantly in water. To test this, we immerse fibre mats with nematic as well as with cholesteric cores in water and study their behaviour, see Figure 6 for an example with nematic core. As for the preliminary experiments without LC core, the crosslinked samples do not dissolve in water even after immersion for 72 h. The uncrosslinked samples, in contrast, start to dissolve in water within a matter of minutes. After 24 h, the uncrosslinked sample has completely dissolved in water.

It is particularly interesting to study the cholesteric LC-filled fibres during immersion. Since the PVA-PAA sheath can become highly swollen by water, its refractive index should become much closer to that of the water surrounding the fibres, meaning that the light scattering at the interface between sheath and surrounding water should largely disappear. We confirm this by observing a fibre mat in a Petri dish using reflection-mode POM,

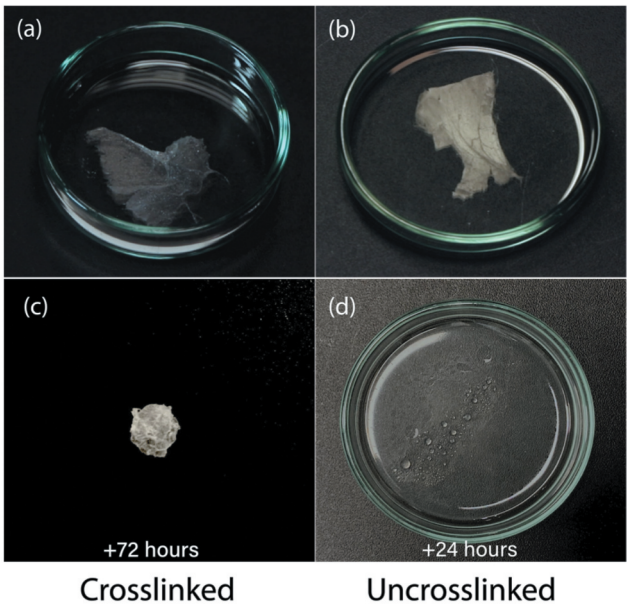

Figure 6. (Colour online) Macroscopic samples of mats spun from hybrid PVA/PAA fibres filled with RO-TN 651, both crosslinked (left: a & c) and not crosslinked (right: b & d), viewed without polarisers. While the fibre sample (c) at 72 h after immersion contracted without a supporting frame, it remained intact, especially compared to the fibres without crosslinks in (d) which simply dissolved within 24 h.

as the dish is filled with water, see Figure 7. Immediately upon immersion, the sheath indeed becomes practically invisible, and the fibres show only the strong red colour due to selective reflection from the cholesteric core (Figure 7(b)). The fibres remain fully intact upon water immersion, which further verifies the success of the crosslinking procedure.

Finally, we characterise the fibres (both uncrosslinked and crosslinked) at the nanoscopic scale using scanning electron microscopy (SEM), to assess their original surface morphology and how this may change by crosslinking, see Figure 8. Additionally, a sample of crosslinked fibres that has been immersed in water is dried, and then observed in the SEM to test for any degradation from the water immersion. These investigations show fibres that appear thicker after crosslinking than before (Figure 8(a–b)), which is surprising considering that crosslinking of polymers typically leads to shrinkage. We conjecture that this is due to a certain degree of aggregation of fibres upon crosslinking. Comparing the crosslinked fibres before and after immersion in water, we see surprisingly little change at the individual fibre level in these samples. However, the overall fibre mat was suspended on a frame during this experiment to prevent collapse upon drying due to the capillary forces acting on the fibres as the water evaporates. As shown in Figure 6(c), the capillary forces leads to crumpling together into a dense lump if the fibre mat is not suspended during drying.

We also attempted basic mechanical experiments on the crosslinked fibre mats to test for elongation at break and the maximum tensile stress. Unfortunately, the fibre mats are of a shape that is incompatible with standard mechanical testers and the results were not conclusive. Our general observations are that the fibre mats are significantly more robust than uncrosslinked fibres, such that they can easily be handled with fingers, even with moist skin, in contrast to uncrosslinked fibres of hygroscopic polymers like PAA, PVA or PVP. The degree of crosslinking is high in these fibres with

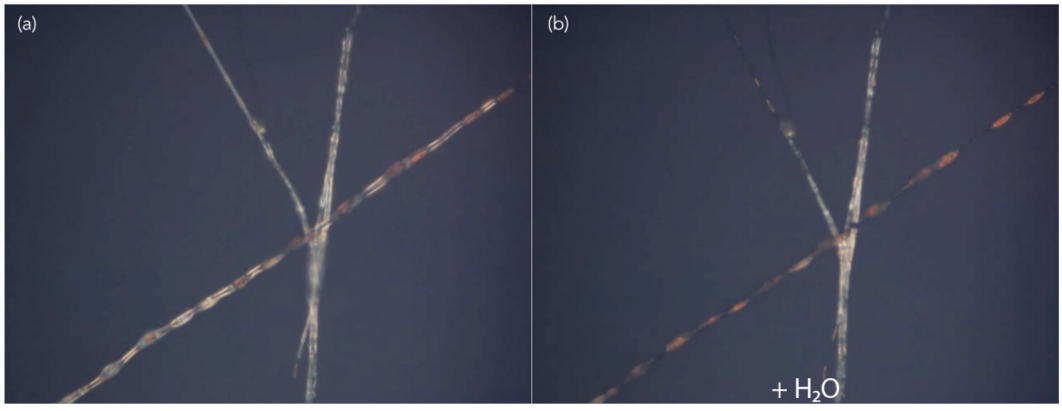

Figure 7. (Colour online) Cholesteric LC-filled fibres before (a) and during (b) water immersion, as they appear in reflection POM. The red colour of the cholesteric LC core becomes much more prominent during water immersion, as the scattering from the sheath disappears (b). The fibre running largely vertical in the photo, as well as its diagonal branch, are at slightly higher level and are thus not immersed in water, explaining their remaining scattering. Corresponding movie attached as Supplemental Movie 7.

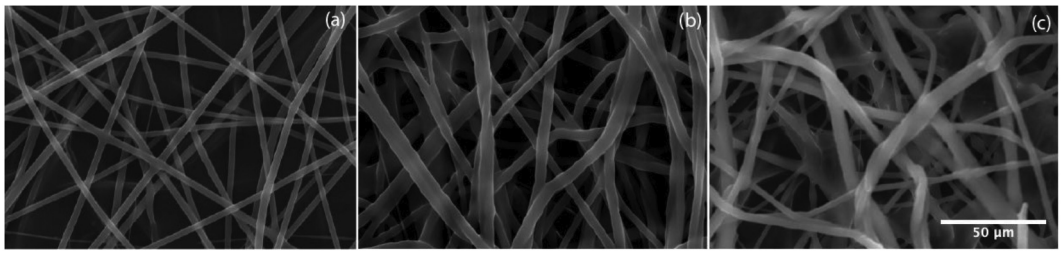

Figure 8. (Colour online) SEM micrographs of filled PVA-PAA composite fibres that were (a) uncrosslinked; (b) crosslinked; and (c) crosslinked and dried after immersion in water. Scale bar 50 µm.

equimolar carboxyl and hydroxyl group content, rendering them rather stiff and brittle. More elastic fibres should be obtainable by changing the PVA:PAA ratio, in turn changing the crosslinking density, and possibly by adding short flexible crosslinker chains, such as hydroxyl-terminated oligoethylenes.

4. Conclusions and outlook

To overcome the long-standing obstacles to making liquid crystal-functionalised electrospun fibre mats that are durable enough for use in wearable technology, we combine PAA and PVA in the sheath such that they can be crosslinked after spinning, resulting in fibres that can be easily manipulated by hand and even fully immersed in water without dissolving and without losing their functional LC core. Since the PVA requires water to be used as sheath solvent, the interfacial tension with the LC core needs to be reduced in order to avoid core break-up due to the Plateau–Rayleigh instability. We achieve this by mixing water and ethanol as sheath solvent and adding either ethanol or dioxane also to the LC core. With ethanol as co-solvent, the two fluids share a common constituent from the start, reducing the interfacial tension. When ethanol is not suitable for the core, dioxane can instead be used, its rapid diffusion into the aqueous sheath phase having a similar beneficial effect on reducing the interfacial tension. While the degree of crosslinking in the sheath of the fibres presented here is higher than optimum, leading to fibres that are rather brittle in their dry state, the same principle can be used to achieve fibres with 10–20% crosslinking in the sheath. With such a modification, we may expect LC-functionalised fibres that are insoluble and mechanically durable, while also being highly flexible and even stretchable, truly opening the path to wearable technology based on electrospun fibres with liquid crystal core.

An interesting side effect of the possibility to immerse the LC-functionalised fibres in water without dissolution, but with the sheath being swelled by the water, is that we achieve index matching between the sheath and the surrounding, removing the scattering from the sheath and thus allowing the liquid crystal optics to appear in full clarity. This opens doors to in-depth studies of the effects of the confinement within the fibre sheath on the LC behaviour, with much higher optical resolution and with less artefacts, since the undistorted LC optics can conveniently be studied. Cylindrical confinement effects can be strong and of unexpected nature, including chiral structures induced from non-chiral LCs, as recently demonstrated for lyotropic nematics in cylindrical glass capillaries [23–25]. Signs of similar effects on thermotropic LCs in the much stronger confinement of electrospun fibres have been reported [26], but were not yet elucidated in detail, in part due to the optical complications of a visible polymer sheath.

Acknowledgments

The authors thank Mr Nicolas Tournier, Dr Hakam Agha, and Dr Ulrich M. Siegel for assistance in constructing the experimental set-up; Ms Zornitza Tosheva for helping with SEM imaging; and Dr Manos Anyfantakis, Dr V.S.R. Jampani, and Ms Katrin Schelski for fruitful discussions.

Disclosure statement

No potential conflict of interest was reported by the authors.

Funding

Funding for this research was provided by a European Research Council Consolidator Grant [INTERACT, grant number 648763] and by an *Aide à la formation-recherche* grant [LIMEFLOW, grant number 9784104] from the Luxembourg National Research Fund.

References

[1] Urbanski M, Reyes CG, and Noh J, et al. Liquid crystals in micron-scale droplets, shells and fibers. J Phys Condens Matter. 2017;29(13):133003.

[2] Kim DK, Hwang M, Lagerwall JPF. Liquid crystal functionalization of electrospun polymer fibers. J Polym Sci B Polym Phys. 2013;51(11):855–867.
[3] Wang J, Jákli A, Guan Y, et al. Developing liquid-crystal functionalized fabrics for wearable sensors. J Soc Inf Disp. 2017;33(4):16–20.
[4] Enz E, Lagerwall JPF. Electrospun microfibres with temperature sensitive iridescence from encapsulated cholesteric liquid crystal. J Mater Chem. 2010;20:6866–6872.
[5] Wang J, Jákli A, West JL. Airbrush formation of liquid crystal/polymer fibers. ChemPhysChem. 2015;16 (9):1839–1841.
[6] Kye Y, Kim C, Lagerwall JPF. Multifunctional responsive fibers produced by dual liquid crystal core electrospinning. J Mater Chem C. 2015;3 (34):8979–8985.
[7] Thum MD, Ratchford DC, Casalini R, et al. Photochemical phase and alignment control of a nematic liquid crystal in core-sheath nanofibers. J Mater Chem C. 2021;9:12859.
[8] Thum MD, Ratchford DC, and Casalini R, et al. Azobenzene-doped liquid crystals in electrospun nanofibrous mats for photochemical phase control. ACS Appl Nano Mater. 2021;4(1):297–304.
[9] Agra-Kooijman DM, Robb C, Guan Y, et al. Liquid crystal core polymer fiber mat electronic gas sensors. Liq Cryst. 2021 Apr;48:1–8.
[10] Pschyklenk L, Wagner T, and Lorenz A, et al. Optical gas sensing with encapsulated chiral-nematic liquid crystals. ACS Appl Polymer Mater. 2020;2 (5):1925–1932. DOI: 10.1021/acsapm.0c00142.
[11] Reyes CG, Sharma A, Lagerwall JPF. Non-electronic gas sensors from electrospun mats of liquid crystal core fibres for detecting volatile organic compounds at room temperature. Liq Cryst. 2016;43(13–15):1986–2001.
[12] Sharma A, Lagerwall JPF. Electrospun composite liquid crystal elastomer fibers. MDPI Mater. 2018;11(3):393.
[13] Bertocchi MJ, Simbana RA, Wynne JH, et al. Electrospinning of tough and elastic liquid crystalline polymer–polyurethane composite fibers: mechanical properties and fiber alignment. Macromol Mater Eng. 2019;304(8):1900186.
[14] Ebru BA, Margaret FW, John WL. Self-assembled, optically responsive nematic liquid crystal/polymer core-shell fibers: formation and characterization. Polymer. 2010;51(21):4823–4830.
[15] Wang J, Jákli A, West J. Morphology tuning of electrospun liquid crystal/polymer fibers. ChemPhysChem. 2016;17(19):3080–3085.
[16] Jasiurkowska-Delaporte M, Juszyńska-Galazka E, and Sas W, et al. Soft versus hard confinement effects on the phase transitions, and intra- and intermolecular dynamics of 6bt liquid crystal constrained in electrospun polymer fibers and in nanopores. J Mol Liq. 2021;331:115817.
[17] Lagerwall JPF, McCann JT, Formo E, et al. Coaxial electrospinning of microfibres with liquid crystal in the core. Chem Commun. 2008;42:5420–5422.
[18] Reyes CG, Baller J, Araki T, et al. Isotropic–isotropic phase separation and spinodal decomposition in liquid crystal–solvent mixtures. Soft Matter. 2019;15:1–11.
[19] Reyes CG, Lagerwall JPF. Disruption of electrospinning due to water condensation into the Taylor cone. ACS Appl Mater Interfaces. 2020;12(23):26566–26576. PMID: 32420728.
[20] Kumeta K, Nagashima I, and Matsui S, et al. Crosslinking reaction of poly (vinyl alcohol) with poly (acrylic acid)(PAA) by heat treatment: effect of neutralization of PAA. J Appl polymersci. 2003;90 (9):2420–2427.
[21] Truong YB, Choi J, Mardel J, et al. Functional crosslinked electrospun polyvinyl alcohol membranes and their potential applications. Macromol Mater Eng. 2017;302(8):1700024.
[22] Kim DK, Lagerwall JPF. Influence of wetting on morphology and core content in electrospun core-sheath fibers. ACS Appl Mater Interf. 2014;6 (18):16441–16447.
[23] Dietrich CF, Rudquist P, Lorenz K, et al. Chiral structures from achiral micellar lyotropic liquid crystals under capillary confinement. Langmuir. 2017;33 (23):5852–5862.
[24] Nayani K, Chang R, Fu J, et al. Spontaneous emergence of chirality in achiral lyotropic chromonic liquid crystals confined to cylinders. Nat Commun. 2015;6:8067.
[25] Jeong J, Kang L, Davidson Z, et al. Chiral structures from achiral liquid crystals in cylindrical capillaries. Proc Natl Acad Sci U S A. 2015;112(15):E1837–44.
[26] Reyes CG. Confined in a fiber: realizing flexible gas sensors by electrospinning liquid crystals [dissertation]. Luxembourg: University of Luxembourg; 2019.

Supplemental Online Material for "Combining responsiveness and durability in liquid crystal-functionalized electrospun fibers with crosslinked sheath"

Shameek Vats, Lawrence W. Honaker, Francesco Basoli, and Jan P.F. Lagerwall

A. Supplementary Figures

Figure S1. Test of how high ethanol fraction can be used in the solvent to dissolve an equimolar ratio of PVA and PAA at 7% by mass. A clear solution is obtained with 25% by mass ethanol, while some phase separation is seen at 50% by mass. At higher ethanol fractions, the samples appear a turbid white due to the strong phase separation.

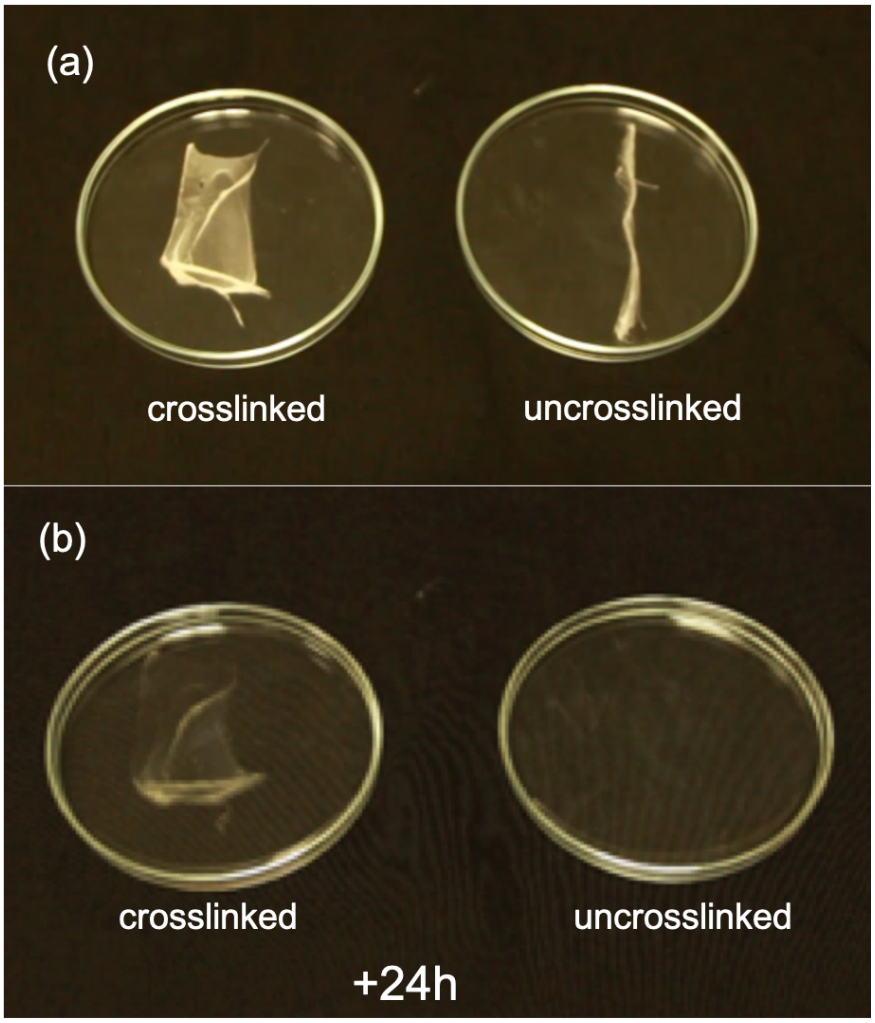

Figure S2. Macroscopic images of pure PVA-PAA fiber mats (no LC core) both crosslinked and uncrosslinked before (a) immersion in water and (b) 24 hours after immersion. Upon water immersion of both mats, the uncrosslinked mat dissolves immediately while the crosslinked mat remained intact; panel (c) shows it after 12 hours of water immersion.

B. Calculation of polymer mixture ratios

We consider masses of PVA, PAA, ethanol and water are m_{PVA}, m_{PAA}, m_E and m_W, respectively. The corresponding molar masses are $M_{PVA} = 44.05$ g/mol, $M_{PAA} = 72.06$ g/mol, $M_E = 46.07$ g/mol and $M_W = 18.02$ g/mol. PVA stock solutions in water with x mass-percent and PAA stock solutions in ethanol with y mass-percent, were prepared by i.e.:

$$x = \frac{100 m_{PVA}}{m_{PVA} + m_W} \tag{1}$$

and

$$y = \frac{100 m_{PAA}}{m_{PAA} + m_E}. \tag{2}$$

To have three different *molar* ratios R of ethanol to water, specifically, 25:75, 50:50 and 75:25. Since $n_E = m_E/M_E$ and $n_W = m_W/M_W$, we can write:

$$R = \frac{m_E/M_E}{m_W/M_W} = \frac{m_E M_W}{m_W M_E}, \tag{3}$$

which means that:

$$\Rightarrow m_W = \frac{m_E M_W}{R M_E}. \tag{4}$$

Inserting (4) into (1):

$$x = \frac{100 m_{PVA}}{m_{PVA} + \frac{m_E M_W}{R M_E}} \Leftrightarrow x(m_{PVA} + \frac{m_E M_W}{R M_E}) = 100 m_{PVA} \tag{5}$$

$$\Rightarrow m_{PVA}(100 - x) = \frac{x m_E M_W}{R M_E} \Rightarrow m_{PVA} = \frac{x m_E M_W}{(100 - x) R M_E}$$

In order to optimize the crosslinking of the fibers, equal fraction PVA monomers and PAA monomers needs to be considered. Since PVA is only 85% hydrolyzed, and the remaining 15% polyvinylacetate is not crosslinkable with PAA. This means that only $0.85 m_{PVA}$ is considered when we calculate the number of moles of each polymer. We thus get:

$$n_{PVA} = \frac{0.85 m_{PVA}}{M_{PVA}} = \frac{0.85}{44.05} m_{PVA} \text{ moles} \tag{6}$$

and

$$n_{PAA} = \frac{m_{PAA}}{M_{PAA}} = \frac{1}{72.06} m_{PAA} \text{ moles}, \tag{7}$$

provided that all masses are given in grams. to have an equimolar ratio, these must

be set equal, thus:

$$\frac{0.85}{44.05}m_{PVA} = \frac{1}{72.06}m_{PAA} \Rightarrow m_{PVA} = \frac{44.05}{0.85 \cdot 72.06}m_{PAA} \tag{8}$$

There are now two different expressions for the mass of PVA, (5) and (8), are set equal:

$$m_{PVA} = \frac{xm_E M_W}{(100-x)RM_E} = \frac{44.05}{0.85 \cdot 72.06}m_{PAA} \Rightarrow m_{PAA} = \frac{0.85 \cdot 72.06xm_E M_W}{44.05(100-x)RM_E} \tag{9}$$

The concentration of PVA solution can be written as:

$$y = \frac{100m_{PAA}}{m_{PAA}+m_E} = 100\frac{\frac{0.85\cdot 72.06xm_E M_W}{44.05(100-x)RM_E}}{\frac{0.85\cdot 72.06xm_E M_W}{44.05(100-x)RM_E}+m_E} = 100\frac{\frac{0.85\cdot 72.06xM_W}{44.05(100-x)RM_E}}{\frac{0.85\cdot 72.06xM_W}{44.05(100-x)RM_E}+1} = \tag{10}$$

$$= \frac{85 \cdot 72.06xM_W}{44.05(100-x)RM_E} \cdot \frac{44.05(100-x)RM_E}{0.85 \cdot 72.06xM_W + 44.05(100-x)RM_E} =$$

$$= \frac{85 \cdot 72.06xM_W}{0.85 \cdot 72.06xM_W + 44.05(100-x)RM_E} = \frac{6125xM_W}{61.25xM_W + 44.05(100-x)RM_E}$$

The overall polymer mass fraction P could be selected to a certain value, say 7%, by the following calculations:

$$P = \frac{100(m_{PVA}+m_{PAA})}{m_{PVA}+m_{PAA}+m_E+m_W} = \frac{100(\frac{xm_E M_W}{(100-x)RM_E}+\frac{0.85\cdot 72.06xm_E M_W}{44.05(100-x)RM_E})}{\frac{xm_E M_W}{(100-x)RM_E}+\frac{0.85\cdot 72.06xm_E M_W}{44.05(100-x)RM_E}+m_E+\frac{m_E M_W}{RM_E}} = \tag{11}$$

$$= \frac{100x(\frac{1}{(100-x)RM_E}+\frac{0.85\cdot 72.06}{44.05(100-x)RM_E})}{\frac{x}{(100-x)RM_E}+\frac{0.85\cdot 72.06x}{44.05(100-x)RM_E}+\frac{1}{M_W}+\frac{1}{RM_E}} = \frac{100x(\frac{1}{(100-x)RM_E}+\frac{1.39}{(100-x)RM_E})}{\frac{x}{(100-x)RM_E}+\frac{1.39x}{(100-x)RM_E}+\frac{1}{M_W}+\frac{1}{RM_E}} =$$

$$= \frac{100x(\frac{2.39}{(100-x)RM_E}}{\frac{2.39x}{(100-x)RM_E}+\frac{1}{M_W}+\frac{1}{RM_E}}$$

To keep P and R freely choosable, keeping them independent variables, (11) can be rewritten in order to get x as a function of P and R:

$$\frac{239x}{(100-x)RM_E} = P\left(\frac{2.39x}{(100-x)RM_E}+\frac{1}{M_W}+\frac{1}{RM_E}\right) \tag{12}$$

$$\Leftrightarrow \frac{x(239-2.39P)}{(100-x)RM_E} = P\left(\frac{1}{M_W}+\frac{1}{RM_E}\right) \Leftrightarrow \frac{x(239-2.39P)}{RM_E} = P\left(\frac{1}{M_W}+\frac{1}{RM_E}\right)(100-x)$$

$$\Leftrightarrow x\left[\frac{(239-2.39P)}{RM_E}+P\left(\frac{1}{M_W}+\frac{1}{RM_E}\right)\right]=100P\left(\frac{1}{M_W}+\frac{1}{RM_E}\right)$$

$$\Rightarrow x=\frac{100P\left(\frac{1}{M_W}+\frac{1}{RM_E}\right)}{\left[\frac{(239-2.39P)}{RM_E}+P\left(\frac{1}{M_W}+\frac{1}{RM_E}\right)\right]}=\frac{100}{\frac{239-2.39P}{RM_E}\cdot\frac{1}{P\left(\frac{1}{M_W}+\frac{1}{RM_E}\right)}+1}=$$

$$=\frac{100}{1+\frac{239-2.39P}{PRM_E\left(\frac{1}{M_W}+\frac{1}{RM_E}\right)}}=\frac{100}{1+\frac{239-2.39P}{P\left(\frac{RM_E}{M_W}+1\right)}}$$

We now have all we need, because we have chosen R and we have an equation for x, so we can get y from equation (10).

As for the volumes/masses of each solution, we can freely choose m_E and then equation (4) gives us m_W. Note that we do not yet have the masses of the *solutions*, only of each respective pure solvent. To get the solution mass, we need to add the polymer mass, but these are given in equations (5) and (8):

$$m_1=m_{PVA}+m_W=\frac{xm_EM_W}{(100-x)RM_E}+\frac{m_EM_W}{RM_E}=\frac{m_EM_W}{RM_E}\left(\frac{x}{100-x}+1\right)=\frac{m_EM_W}{RM_E}\left(\frac{100}{100-x}\right) \tag{13}$$

and

$$m_2=m_{PAA}+m_E=\frac{0.85\cdot 72.06m_{PVA}}{44.05}+m_E=\frac{0.85\cdot 72.06\frac{xm_EM_W}{(100-x)RM_E}}{44.05}+m_E= \tag{14}$$

$$=m_E\left[1.39\frac{xM_W}{(100-x)RM_E}+1\right]$$

Table S1. Calculated mass percentages of sheath and core used for electrospinning.

	Sheath		Core	
	Polymer	Solvent	LC	Solvent
Nematic	10% PVA-PAA	90% 1:3 EtOH:water	70% RO-TN 651	30% EtOH
Cholesteric	10% PVA-PAA	90% 1:3 EtOH:water	90% 1:3 CB15:RO-TN 651	10% 1,4-dioxane

Table S2. Parameters and conditions for electrospinning with nematic LC core

Relative Humidity(%)	Temperature (°C)	Distance (cm)	Voltage (kV)	Flow rate (ml/h)	
				Sheath	Core
30	22.5	9	12.5	0.0021	0.029

Table S3. Parameters and conditions for electrospinning with cholesteric LC mixture as the core

Relative Humidity(%)	Temperature (°C)	Distance (cm)	Voltage (kV)	Flow rate (ml/h)	
				Sheath	Core
31	23.6	9	7.5	0.002	0.021

C. Description of ESI movies

(1) Movie of Taylor cone while spinning with RO-TN-651 nematic LC as core. The continuous spinning cycle with core injection is about 15 s, after which the spinneret must be wiped clean (end of the movie) to avoid dripping of liquid onto the fiber mat.

(2) Movie of uncrosslinked fiber with nematic LC core as it is rotated on the transmission POM between crossed polarizers. The good extinction when the fiber is along the polarizer (vertical in the movie) and the nearly uniform brightness for orientation about 45° to the polarizer confirm the good alignment of the LC director along the fiber axis.

(3) Movie of crosslinked fiber with nematic LC core, seen in transmission POM between crossed polarizers, heated above the LC clearing point and cooled back into nematic.

(4) Movie of crosslinked fiber with nematic LC core as it is rotated on the transmission POM between crossed polarizers. The fiber brightness is maximum for orientation 45° to either polarizer while it is minimum when it is along a polarizer (vertical or horizontal in the movie), confirming that LC director is aligned primarily along the fiber axis, although the lack of complete extinction when the fiber is along either polarizer shows that the alignment quality is reduced by crosslinking.

(5) Movie of Taylor cone while spinning with cholesteric LC mixture as core. Distortion of Taylor cone shape towards the end of the movie clearly shows that polymer gelation is taking place near the Taylor cone surface after about 15 s of spinning.

(6) Movie of uncrosslinked fiber with cholesteric LC core as it is rotated on the reflection POM between crossed polarizers. The red reflection color is visible independent of orientation with respect to the polarizers, as expected since the reflected light is circularly polarized.

(7) Movie of crosslinked fibers with cholesteric LC mixture as core, observed in reflection POM between crossed polarizers, while the inclined fiber is being immersed in water. Its sheath is imbibed with water, reducing the refractive index contrast with the surrounding to near zero, thus eliminating the scattering. The near vertical fiber and its branch are above the water surface and thus retain their scattering.

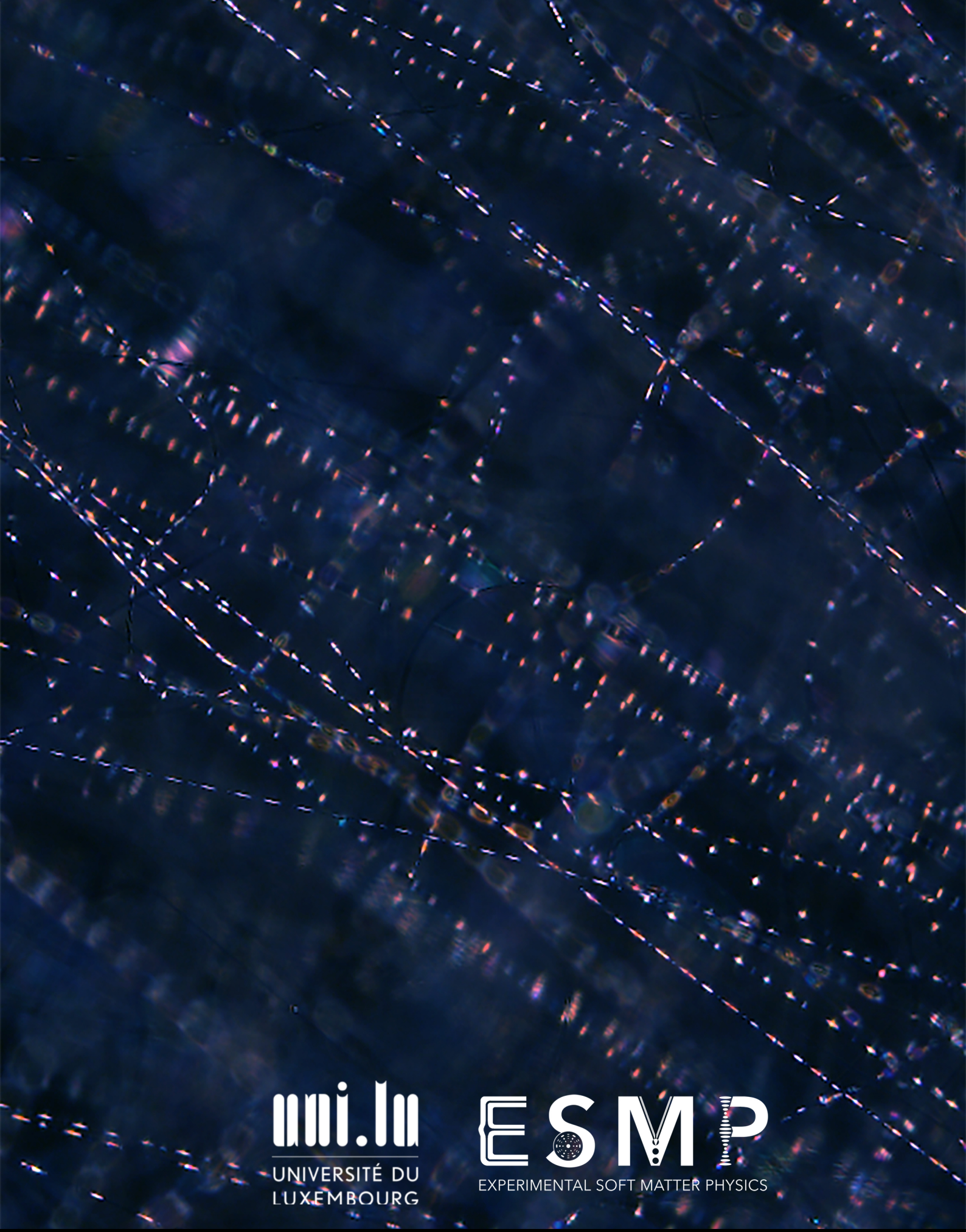

UNIVERSITÉ DU LUXEMBOURG

ESMP

EXPERIMENTAL SOFT MATTER PHYSICS